UNIVERSITE DE NEUCHATEL FACULTE DES SCIENCES

MAGNETOTELLURIC AND SEISMICITY STUDIES ALONG ACTIVE FAULT ZONES

THESE

Présentée à la Faculté des Sciences de l'Université

pour l'obtention du grade de docteur ès sciences

par

MAHMOUD MEKKAWI

Geophys. M. Sc.

COMMISSION D'EXAMEN:

M.	Prof. M. Burkhard	Directeur de thèse (Neuchâtel)
Mme	Prof. A. Kalt	(Neuchâtel)
M.	Prof. Guy Marquis	(Strasbourg - F)
M.	Dr. P.-A. Schnegg	Co-directeur de thèse (Neuchâtel)

2003

IMPRIMATUR POUR LA THESE

Magnetotelluric and seismicity studies

along active fault zones

de M. Mahmoud MEKKAWI

UNIVERSITE DE NEUCHATEL

FACULTE DES SCIENCES

La Faculté des sciences de l'Université de
Neuchâtel, sur le rapport des membres du jury

Mme A. Kalt, MM. M. Burkhard (directeur de thèse) ,
P.-A. Schnegg (co-directeur de thèse) et
G. Marquis (Strasbourg F)

autorise l'impression de la présente thèse.

Neuchâtel, le 26 septembre 2003

Le doyen:

François Zwahlen

DECLARATION

This thesis has been composed by me and has not been submitted for any other degree. Except where acknowledgement is made, the work is original.

Mahmoud Mekkawi

Abstract

Crustal water is an ideal target for magnetotelluric studies (MT), due to its decreased electrical resistivity contrasting with the high resistive rock matrix of the sediments and basements rocks. The electrical resistivity in the earth is very sensitive to the presence of interconnected fluids. This parameter helps mapping the distribution of fluids within the fault zone. The aims in our research are:

- To check that the crustal fluids play a role in triggering earthquakes in two moderately seismic areas, Aswan (Egypt) and the southern Vosges (France).
- To detect electrical resistivity anomalies which can be linked directly with earthquake activity (i.e. fluids along fault planes).
- To understand the connection between electrical resistivity anomalies and earthquake occurrences.

We applied the MT method to active faults in Aswan (Kalabsha fault) and Remiremont faults in an attempt to reveal the stress field and geological structures covered by Quaternary formations.

Seismicity in the Aswan reservoir and in southern Vosges to a certain extent, present the unique opportunity to test processes that are thought to drive the earthquake mechanisms. The Aswan seismicity is accepted as an example of reservoir-induced earthquakes since the occurrence of the M = 5.4 event in 1981. We apply statistical techniques on the Aswan earthquake catalogue to understand the seismic energy distribution in space and time domains. The spatial clustering and the magnitude distribution of earthquakes are studied to understand how the water level loading drives the moderate seismicity (M < 5.0) from 1982 to 2001. The relation between water level change and reservoir-induced seismicity shows some interesting correlation. Additionally, we observe a phase shift between water level and earthquake activity.

MT measurements are widely used to explore the electrical conductivity structure of the earth's crust from depths of a few meters down to the upper mantle. The electrical conductivity of crustal rocks depends on saline fluids, ore mineral and on the interconnectivity between these materials. The method is applied to delineate the horizontal and vertical extension of the fault system, using the fact that crustal fluids find an easy circulation path in the system and display high conductivity contrast with the rock matrix. MT data of both areas are analyzed by using the 2D simultaneous inversions (REBOCC) of TE and TM modes. The resulting models are compared with the local seismicity maps. They clearly reflect the geological tectonic stresses prevailing in the Aswan and southern Vosges areas.

Résumé

Les fluides crustaux constituent une cible idéale pour les sondages magnétotelluriques (MT), à cause de leur grande conductivité électrique qui contraste avec la grande résistivité des roches encaissantes formées de sédiments ou du socle. Dans le sous-sol, la résistivité électrique est un paramètre sensible à la présence de fluides interconnectés. Cette propriété permet d'établir la distribution des fluides dans une zone de failles, par exemple. Les buts de notre recherche sont:

- Vérifier que les fluides crustaux jouent bien un rôle dans le déclanchement des tremblements de terre de deux régions particulières : Assouan (Egypte) et Vosges (France).
- Détecter les anomalies de résistivité électrique directement liées à l'activité sismique (fluides le long des plans de failles).
- Comprendre la connexion entre les anomalies de résistivité électrique et la sismicité.

Nous avons appliqué la méthode MT à des failles actives à Assouan (faille de Kalabsha) et Remiremont (Vosges) dans le but de détecter le champ de contraintes et les structures géologiques cachées sous le Quaternaire.

La sismicité des régions d'Assouan et des Vosges méridionales offre une opportunité unique de tester des processus susceptibles d'induire des séismes. La sismicité d'Assouan est considérée comme représentative d'une sismicité induite par une charge d'eau (lac Nasser) depuis le séisme survenu en 1981 (M=5.4). Nous appliquons des tests statistiques au catalogue sismique d'Assouan pour comprendre la distribution temporelle et spatiale de l'énergie sismique. L'amas spatial et la distribution en magnitude des tremblements de terre sont étudiés dans le but de comprendre pourquoi et comment le niveau de l'eau a déclanché une sismicité modérée (M<5.0) entre 1982 et 2001. La relation entre le changement du niveau d'eau et la sismicité induite montre quelque relation intéressante. En outre, on observe un déphasage entre les variations de niveau et l'activité sismique.

Les sondages MT sont largement exploités pour étudier la structure électrique de la croûte à des profondeurs qui peuvent s'étendre entre quelques mètres et quelques dizaines de kilomètres. La conductivité électrique des roches dépend de leur porosité, de la présence de saumures, de minerais, et de la manière dont ces divers éléments sont interconnectés. La méthode est utilisée pour délimiter l'extension du système de failles, en mettant à profit le fait que les fluides crustaux trouvent un cheminement facile dans ce système, et produisent un excellent contraste sur la roche mère. Les données MT des deux régions sont analysées au moyen de l'inversion simultanée des modes TE et TM par la méthode REBOCC. Les modèles qui en résultent sont comparés aux cartes de sismicité. Ils reflètent clairement les contraintes existantes dans ces deux régions d'Assouan et des Vosges méridionales.

Acknowledgements

I would like to express my great indebtedness and deep gratefulness to my supervisor Dr. Pierre-André Schnegg for his kind supervision and useful guidance and comments during this study. His guidance support and patience are greatly appreciated. Without his help and assistance this study could not have been carried out.

I would like to extend my thank to my colleagues of National Research Institute of Astronomy and Geophysics (NRIAG), Cairo, Egypt, for providing support during the field work (Dr. T. A. Hamed and E. A. Elathy). I also thank Prof. Dr. Yehia AbdelHady, director of the Center for Environmental Hazards Mitigation, Giza, Egypt, for his support during field work.. Also thanks to Mr. Mark Sargent (ETH, Zurich).

The author is grateful to the University Louis Pasteur, Réseau National de Surveillance Sismique, Ecole et Observatoire des Sciences de la Terre de Strasbourg, for providing the earthquake catalogue of the southern Vosges area. A special thank to Dr. Jean-Robert Grasso of Grenoble Observatory, France, for his kind help in the seismicity analysis and for his useful comments.

I also thank the group of structural geology, University of Neuchâtel (Prof. M. Burkhard, A. Hubert-Ferrari and C. Sue); A. Husker, A. Helmstetter and N. Deichmann for fruitful discussions and comments. The author is grateful to Dr. H. Awad (NRIAG) for providing the earthquake catalogue of the Lake Aswan area and for providing water level data. Furthermore, thank to Dr. S. Wiemer (ETH-Zurich) for allowing me to use the ZMAP software to analyse the earthquake catalogue.

This research project received financial support from the Swiss National Science Foundation (2100-65188).

Contents

List of Figures

List of Tables

1. Introduction

1.1 The problem

Active faults such as the San Andreas Fault (SAF) or the Anatolian fault display high distribution of earthquakes in the upper crust. Recent MT studies of SAF (Mackie et al. 1997; Unsworth et al. 1999, 2000 and Bedrosian et al. 2002) **showed that the MT method could be used to map the fluid distribution within the fault zones. The low electrical resistivity is attributed to high porosity and saline fluids present in the highly fractured zone.** The results have shown that the upper 4 kilometres of the SAF at Parkfield had a lower resistivity than segments at Cholame and Carrizo. This was interpreted as implying a higher fluid content in the seismically active Parkfield segment. The occurrence of microearthquakes and creep in the lower resistivity zone is consistent with suggestion that seismicity of SAF (Parkfield) is fluid driven.

There are also earthquakes caused by perturbations in the upper crust of the earth, due to human activities. Reservoir impoundment, fluid injection and extraction and underground mining are known to cause perturbations in the stress field, leading to earthquake rapture. Disturbance in the state of stress and hydro-mechanical environment due to application or removal of load and change in pore pressure are important factors leading to triggering of earthquakes. Additional studies of velocity structure, pore pressure measurements in deep boreholes, physical properties of rocks, spatial and temporal association with the source and cause of disturbance have contributed to the understanding of their mechanism. This research activity has important implications for the study of the mechanism of the earthquake faulting in natural tectonic settings.

The earthquakes are triggered by increased pore pressure due to natural processes and/or by a reservoir loading. The increase in pore pressure can drive fault system to failure. It is difficult to measure the actual changes in pore pressure, yet possible to compute changes in effective stress under certain assumptions. Grasso et al. (1992) applied this idea to the Monteyard reservoir area (France) to demonstrate that small changes in effective stress could trigger an earthquake. Studies on some earthquakes in the SAF area suggested that stress variations as low as 0.1 bar are sufficient to induce failure in critically stress areas (Stein 1999).

According to Chen et al. (2002) two sources of aqueous electrolytic conduction in the earth crust are magma reservoirs and crustal fluids. There is little information about the volume and rates of magma produced anywhere except in the mid oceanic ridges. Magma moves via diapirism, porous flow or fractures, creating a plumbing structure on its way toward surface.

The presence of an electrically conducting fluid such as saline pore water strongly influences the overall electrical conductivity of crustal rocks. Fracturing and fluid saturation combine to produce low

resistivity. The correlation of these two parameters strengthens the hypothesis according to which the low resistive is due to fluids rather than serpentinite or clay alone (Unsworth, 1997).

Aqueous electrolytic conducting pathway such as pores, fractures, faults and shear zones control the bulk resistivity of normal crust from the surface to more than 15 km depth (Ward, 1990). According to Vogel (1995), fluids have been sampled directly by the Soviets at a depth of about 11 km in the Kola Peninsula drill hole.

Crampin et al. (2002) stated that high pore-fluid pressures are necessary in seismically active fault planes to relieve frictional stress, allowing fracturing and earthquakes to occur on the lithostatically-clamped faults. High pore-fluid pressures are needed to open cracks (by hydraulic fracturing). Necessary driving pressures have been estimated from the thickness of mineral veins in outcrops in tectonic areas (Gudmudsson et al. 2001). Nur and Walder (1990) proposed a feedback process leading to the cycle of hydrofracture and water release.

There are many theoretical models accounting for the behaviour of saturated fluids in fractures. Active fault zones have been proposed by Noir et al. (1977); Byerlee (1990); Rice (1992); Gavrilenko et al. (2000); Gavrilenko and Gueguen, (1993, 1998); Berdichevsky and Kulikov (1995); Hickmann et al. (1995) ; Sausse et al. (2001); Karnel and Marone (2001).

1.2 The tool

The magnetotelluric (MT) method is an electromagnetic method that uses measurements of the naturally-occurring electric **E** and magnetic **H** fields at the surface of the earth to determine the distribution of the electrical resistivity in depth. This parameter is important in solid earth geophysics, mineral, and geothermal exploration because electrical resistivity depends on porosity and permeability, pore fluid saturation, temperature and the presence of conductive ore materials such as graphite and sulphides. MT is used to explore the earth's crust and the upper mantle especially in tectonically active regions (volcanic and earthquake seismology). Geothermal anomalies in the upper mantle are associated with resistivity anomalies, which show up in MT measurements (Yungul 1996).

The MT measurements made at each site yield resistivity information within depth at that location, by assuming that the subsurface structure is locally horizontal (1D). In other cases, the subsurface may be assumed 2D. Then, MT measurements are carried out along profiles perpendicular to the geological strike. The MT method as application to the exploration of sedimentary basin, is used to obtain resistivity logs without drilling (Vozoff 1972). Sometimes, the natural electric field is measured simultaneously at two or more stations without measuring the magnetic field. This is the so-called telluric method.
MT measurements are widely used to explore the electrical resistivity structure of the Earth's crust (Vozoff 1986 and 1991). It is of considerable importance to investigate the geological structure around

active faults, especially for estimating the fault activity. The principle of MT sounding is the following: Naturally occurring variations of the earth's magnetic field induce electrical currents in the conducting earth. The vertical wave attenuation is characterised by a skin-depth. To explore deep structures requires large skin depths and usually long-period signals. Very long periods (T=10,000 seconds) induce currents down to the upper mantle. These currents can be recorded at the surface along with the inducing magnetic field. Apparent resistivities of the subsurface can be computed from these fields for the two geographic axes. Then, 2D modelling is carried out to look for the best geological model able to explain the measured data.

Many areas in tectonically active regions have been investigated with MT (Bailey et al. 1974; Rooney and Hutton 1977; Camfield 1981; Schnegg et al. 1987 and 1998; Park 1991; Park et al. 1993; Madden and Mackie 1996; Mackie et al. 1997; Echternacht et al. 1997; Unsworth et al. 1997 1999 and 2000; Volti 1999; Lemonnier et al. 1999; Pous et al. 1999; Suzuki et al. 2000 and Bedrosian et al. 2002). The goal of this research is studying by MT method the role of crustal fluids in the triggering of earthquakes occurring in the seismically well-documented areas of the Aswan region (Egypt) and Remiremont area, southern Vosges (France).

1.3 Origin and spectrum of EM fields

Below about 1 Hz the sources of the field are equivalent current systems in the magnetosphere; above 1 Hz the sources are lightening discharge in the earth-ionosphere cavity. These sources provide a rich spectrum of EM fields in band between 10^3 and 10^{-4} Hz, which are ideally suited for crustal resistivity mapping. There are various sources and frequencies of variations (Yungul 1996): secular and diurnal variations, variation of exospheric origin and vibrations (Fig. 1.1).

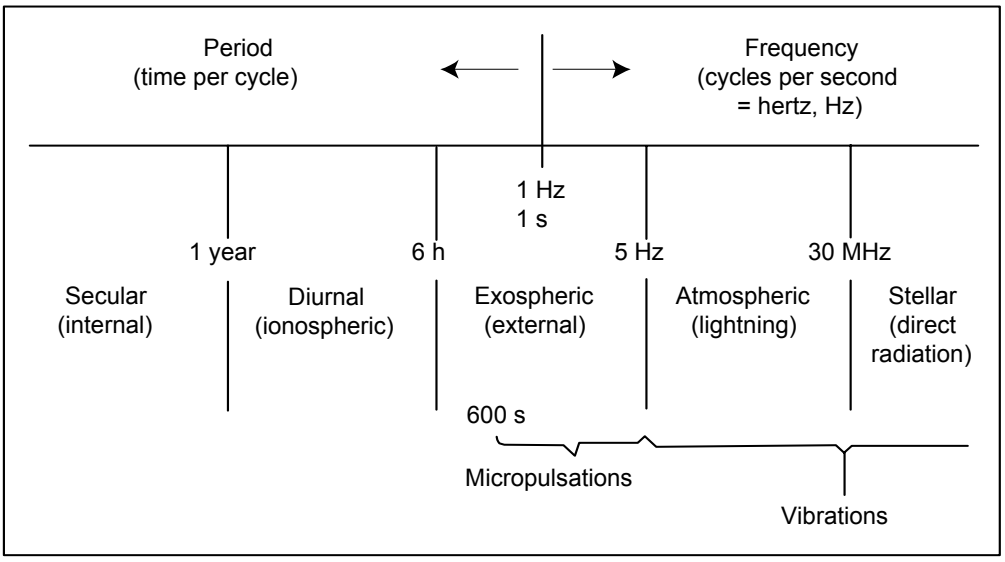

Figure 1.1. Approximate and schematic frequencies and origin of the natural electromagnetic fields (Yungul 1982).

- Secular variations: they are entirely of internal origin though to be caused by motion in the electrically conducting fluid core of the earth. The periods are measured in tens of years.

- Diurnal (daily variations): thermal effect of the sun and attraction effects of the moon, which causes the ionosphere (high electrical conductivity) to oscillate. This conductor moves in the earth's main magnetic field and forms an atmosphere dynamo. The measured periods are from 6 to 24 hours. These events have application in the exploration of the lower crust and upper mantle.

- Variation of exospheric origin: they are generated through interaction of ionised gas clouds coming from the sun, called the solar wind, with the main magnetic field of the earth. These interaction set up large sheets (loops) of electrical current in the ionosphere.

- Micropulsations are classified into two groups: continuous pulsations (Pc) and irregular pulsations (Pi). Continuous pulsations occur mostly during daytime. Pcs are subdivided into several kinds and frequency ranges: Pc3, with period range from 10-45 s, are the most useful in exploring sedimentary basins. Irregular pulsations (like Pi2) occur mostly during the night. Their period range is usually 40-150 s. Table 1 summarises the classification of geomagnetic pulsations and their time of appearance.

- Vibrations: (frequencies higher than 5 Hz). From 5 Hz to about 10 kHz the major cause is lightening which occurs mostly in Indonesia, in central Africa and in the Amazon region; they are called atmospherics. Resonance in the earth cavity, called Schumann resonance, has a fundamental frequency at 8 Hz; it is usually present and useful in exploration of the shallow subsurface (Fig. 1.2).

Table 1. Types of continuous (Pc) and irregular (Pi) pulsations
(Rokityansky 1982)

Type	Period (s)	Normal time of appearance
Pc1	0.2-5	Morning-Day
Pc2	5-10	Morning
Pc3	10-45	Morning-Day
Pc4	45-150	Morning-Day
Pc5	150-600	Morning-Day-Evening
Pc6	> 600	Night
Pi1	1-40	Night, Morning, Day
Pi2	40-150	Night, Day
Pi3	> 150	Night

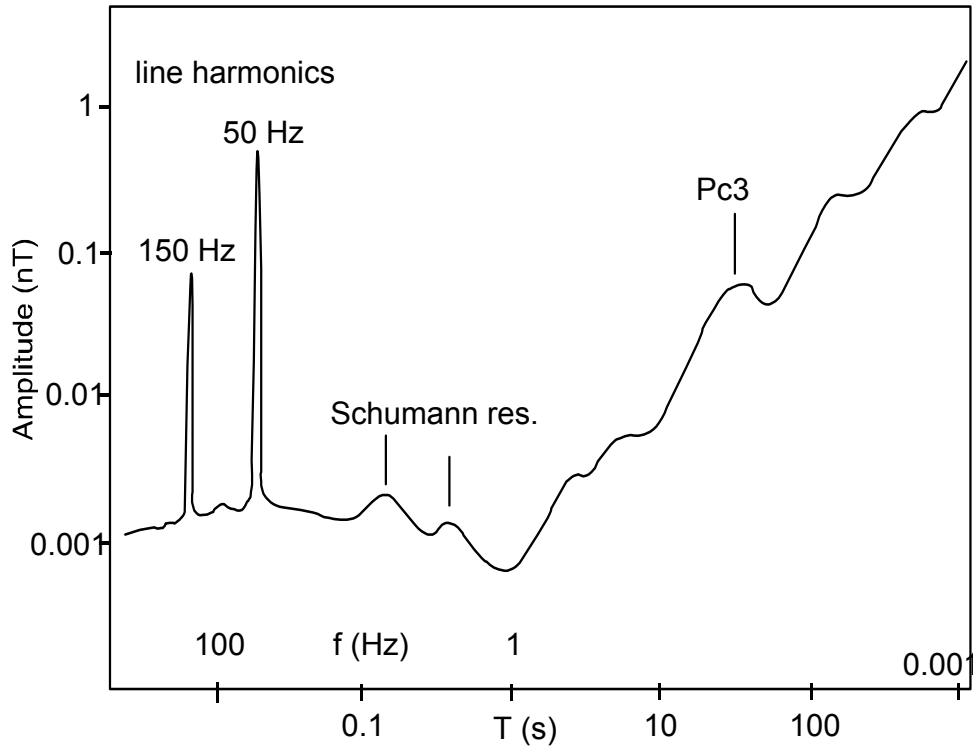

Figure 1.2. Example of naturally-occurring magnetic field spectrum. Spikes to the left are power line harmonics. Other features are Schumann resonance and pulsations (Malergue et al. 1986).

1.4 Earth surface impedance

The physical description of the process that leads to the measurements of the resistivity is as follows (Morrison 1997):

- The current system in the magnetosphere or the lightening discharges produce time varying magnetic fields at the surface of the earth.
- Through Faraday's law of induction the time varying magnetic field induce currents in the conducting earth.
- The electrical field produced in the earth, which by Ohm's law is equal to the product of the resistivity and the current, is measured using two separate electrodes.
- Under the assumption that the inducing magnetic fields are horizontal and uniform, the ratio of the electric field (E) to the magnetic field (H), called the impedance (Z), is a unique function of the conductivity structure surrounding the measurement point.

- At a given frequency two orthogonal measurements of magnetic fields (Hx) and (Hy), are related to electrical fields (Ex) and (Ey) on the same axes through a tensor impedance defined by two equations:

$$E_x(\omega) = Z_{xx}(\omega)H_x(\omega) + Z_{xy}(\omega)H_y(\omega)$$
$$E_y(\omega) = Z_{yx}(\omega)H_x(\omega) + Z_{yy}(\omega)H_y(\omega \quad (1)$$

or in matrix form

$$\begin{vmatrix} E_x \\ E_y \end{vmatrix} = \begin{vmatrix} Z_{xx} Z_{xy} \\ Z_{yx} Z_{yy} \end{vmatrix} \begin{vmatrix} H_x \\ H_y \end{vmatrix} \quad (2)$$

- Low frequencies penetrate more deeply into the earth than high frequencies. Impedance of high frequencies yields conductivity near the surface; at low frequencies it yields an integrated conductivity over depth. A process of extracting the progressive change in conductivity with depth by measuring the impedance from high frequencies to low is called a MT sounding (MTS).

1.5 Theory of MT

Overview of the basic aspects and the application of the EM induction theory in geophysical studies are described by several textbooks and literature (Kaufman and Keller 1981; Vozoff 1986 and 1991; Yungul 1996; Sharma 1997; Morrison 1997). It is assumed that the medium is linear, isotropic and homogeneous, which is a reasonable assumption. Note that for non-linear or anisotropic media the EM theory is extremely complicated. An electromagnetic field can be described with four vectors, as follows:

E = electrical field intensity (V/m),
H = magnetic field intensity (A/m),
B = magnetic induction or flux density (Wb/m^{2}or Tesla), and
D = electric displacement (C/m^2)

The four Maxwell equations relate these vectors to their sources, a distribution of electric charge density ρ_c (C/m^3) and an electrical current density J (A/m^2) as follows:

$$\nabla \times E = -\frac{\partial B}{\partial t} \quad \text{(Faraday's law)} \quad (3)$$

$$\nabla \times H = J + \frac{\partial D}{\partial t} \quad \text{(Ampere's law)} \quad (4)$$

$$\nabla B = 0 \quad \text{(Coulomb's law)} \quad (5)$$

$$\nabla D = \rho_c \tag{6}$$

The other three relationships connecting the field vectors are

$$D = \varepsilon E; B = \mu H; J = \sigma E \tag{7}$$

where

ε is the dielectric permittivity (F/m)

μ is magnetic permeability (H/m), and

σ is an electric conductivity (S/m), defined as the reciprocal of resistivity.

By using these relations we can reduce Maxwell's equations in terms of only two vectors E and H by assuming a time-dependence of the form $E(t) = E_0 e^{i\omega t}$, where $\omega = 2\pi f$ is the angular frequency of the field. The vectorial equations for E and H take the following form:

$$\nabla^2 E = i\omega\mu\sigma E - \varepsilon\mu\omega^2 E \tag{8}$$

$$\nabla^2 H = i\omega\mu\sigma H - \varepsilon\mu\omega^2 H \tag{9}$$

where $i = \sqrt{(-1)}$. These are the basic equations for the propagation of electric and magnetic field vectors in an isotropic medium with physical properties ε, μ and σ.

In eqs (8) and (9), the terms involving $i\omega\mu\sigma$ are related to the conduction currents, whereas the terms involving $\varepsilon\mu\omega^2$ are related to the displacement currents.

The rock parameters ε, μ and σ and angular frequency ω can be grouped into one term k^2 given by

$$k^2 = -i\omega\mu(\sigma + i\omega\varepsilon) = \mu\varepsilon\omega^2 - i\omega\mu\sigma \tag{10}$$

The field equations (8) and (9) can then be rewritten as

$$\nabla^2 E + k^2 E = 0; \nabla^2 H + k^2 H = 0 \tag{11}$$

the quantity $k = \sqrt{\mu\varepsilon\omega^2 - i\omega\mu\sigma}$ is called the propagation parameter. At low frequencies ($f < 10^5 Hz$) $\mu\varepsilon\omega^2 << \omega\mu\sigma$, because ε for most rocks is small and σ for favourable targets in EM surveys is usually $\sigma > 10^{-2}$ S/m. In this regime, known as inductive regime, the propagation parameter is $k = \sqrt{-i\omega\mu\sigma}$.

In the other case, at high frequencies of the order of 10 MHz or higher (such as geo-radar), $\mu\varepsilon\omega^2 >> \omega\mu\sigma$ in earth material of low conductivity σ <1 mS/m. For this case, the propagation parameter is given by $k = \sqrt{\mu\varepsilon\omega^2}$.

In the case of the electrical field E having x-component and the magnetic field only y-component, and the amplitudes of the two fields varying with z (positive downward), the field eqs (11) have a simple solution, given by

$$E_x = E_0 e^{-ikz} = E_0 e^{-i(\beta+i\alpha).z} \tag{12}$$

with E_0 the amplitude of the electric field component at z=0. E_x is the amplitude of the electric field at some reference point in the medium and k is the propagation factor. The solution for magnetic field can be written likewise by replacing E with H:

$$H_y = H_0 e^{-ikz} = H_0 e^{-i(\beta+i\alpha).z} \tag{13}$$

The real part of k is associated with a phase factor β, and the imaginary part is associated with the attenuation factor α of the wave. The expression for phase and attenuation factors are simplified to

$$\alpha = \beta = \sqrt{(\omega\mu\sigma/2)} \tag{14}$$

The depth δ at which the amplitude of the field is reduced to 1/e (i.e. 37%) of its surface value is known as the skin depth. This depth referred to as the depth of penetration of an EM wave, is related to the attenuation factor α by

$$\delta(km) = \frac{1}{\alpha} = \left(\frac{2}{\mu_0\sigma\omega}\right)^{0.5} \approx 0.5 * \left(\frac{\rho}{f}\right)^{0.5} \tag{15}$$

where $\rho = 1/\sigma$ is the resistivity in Ωm, f is the frequency of the EM wave in Hz, and $\mu = \mu_0 = 4\pi * 10^{-7}$ for non-magnetic media. Skin effect and the recorded variations of the geo-electromagnetic fields control the depth of penetration. Table 2 shows a list of skin depths for various periods and resistivities of host rocks, typical for EM studies.

Table 2. Skin-depth for various periods and resistivities of the host rocks.

	T=1s	**T=10s**	**T=100s**
$\rho = 10\Omega m$	$1.6km$	$5km$	$16km$
$\rho = 100\Omega m$	$5km$	$16km$	$50km$
$\rho = 1000\Omega m$	$16km$	$50km$	$160km$
$\rho = 10000\Omega m$	$50km$	$160km$	$500km$

1.6 Principles of MT sounding

The propagation of MT fields is basically governed by eq. (11) in the regime of low frequencies, for which the propagation parameter k is given by $k = \sqrt{-i\omega\mu\sigma}$. The physical parameters involved are $\mu = \mu_0$ (for non magnetic medium), $\rho = 1/\sigma$ and $\omega = 2\pi f$. According to Cagniard (1953), for a wave polarised in the horizontal plane (x-y) and propagating downward in the ground, the plane wave scalar apparent resistivity is related to the square of the MT impedance function $Z(\omega)$. The apparent resistivity $\rho_a(\omega)$ is given by

$$\rho_a(\omega) = \frac{1}{\omega\mu_0}\left|Z(\omega)\right|^2 \tag{16}$$

where $Z(\omega) = E_x / H_y$ is the ratio of orthogonal components of the electric and magnetic fields at a given frequency. For 1D geology, the resistivity distribution solely depends on the depth and the MT impedance yields $Z_{xy} = -Z_{yx}$. Eq. (16) defines an apparent resistivity ρ_a that can be calculated from simultaneous measurements of Ex and Hy (or Ey and Hx) at different frequencies. The depth of penetration increases as frequency decreases.

The complex elements of the impedance tensor in eqs (1) and (2) are converted into apparent resistivities $\rho_{a,ij}(\omega)$ and phases $\varphi_{ij}(\omega)$

$$\rho_{a,ij}(\omega) = \frac{1}{\omega\mu_0}\left|Z_{ij}(\omega)\right|^2 = 0.2T * \left|Z_{ij}(\omega)^2\right| \tag{17}$$

$$\varphi_{ij}(\omega) = \arg(Z_{ij}(\omega)) = \tan^{-1}\{\mathrm{Im}\, Z_{ij}(\omega) / \mathrm{Re}\, Z_{ij}(\omega)\} \tag{18}$$

here the index i is x or y, j is y or x, and $T = 2\pi/\omega$ is the period of the wave.

The subsurface may be approximately 2D. If the system of measuring axes is rotated at a particular angle θ, elements Z_{xx} and Z_{yy} are zero. Eq. (2) can be rewritten as

$$\begin{vmatrix} E_x \\ E_y \end{vmatrix} = \begin{vmatrix} 0 & Z_{xy} \\ Z_{yx} & 0 \end{vmatrix} \begin{vmatrix} H_x \\ H_y \end{vmatrix}, \quad \text{with } Z_{xy} \neq Z_{yx} \tag{19}$$

where Z_{xy} and Z_{yx} are called principal impedances (two modes in MT) and the new axes aligned in this particular direction are called the principal axes of anisotropy. The TE mode (transverse electric) is observed when the currents are flowing parallel to the strike direction of the structure. The TM mode (transverse magnetic) occurs when the currents are perpendicular to the strike structure. Thus, the TE mode is specified by Ex and Hy, whereas TM mode uses Ey and Hx.

If the impedance tensor is rotated to a new system x', y' through a positive (clockwise) angle θ around the vertical axis z, eq. (2) becomes: $Z' = RZR^T$ (20)

where the rotation matrix is defined as: $\underline{R} = \begin{pmatrix} \cos\theta & \sin\theta \\ -\sin\theta & \sin\theta \end{pmatrix}$ (21)

Expanding eq. (20), each rotated impedance tensors element can be expressed as:

$$Z'_{xx} = Z_{xx}\cos^2\theta + Z_{yy}\sin^2\theta + (Z_{xy} + Z_{yx})\sin\theta\cos\theta \tag{22}$$

$$Z'_{xy} = Z_{xy}\cos^2\theta - Z_{yx}\sin^2\theta - (Z_{xx} - Z_{yy})\sin\theta\cos\theta \tag{23}$$

$$Z'_{yx} = Z_{yx}\cos^2\theta - Z_{xy}\sin^2\theta - (Z_{xx} - Z_{yy})\sin\theta\cos\theta \tag{24}$$

$$Z'_{yy} = Z_{yy}\cos^2\theta + Z_{xx}\sin^2\theta - (Z_{xy} + Z_{yx})\sin\theta\cos\theta \tag{25}$$

From $\underline{Z}$ it is possible to derive some invariant relationships with respect to rotation. Others invariants are given by Fischer and Masero (1994). For 2D structures the principal axes are those that maximise $|Z_{xy}|$ and minimise $|Z_{yx}|$, and therefore maximise the anisotropy (A):

$$A = |Z_{xy}|^2 / |Z_{yx}|^2 \tag{26}$$

The anisotropy is an indicator of the extent of the lateral resistivity contrast of the geological formations under study. Eq (26) means an anisotropic MT response and not an anisotropic resistivity of the medium. The angle that maximises $|Z_{xy}|$ is generally different from the one that maximises A.

According to Sims and Bostick (1969) both $|Z_{xx} + Z_{yy}|$ and $|Z_{xy} - Z_{yx}|$ are independent of θ. The magnitude of the ratio of these quantities is also independent of θ and is called the skewness (S):

$$S = \frac{|Z_{xx} + Z_{yy}|}{|Z_{xy} - Z_{yx}|} \tag{27}$$

if S is small (<0.3), it is concluded that the subsurface is typically 1D or 2D at that site and frequency, otherwise it is 3D. If the subsurface is really 1D or 2D, then S=0. Very often, the MT response in the short period range 0.001 to 1 s shows 1D behaviour, whereas the longer periods (1 to 1000 s) are multi-dimensional (2D and 3D).

1.7 Estimation of impedance function and coherency

The power spectrum approach is used to estimate the tensor impedance elements Z_{ij}. For example, from eq (1) $E_x = Z_{xx}H_x + Z_{xy}H_y$, we could first multiply by $H_x^\bullet$ and take the average, i.e. $\overline{E_x H_x^\bullet} = Z_{xx}\overline{H_x H_x^\bullet} + Z_{xy}\overline{H_y H_x^\bullet}$ and then multiply by $H_y^\bullet$ and take averages: $\overline{E_x H_y^\bullet} = Z_{xx}\overline{H_x H_y^\bullet} + Z_{xy}\overline{H_y H_y^\bullet}$. Now we have two equations in the two unknowns Z_{xx} and Z_{xy} and we can solve for them, viz.

$$Z_{xx} = \frac{\left(\overline{E_x H_x^\bullet}\right)\left(\overline{H_y H_y^\bullet}\right) - \left(\overline{E_x H_y^\bullet}\right)\left(\overline{H_y H_x^\bullet}\right)}{\left(\overline{H_x H_x^\bullet}\right)\left(\overline{H_y H_y^\bullet}\right) - \left(\overline{H_x H_y^\bullet}\right)\left(\overline{H_y H_x^\bullet}\right)},$$

$$Z_{xy} = \frac{\left(\overline{E_x H_y^\bullet}\right)\left(\overline{H_x H_x^\bullet}\right) - \left(\overline{E_x H_x^\bullet}\right)\left(\overline{H_x H_y^\bullet}\right)}{\left(\overline{H_x H_x^\bullet}\right)\left(\overline{H_y H_y^\bullet}\right) - \left(\overline{H_x H_y^\bullet}\right)\left(\overline{H_y H_x^\bullet}\right)} \qquad (28)$$

and similarly for Z_{yx} and Z_{yy} (Morrison 1997):

$$Z_{yx} = \frac{\left(\overline{E_y H_x^\bullet}\right)\left(\overline{H_y H_y^\bullet}\right) - \left(\overline{E_y H_y^\bullet}\right)\left(\overline{H_y H_x^\bullet}\right)}{\left(\overline{H_x H_x^\bullet}\right)\left(\overline{H_y H_y^\bullet}\right) - \left(\overline{H_x H_y^\bullet}\right)\left(\overline{H_y H_x^\bullet}\right)},$$

$$Z_{yy} = \frac{\left(\overline{E_y H_y^\bullet}\right)\left(\overline{H_x H_x^\bullet}\right) - \left(\overline{E_y H_x^\bullet}\right)\left(\overline{H_x H_y^\bullet}\right)}{\left(\overline{H_x H_x^\bullet}\right)\left(\overline{H_y H_y^\bullet}\right) - \left(\overline{H_x H_y^\bullet}\right)\left(\overline{H_y H_x^\bullet}\right)} \qquad (29)$$

These are the same expression as derived by Sims and Bostick (1969) from a direct least square formulation.

After estimating the tensor elements (Z_{ij}) we substitute in eq (1) in order to compute Ex and Ey. Both components are predicted from Hx and Hy. Therefore, any discrepancy between the observed E and predicted E must be due to contamination of either E or H by noise. The coherency between predicted and measured components is a sensitive noise indicator (Vozoff 1972). The noise level on channel Ex can be assessed by the predicted or multiple coherencies γ^2 (Bendat and Piersol 1986):

$$\gamma^2_{P,E_x} = \frac{Z_{xx}\left\langle H_x E_x^* \right\rangle + Z_{xy}\left\langle H_y E_x^* \right\rangle}{\left\langle E_x E_x^* \right\rangle} \qquad (30)$$

There is an analogous expression for Ey. The predicted coherency gives a measure of how eq (1) fits the linear relation between the horizontal components of E and H fields. Its value is real and bounded by $0 \le \gamma^2 \le 1$.

Generally in MT, measurements of E and H always contain some random noise, independent of the desirable signals. Kao and Rankin (1977) have described an iterative scheme by assuming that the noise existed in the auto-powers only. Their technique brings a significant improvement of data quality. Data are essentially biased by faulty auto-powers, but are unaffected when there is bias in the cross-powers as well. To overcome noise in both auto-powers and cross-powers, Gamble et al. (1979a, b) proposed a remote magnetic reference. This leads to an improvement of the estimation of the magnetotelluric impedance Z. The method employs two sets of simultaneously recorded magnetic signals at distinct sites to correct for bias errors introduced by locally-occurring noise.

The resulting impedance matrix Z can be rotated mathematically to maximise the difference between off-diagonal elements Z_{xy} and Z_{yx}. In ideal 1D or 2D cases, the diagonal elements Z_{xx} and Z_{yy} should tend towards zero. The rotation brings the new reference axes in concordance with the geological strike. Unfortunately, static effects may often affect the electric field measured on one of the lines, or both, by adding a frequency-independent offset of unknown magnitude.

The geological strike is obtained by using a special technique (Groom and Bailey 1989 1991). The skewness parameter (S) gives a measure for the deviation of the structure from two-dimensionality (2D).

1.8 Geomagnetic depth sounding (GDS)

GDS is basically a method of investigation of the subsurface conductivity distribution, which measures the magnetic field components (Hx, Hy and Hz) without measuring the electrical fields (Ex and Ey). Under ideal source conditions Hz is totally due to currents flowing parallel to the strike. Therefore, the horizontal direction in which H is most coherent with Hz is the direction perpendicular to the strike. The procedure for determining this direction is described by Vozoff (1972). It is assumed that Hz (vertical component) is linearly related to Hx (north) and Hy (east) at each frequency. The Fourier transforms can be written as

$$H_z(\omega) = AH_x(\omega) + BH_y(\omega) \tag{31}$$

where A and B are unknown complex coefficient that can be calculated. They refer to tipper, meaning that a part of the horizontal component of H is tipped into the vertical. For 1D earth, the coefficients A and B are zero.

The transfer functions A and B are more frequently displayed in the form of vectors, the induction arrows (Parkinson 1962 and Schmucker 1970). The complex amplitude of the induction arrows is

proportional to the local effects of induction on Hz at that location and the orientation (with A as the north and B the east directed components) is perpendicular to the current flow. The induction arrows can be expressed as a pair of real (in-phase) and imaginary (quadrature) vectors (Arora and Adam 1992):

a length: $T(\mathrm{Re}) = \sqrt{\mathrm{Re}(A)^2 + \mathrm{Re}(B)^2}$ and an angle: $\vartheta(\mathrm{Re}) = \arctan\dfrac{\mathrm{Re}(B)}{\mathrm{Re}(A)}$ (32)

a length: $T(\mathrm{Im}) = \sqrt{\mathrm{Im}(A)^2 + \mathrm{Im}(B)^2}$ and an angle: $\vartheta(\mathrm{Im}) = \arctan\dfrac{\mathrm{Im}(B)}{\mathrm{Im}(A)}$ (33)

In the 2D case the real component points away from regions which are good conductors.

1.9 Distortion in MT transfer function

The study of near surface lateral conductivity variations and their static shift effects on 2D MT transfer functions was discussed by several authors (Jones 1988; Sternberg et al. 1988; Beamish and Travassos 1992b; Groom and Bahr 1992). The sources of these effects are near surface inhomogeneities leading to galvanic distortions. Different decomposition techniques have been proposed to solve the distortion effects in MT transfer functions (Bahr 1988; Groom and Bailey 1989, 1991; Chave and Smith 1994 and Smith (1995). The Groom and Bailey (GB) approach differs in significant manner from other distortion methods in that the effects of galvanic distortions are separated into determinable and indeterminable parts. In GB analysis, the determinable part of galvanic distortion is characterised by two galvanic distortion parameters, so-called shear and twist, induction by the regional strike and the regional impedances. The method assumes a local small-scale 3D anomaly over 2D earth. Accurate interpretation of MT data requires an understanding of the directionality and dimensionality inherent to the data. McNeice and Jones (2001) proposed an extension to GB decomposition in which a global minimum is sought to determine the most appropriate strike direction and telluric distortion parameters for a range of frequencies and a set of sites. Also, they showed how the analysis could be extended to cover the case of frequency-independent distortion caused by the magnetic effects of the galvanic charges.

The galvanic distortion of the electrical field by a 3D surficial feature was first introduced by Larsen (1977) for 1D subsurface and was extended later to 2D subsurface (Richards et al. 1982). The basic model can be written as

$$Z_{meas} = RCZ_{2D}R^T \tag{34}$$

where R is a rotational tensor, the superscript T denoting transpose; C is a real 2x2 telluric distortion tensor and Z_{2D} is the searched regional 2D impedance tensor in strike coordinates. Groom and Bahr (1992) and Chave and Smith (1994) give the meaning of this equation. Groom and Bailey (1989) proposed matrix decomposition based on the factorisation of the telluric tensor C as a product of modified Pauli spin matrices:

$$C = gTSA = g\begin{Bmatrix} 1 & -t \\ t & 1 \end{Bmatrix}\begin{Bmatrix} 1 & e \\ e & 1 \end{Bmatrix}\begin{Bmatrix} 1+s & 0 \\ 0 & 1-s \end{Bmatrix} \tag{35}$$

where g is a scalar termed 'site gain' and T, S and A are tensor factors termed twist, shear and anisotropy respectively. The twist (T) and shear (S) tensors form the determinable portion of the distortion matrix, whereas the site gain (g) and anisotropy (A) together form the indeterminable parts of the distortion matrix that scale the apparent resistivity curves and form of the static shift (McNeice and Jones 2001). Absorbing the site gain (g) and anisotropy (A) into regional impedance, the measured impedance tensor under the GB factorisation becomes

$$Z_{meas.} = RTSZ_{reg}R^T = \begin{Bmatrix} \cos\theta & -\sin\theta \\ \sin\theta & \cos\theta \end{Bmatrix}\begin{Bmatrix} 1-te & e-t \\ e+t & 1+te \end{Bmatrix} * \begin{Bmatrix} 0 & A \\ -B & 0 \end{Bmatrix}\begin{Bmatrix} \cos\theta & \sin\theta \\ -\sin\theta & \cos\theta \end{Bmatrix} \tag{36}$$

where Z_{reg} is the scaled regional 2D impedance tensor (g A Z_{2D}).

Groom and Bailey (1989) showed that the measured impedance tensor obeys the decomposition model; the tensor is uniquely described by the seven parameters of the factorisation. These parameters are the two descriptors of telluric twist (t) and shear (e), the regional strike (θ) and the four parameters contained in the two complex scaled regional impedances (TE and TM) modes.

Electrical charge build-up on small-scaled conductivity anomalies affects the observed electric field (static shift). It takes the form of a multiplicative constant applied to the apparent resistivity i.e. a vertical shifting of the apparent resistivity relative to the regional values, without any effect on the phases. Magnetic distortion effects definitely require a more complicated treatment. Most of literature is limited to the galvanic distortion of the electric field. However, Zhang (1993) described magnetic distortion to discriminate current channelling from induction effect.

GB method tries to fit the observed data i.e. the eight real numbers of the complex 2x2 impedance tensor at each period, with seven parameters of the model consisting of a 3D local structure superimposed over a regional 2D structure. Assuming that the distorting effect is frequency-independent, one expects to get a frequency-independent regional strike angle from the decomposition, as the regional structure is assumed to be two-dimensional.

1.10 Two-dimensional magnetotelluric modelling

Interpretation of MT results requires the application of numerical methods to solve 2D or 3D induction problems, since the surveyed structure usually may not be considered 1D. The MT impedance tensors rarely conform to the ideal 2D case, but a strike direction may be obtained at regional scale for at least a certain range of periods. In this case, the two impedance elements Z_{xy} and Z_{yx} must be interpreted to infer the electrical structure (Osella and Martinelli 1993). Different methods have been developed to handle 2D structures: finite differences (Brewitt-Taylor and Weaver 1976), finite elements

(Wannamaker et al. 1987) and integral equations (Hohmann 1975; Weidelt 1975). The goal is always to solve the Helmholtz equation governing the EM field distribution.

In the 1990's there were many types of algorithms in use for regularised 2D inversion of MT data. They included straight forward extensions of linear search methods developed previously for 1D regularised inversion (deGroot-Hedlin and Constable 1990; Uchida 1993), efficient approximated methods (Smith and Booker 1991; Farquharson and Oldenburg 1996) and methods based on direct iterative minimisation of a regularised penalty functional matrix {e.g., non-linear conjugate gradients (NLCG)}. They used a steepest descent method to avoid the expense of constructing large matrices (Rodi and Mackie 2001).

Approximate methods (Rapid Relaxation Inversion, RRI) have been developed (Smith and Booker 1991) which used computing approximations to the sensitivity matrix to search for a minimum of a penalty functional. RRI approach can be very fast. Schnegg (1993) described a computing method for 2D magnetotelluric modelling directed by polynomials. The polynomials represent layer resistivities and thicknesses in logarithm space. Their coefficients are searched with a steepest descent algorithm. Forward calculation described by Wannamaker et al. (1985) is employed in this method.

All algorithms seek to minimise some function representing data misfit. In the OCCAM straight forward method (deGroot-Hedlin and Constable 1990), minimisation is accomplished using some variant on a linear Gauss-Newton approach. REBOCC (Reduced Basic Occam's Inversion) presents a new and much more efficient variant on the OCCAM scheme.

By expressing the solution as a linear combination of rows of the sensitivity matrix smoothed by the model covariance (the representor), REBOCC transforms the linearized inverse problem from the M-dimensional model space into the N-dimensional data space. This method is referred to as DASOCC, the data space OCCAM'S inversion. More importantly the data space formulation suggests a simple approximate method for constructing the inverse solution (Siripunvaraporn and Egbert 2000).

We give here a brief review of the inversion approach used in REBOCC. The goal of the inversion is to find the minimum structure model subject to a desired misfit level. The unconstrained functional $U(m,\lambda)$ can be written as

$$U(m,\lambda) = (m-m_0)^T C_m^{-1}(m-m_0) + \lambda^{-1}\left\{(d-F[m])^T C_d^{-1}(d-F[m]) - X_*^2\right\} \quad (37)$$

where the first term $(m-m_0)^T C_m^{-1}(m-m_0) = X_m^2$ is a model norm, $m = [m_1, m_2 \ldots\ldots m_M]$ is a series of M constant resistivity blocks, m_0 is a base (or prior model, and C_m is a mode covariance matrix which characterises the expected magnitude and smoothness of resistivity variations relative to m_0.

The second term is $\lambda^{-1}\left\{(d-F[m])^T C_d^{-1}(d-F[m]) - X_*^2\right\}$ (38)

where λ is a Lagrange multiplier, and $(d-F[m])^T C_d^{-1}(d-F[m]) = X_d^2$ is the fit of the theoretical data responses $F[m]$ to the observational data N ($d = [d_1, d_2 ... d_N]$).

The minimum structure inverse problem is to minimise X_m^2 subject to $X_d^2 = X_*^2$, where X_*^2 is the desired level of misfit. For more details see the original paper (Siripunvaraporn and Egbert 1999).

REBOCC is an inversion scheme for 2-D magnetotelluric data, able to invert apparent resistivity and phase simultaneously for TE and TM modes. In order to test the merits and weaknesses of this method, we generated synthetic data from a synthetic 2D model. The model (Fig 1.3a) consists of three horizontal layers and one vertical conductor (as expected from a geological fault structure). The model responses, including resistivity and phase shift for TM and TE modes were generated for 27 stations and 29 periods using the finite-element forward modelling program of Wannamaker et al. (1986). To simulate our real data set, only nine stations were used for the inversion test (Fig 1.3b). Then, 10% noise was added to the data (Fig. 1.3c). After REBOCC inversion of these synthetic data, the vertical conductor shows up again in both non-noisy and noisy data. Note that the small right-shift of the fault is an artefact of Wannamaker's regularisation mesh.

1.11 Main objectives of this research

For a long time now we know that crustal fluids trigger seismic activity in active faults. Since crustal fluids constitute excellent ionic conductors due to dissolved minerals, we apply magnetotellurics, a convenient EM sounding technique for detecting crustal conductors. The original project was planned solely in Egypt, as the publicly available seismic catalogue of Aswan area was very accurate. Furthermore, seismic activity was not completely random, but linked to the Lake level. For the sake of completeness and comparison, the study was extended to the Remiremont fault zone, where a seismic crisis developed along a 3 km-long vertical plane in 1984.

The next two chapters are concerned with the geological setting in Wadi Kalabsha site (Aswan), and will analyse 20 years of seismicity in the region and its relationship to the loading induced by reservoir water level fluctuation. Chapter 4 and 5 present the analysis of MT data in Wadi Kalabsha and Remiremont areas. Finally, Chapter 6 will be the discussion and interpretation of the results of both areas and a comparison with other similar locations like SAF (San Andreas Fault, California).

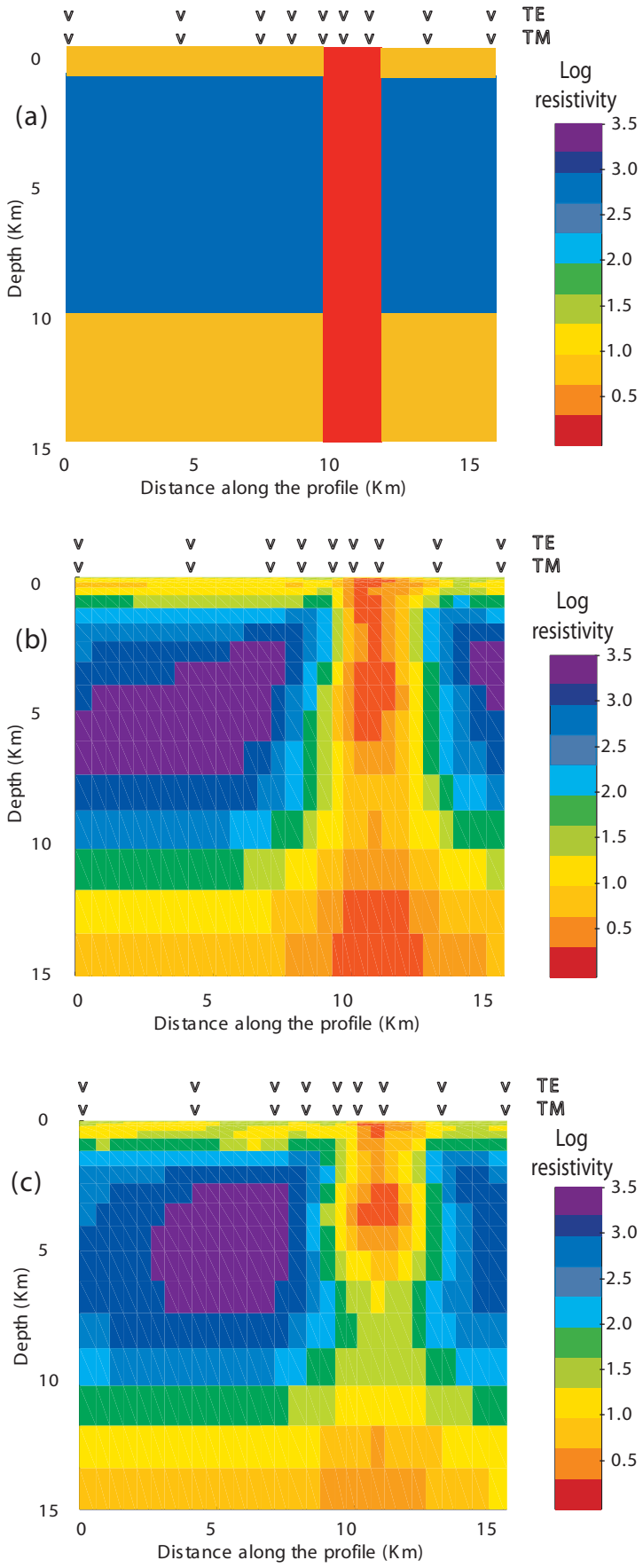

Figure 1.3. Test of REBOCC inversion.
(a) Model used to generate synthetic data responses of TE and TM at the marked sites. There are three layers with resistivities 50, 1000 and 50 Ωm. A 2-km wide vertical conductor (1 Ωm) representing a fault is buried to 15 km depth.
(b) REBOCC inversion without and (c) with 10 % added noise.

2. The Wadi Kalabsha area

2.1 Geological and structural setting

Egypt is located in the north-eastern part of Africa. The Africa (Arabia-Nubian) massif is bisected by the Red Sea rift and its continuation (as continental rift) of Suez and Aqaba. The geological map of Egypt (Fig 2.1) shows the basement occupying about 10 % of the area, and the Phanerozoic sediments and volcanics about 90 %. These structures represent the most active regions of the Precambrian shield outcropping in their greatest extend in Ethiopia, Sudan, the eastern part of Egypt and Sinai (Said 1962).

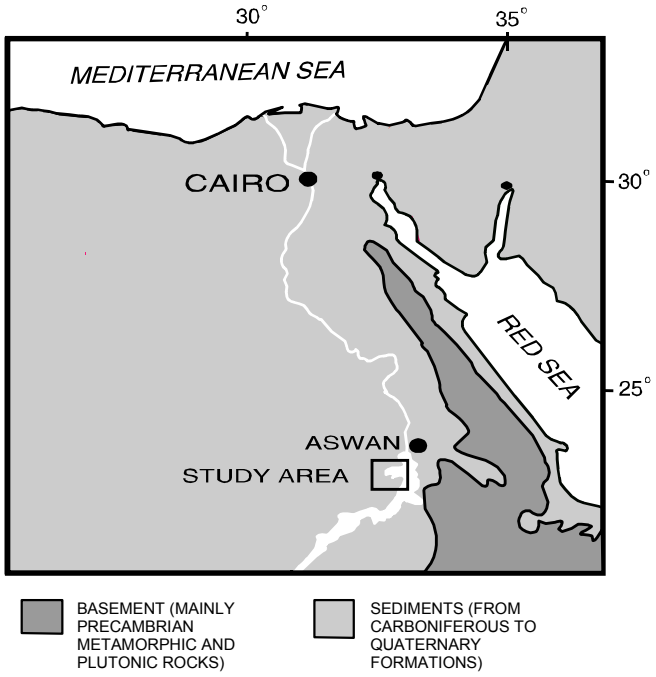

Figure 2.1. A simple geological map of Egypt (after El-Shazly 1977), showing the location of Wadi Kalabsha area.

According to Smith (1984) Egypt is classified into three tectonic provinces. They are defined as Arabia-Nubian massif (shield), the stable and unstable shelf (Fig 2.2). The Arabia-Nubian craton is exposed over southern Egypt, eastern Desert and southern part of Sinai Peninsula. The stable shelf is situated north of Arabia-Nubian massif and exhibits a gentle tectonic deformation. The sedimentary sequence on the stable shelf is relatively thin (500 m.) near the Arabia-Nubian shield and increasing to north near the unstable shelf about 2500 m. It is composed of sands and shales in its lower part and carbonates in its upper part. The unstable shelf is located north of stable shelf with transition between the two structural depositional units. It extends from Siwa oasis through Farafra oasis and Suez into central Sinai.

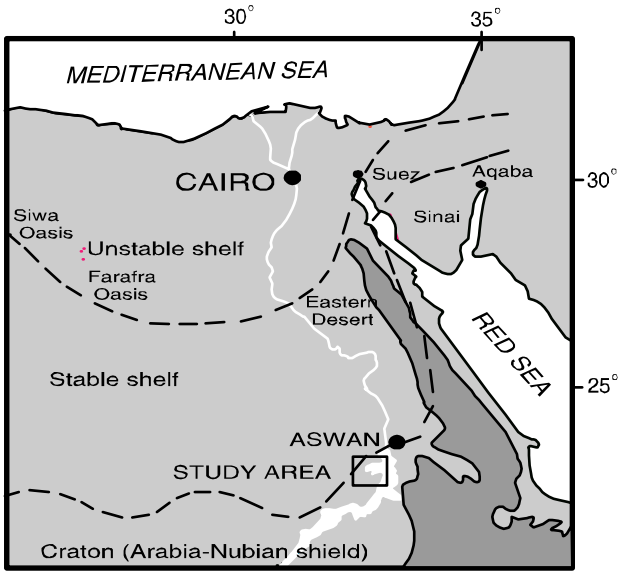

Figure 2.2. The main tectonic provinces of Egypt (after Smith 1984).

2.2 Seismicity in Egypt

Egypt is one of the few countries in the world where earthquake activity has been documented during the past 4200 years. Information on historical earthquakes is present in the annals of ancient Egyptian and Arab literatures. Earthquake activity is important in Egypt (e.g. 1210, 600 BC, 778, 967, 1303, and 1874, 1899 AD), with earthquakes destroying part of big cities such as Cairo and Alexandria (Ambraseys et al. 1994). According to Thenhaus et al. (1993) about 83 events were reported to have occurred in and around Egypt and to have caused damage of variable degrees in different localities. Several significant earthquakes occurred in Egypt from (1955-1998) as follows:

1955 September 12, offshore Alexandria earthquake:
This earthquake had a magnitude of 6.1 and was felt in the entire east of Mediterranean basin, Cyprus, the Dodecanese Island and as far as Athens (Maamoun 1979). In Egypt, it was strongly felt and led to loss 22 lives and damage in the Nile Delta between Alexandria and Cairo.

1969 March 1969, Shadwan Island earthquake:
The magnitude of this earthquake was 6.3 with a maximum intensity of IX assigned to a small area on Shadwan Island (Red Sea) (Ben-Menahem et al. 1971). On Shadwan Island, landslides, earth slumps and rock falls were common; *fissures* and cracks in the soil were found, and their main direction was parallel to the Red Sea-Gulf of Suez. This earthquake was preceded by a large sequence of foreshocks and also followed by a large sequence of aftershocks.

1981 November 14, Aswan earthquake:
On November 14, 1981, moderate earthquakes with a local magnitude of 5.4 occurred in the unpopulated area of Wadi Kalabsha along the most active faults (Kalabsha fault) in the area,

approximately 70 km Southwest of Aswan city followed by numerous aftershocks sequences (Kebeasy et al. 1982). The main shock and most of the immediate aftershocks lies between depths of 15 and 26 km beneath Gebel Marawa. Shallow earthquakes occur between 0.5-12 km on the other segment of Kalabsha fault and north of Marawa area (Toppozada et al. 1984).

1992 October 12, Cairo Earthquake:

Cairo earthquake that occurred in 12 October 1992 had a magnitude 5.3 and intensity VIII (Thenhaus et al. 1993). It was strongly felt and damaged many houses along the Nile (Cairo, Giza and Elsaff). Fissures and cracks in the soil were found in Dahshour, El-Tabbia, Manshiyat Fadill and Qubabat areas (Youssef et al. 1992).

1995 November 22, Gulf of Aqaba earthquake:

The largest earthquake occurred in the Gulf of Aqaba with magnitude 7.0. Ground fractures, damage and collapse of buildings and liquefaction were recorded in Aqaba (Jordan), Elate (Israel) and along the western coast of the Gulf of Aqaba in Sinai Peninsula (Osman and Ghobarah 1996).

1998 May 28 Mediterranean earthquake:

On May 28, a moderate size earthquake of magnitude 6 occurred in the Mediterranean Sea. It was strongly felt in the northern part of Egypt and caused a strong shaking in Cairo and in many localities along the Nile Delta (Awad and Tealeb 2000).

Recent seismic hazard assessment in Egypt was done by El-Sayed et al. (2001), using spatial distribution of recorded earthquakes (Fig. 2.3a) to identify the major seismic zones. The four major zones are: the Gulf of Aqaba-Levant zone, the northern Red Sea-Gulf of Suez zone, the Suez-Cairo-Alexandria fault zone and the eastern Mediterranean-Cairo-Fayoum zone (Maamoun and Ibrahim 1978; Kebeasy 1990; Mohammed 1993). In addition to these zones, Kebeasy (1990) defined other local seismic zones for example, the Gilf El-Keber, Aswan and Qena local source zones. Also distant earthquakes have caused considerable damage in Egypt and three larger seismogenic zones {i.e. Egypt-Mediterranean coastal, Cyprus and Crete) must be added. El-Sayed also discussed seismogenic zones with common focal mechanisms in Egypt and its vicinity (Fig. 2.3b).

2.3 Geological and tectonic setting of Kalabsha area

The Wadi Kalabsha area lies on the western side of Lake Aswan, 70 km Southwest of Aswan city. It became tectonically interesting after the occurrence of the 14 Nov. 1981 earthquake along Kalabsha fault, the main active faults of the area. It is located within the stable platform of the African (Arabia-Nubian) massif. The Nile follows the contact between the surface exposure of the granite of the Eastern Desert to the east, and the sedimentary cover of the Nubian sandstone to the west. The location map of the study area is shown in (Fig 2.1).

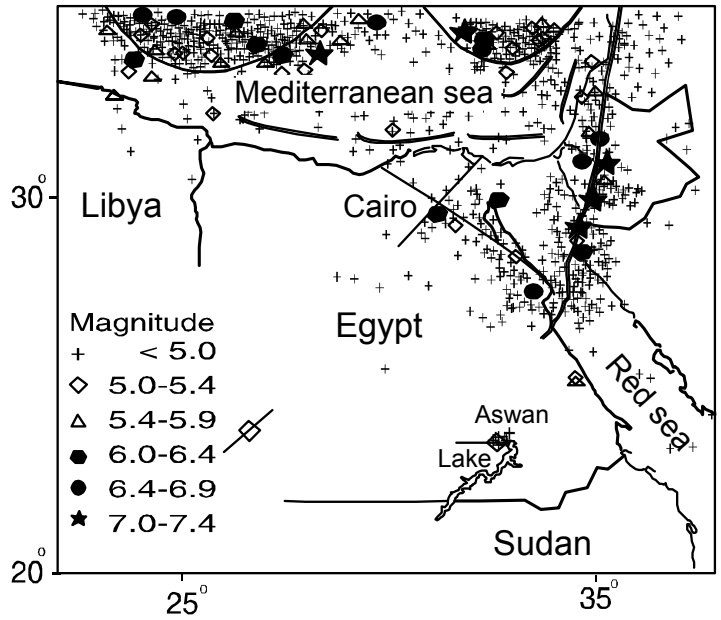

Figure 2.3a. Distribution of earthquake epicenters around Egypt for the period 1900-1998. Lines denote the major tectonic elements (adapted from El-Sayed et al. 2001).

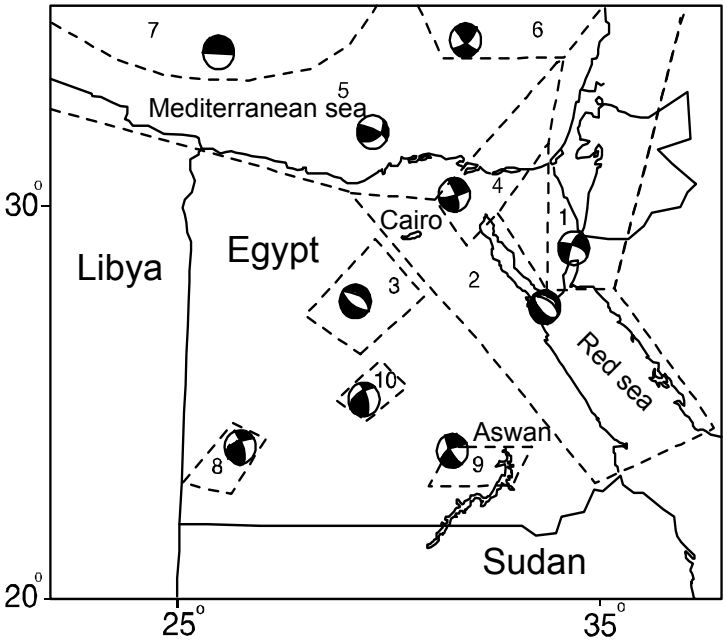

1: Gulf of Aqaba-Levant, 2: Northern Red Sea-Gulf of Suez
3: Suez-Cairo-Alexandria, 4: Eastern Mediterranean-Cairo-Fayoum, 5: Mediterranean costal, 6: Cyprus, 7: Crete,
8: Gilf El-Keber, 9: Aswan, 10: Qena zone

Figure 2.3b. Seismogenic zones with focal mechanisms in Egypt and its vicinity (adapted from El-Sayed et al. 2001).

Geomorphologically, the area is flat with relief varying from 150 to 350 m. The landscape is broken by the rise of black hills, ridges and low scarps of sandstone. The topography is complicated by structural dislocations and also by the presence of several alkali granites and a syenite ring complex. Sediments ranging in age from Late Cretaceous to Eocene cover the area. They unconformably overlie the Precambrian Basement (Fig. 2.4). In turn, the Nubian formation unconformably overlies the irregular basement rock surface. Overlying the Nubian formation in some places are Kurkur and Gharra formations. Quaternary is represented by calcite and Nile deposits (Issawi 1978 and 1982).

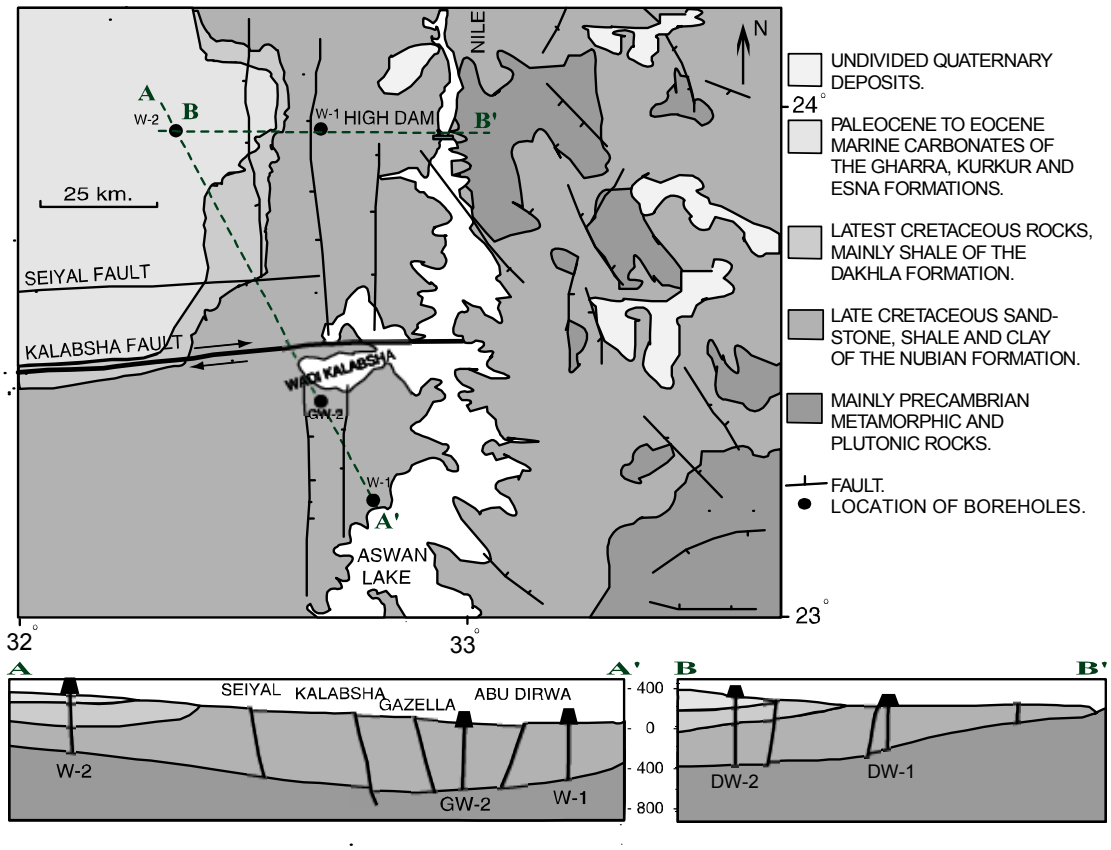

Figure 2.4. Regional geological and tectonic setting of Wadi Kalabsha area (after Issawi 1969).

The Nubian plain is interrupted by sandstone hills composed of resistant beds of the Nubian formation as well as limestone hills as Gebel Marawa (274 m). Several large and small E-W trending 'wadies' have developed as Wadi Kalabsha and Seiyal. The Sinn El-Kaddab Plateau is made of limestone and extends westward from the western edge of the Nubian Plain. The eastern margin of the plateau is a steep east-facing escarpment called Sinn El-Kaddab Escarpment (Issawi 1969). Igneous and metamorphic intrusions are distributed in several localities on the western side of the lake and constitute the main geologic formation of the eastern side. Information from the boreholes indicates that the average thickness of the Nubian formation and whole sedimentary column is approximately 500 m (Fig. 2.4).

The area is characterised with different geological units. The main units are Precambrian basement, late Cretaceous, Palaeocene, Eocene and Quaternary deposits (El-Shazly et. al 1977).

Starting from the oldest unit:

Basement: most of the basement rocks exposed in the area belong to the Aswan monumental granites of the post-orogenic plutonites. The Aswan granites that are widely distributed in the area display aligned N-S and E-W fractures and faults. They form an elongated N-S stretch in both sides of the lake and Wadi Kalabsha extending northward to Aswan city.

Cretaceous sediments: They are mainly represented by Nubian beds covering the greater part of the investigation area. The succession of Nubian sediments had been deposited unconformably over the previously mentioned basement rocks. The latest Cretaceous rocks are conformably overlain by a thin succession of alternating beds of clay, shales and sandy shales of the Dakhla formation.

Palaeocene to Eocene sediments: Represented with Esna, Kurkur and Garra formations, as follows:

Esna formation: it is composed mainly of greyish to dark shales with thin sandy or calcareous intercalations. It forms an elongated stretch along lower part of Sinn El-Kaddab escarpment.

Kurkur formation: it is composed mainly of limestone with minor intercalations of shales and sandstones. The Kurkur formation is well developed in the area of study. It makes also some ridges to the west of Gebel Marawa and stretches to the north and south.

Garra formation: it represents of a succession of white limestone and chalky limestone beds with common intercalations of calcareous clays and shales.

Quaternary sediments: mainly represented by calcite deposits. Calcite deposits are found near Sinn El-Kaddab escarpments, Gebel Marawa. In some places, they are represented with alluvial deposits on both sides of the Lake Aswan. The alluvial deposits are composed mainly of clay, silty and sandy materials. The structural pattern of the area investigated is governed mainly by faulting as well as uplifted basement rocks. The faults that crosscut the area are classified into several systems depending on their trend (El-Shazly 1977). There are two sets of faults crossing the Nubian formation and basement complex, mainly oriented in E-W and N-S directions (Figure 2.4):

East-West trending faults:
The E-W trending fault systems are the most predominant faults in the area to the Northwest of the Lake Aswan. These faults extend from the Nubian Plain across the Sinn El-Kaddab Plateau. The two major faults of the system are the Kalabsha and Seiyal faults. These faults are strike-slip with right-

lateral movements, and affect the sandstone beds of the Nubian Plain as well as the basement complex. These faults are the active faults in the area.

North-south trending faults:
The N-S trending fault system is well represented in the area of Lake Aswan and affects the sandstone beds of the Nubian Plain. These faults (Gebel El-Barqa, Kurkur, Khor El-Ramla, Gazella, and Abu-Dirwa) are normal faults. Most of these faults show evidence of activity (Tealeb et al. 1999).

2.4 Previous research work in Kalabsha area

There have been many research works in the Kalabsha area, starting after the 14 Nov. 1981 earthquake along Kalabsha fault. Kebeasy et al. (1982) determined the location of the earthquake using the intensity distribution map. Toppozada et al. (1984) estimated the seismicity and focal mechanism of two seismic zones in the period from late Dec. 1981 to June 1982. The first zone was concentrated at Gebel Marawa, near the intersection of the easterly trending Kalabsha fault with a northerly trending fault. The second seismic zone clustered some 15 km further to the east near the intersection of the Kalabsha with another northerly trending fault. Simpson et al. (1987) located a sequence of seismic activity by using a radio-telemetry network of nine stations surrounding the north part of the lake including the Kalabsha area from July 1982 to May 1984. The most active zone extended along Kalabsha fault. The earthquake foci are concentrated into two depth ranges (14 to 22 km and from 4 to 7 km). Composite fault plane solutions indicated strike-slip with right-lateral movements.

Kebeasy et al. (1982, 1987) and Simpson et al. (1987) identified the lake Aswan seismicity as a *reservoir-triggered* sequence. Gharib and Simpson (1990) determined the crustal structure around lake Aswan by using two reversed seismic refraction profiles oriented north-south across the Kalabsha fault. Interpretation of these seismic refraction data indicated a total crustal thickness of 26-28 km.

The local crustal structure in Kalabsha area was studied also using explosives (Kebeasy et al. 1991). It showed that the crust beneath the Aswan reservoir area was characterised by three reflectors located below the sediment cover. P and S wave velocities for these layers are 5.3 and 3.0 km/s respectively from the base of the Nubian sandstone to a depth of 4.7 km; 6.2 and 3.5 km/s to a depth 16 km and 6.4 and 3.7 km/s for depth greater than 16 km. Seismic tomography has imaged both velocity contrasts across Kalabsha fault (Awad and Mizoue 1995b). The authors mentioned that the shallow seismic activity occurs within the low velocity zone, and that the deeper seismic activity is concentrated within the deeper high-velocity anomaly (Fig. 2.5).
AbdelRahman et al. (1991) carried out a detailed gravity survey in the active region of Wadi Kalabsha to study its subsurface structure. A Bouguer anomaly map of the area was constructed and several interpretation techniques were applied to analyse these anomalies (Fig. 2.6). The results indicated that

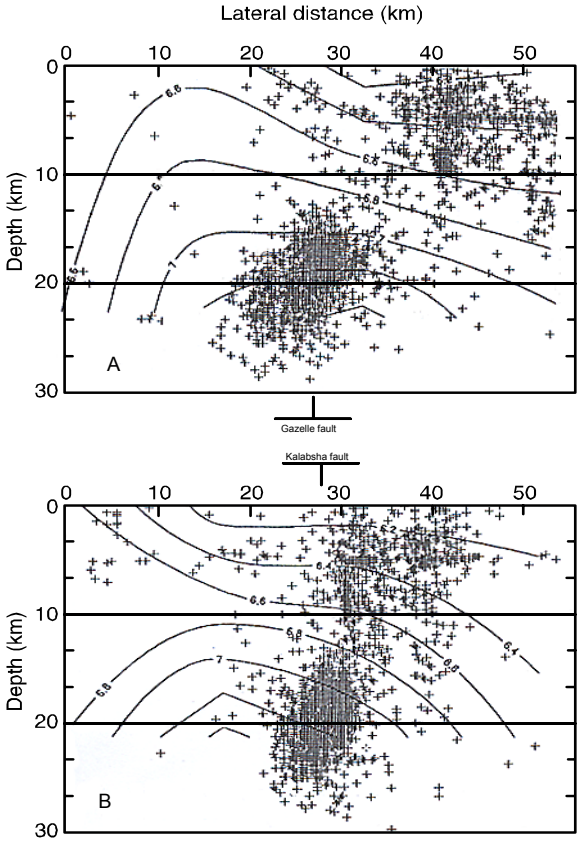

Figure 2.5. Correlation between seismicity and P-wave velocity structure in Aswan region. (A) and (B) are E-W and N-S cross-sections, respectively (after Awad and Mizoue 1995b). Values of contour lines give the P-wave velocity (km/s).

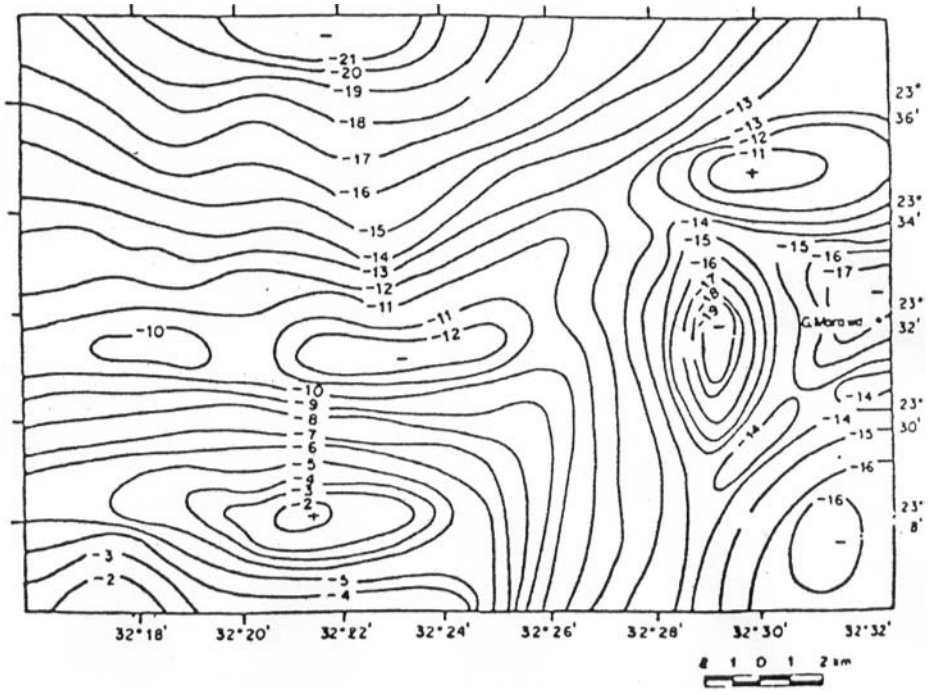

Figure 2.6. Bouguer anomaly map of the Kalabsha area. Contour interval 1 mgal (AbdelRahman 1991).

the active area located west of Gebel Marawa is bounded by a set of faults striking NE-SW, N-S and E-W. The throws of these faults range from 160 to 370 m. In its centre there are two minima having E-W strike, i.e. the same direction as Kalabsha fault. Presumably, small sedimentary basins corresponding to the gravitational minima have been generated by the intersection of longitudinal fractures. This is very characteristic of the Kalabsha area.

Evans et al. (1991a-b) and Beavan et al. (1991b) published three papers concerning estimation of aquifer parameters through the application of time series analysis to water level data from boreholes. They mentioned that the stratigraphy of the Nubian formation in the area consists of three horizontal units of 400m total thickness. The lowermost unit, overlying the granitic basement is an aquifer of fluvial sandstones and has a large-scale (several kilometres) horizontal permeability. The middle unit is an aquiclude that extends unbroken under the lake and leaks at periods larger than several years. The uppermost unit is the water table aquifer, which is composed of 25-30% porosity sandstone with interspersed clay lenses and displays large-scale permeability.

The authors discuss the aquifer poro-elastic and diffusivity rock properties from forced fluctuations of borehole water level in five wells sampled in Nubian sandstone (high porosity) near the Aswan reservoir. They find that the propagation is about 0.6 km/day. A regional 3D hydrological model for the study area is developed, based on the 23-year record of water changes that occurred at six wells in response to the changing level of Lake Aswan.

Noshy (1993) analyses the total magnetic intensity data of the Kalabsha area and reveals that the area is occupied by a thin sedimentary succession and a complicated pattern of fault systems of different trends. The analysis of the geoelectrical resistivity data and of geomagnetic measurements reveals that the sedimentary section can be represented by five geoelectric layers. These layers vary from very dry sands to clay, with sandstone being saturated by groundwater. Also, this investigation shows that there is no correlation between groundwater flow and tilting of layers that had been indicated in the constructed relief maps of the basement.

For Kebeasy and Gharib (1991) the seismicity in Aswan is concentrated in five distinct clusters along the Kalabsha fault, a major EW, right-lateral strike slip structure. The composite focal mechanism solution shows that all the mechanisms are strike slip faulting on nearly vertical planes with small components of dip slip components. These fault systems occur under the influence of maximum compressional NW-SE stress whereas the direction of tension is NE-SW (Gharib 1992). Hassib (1997) found that the orientation of compressional stress and the tensional stress prevailing in the Kalabsha area are in the ESE-WNW and NNE-SSW respectively. Mahmoud (1994) deduced that the orientation of the compressional stress has the direction NWW-SEE and that the type of seismotectonic deformation is a strike slip faulting with thrust component.

After the November 1981 in Kalabsha area, the Egyptian National Research Institute of Astronomy and Geophysics (NRIAG) initiated a long program for the study of the recent movement and detection of deformations associated with earthquakes in the area at the northern part of Lake Aswan (Tealeb 1994, 1998). This program includes the establishment and measurement of the local geodetic networks around potential faults. The analysis of the repeated levelling measurements indicates annual rates from 0.5 to –1.5 cm/y (Fig. 2.7). This means that the Wadi Kalabsha area is subsiding towards the south with small annual rate not exceeding 1.5 cm/year. Horizontal movements are significantly correlated with the earthquake activity in the area, with prevalence of shear deformations along the Kalabsha and Seiyal faults. The intensity of the shear deformation varies with time (2.0-7.0 cm/year and 1.0-5.0 cm/year respectively) (Fig. 2.8) and well correlated with the seismicity of the area (Vyskocil 1991; Tealeb 1994).

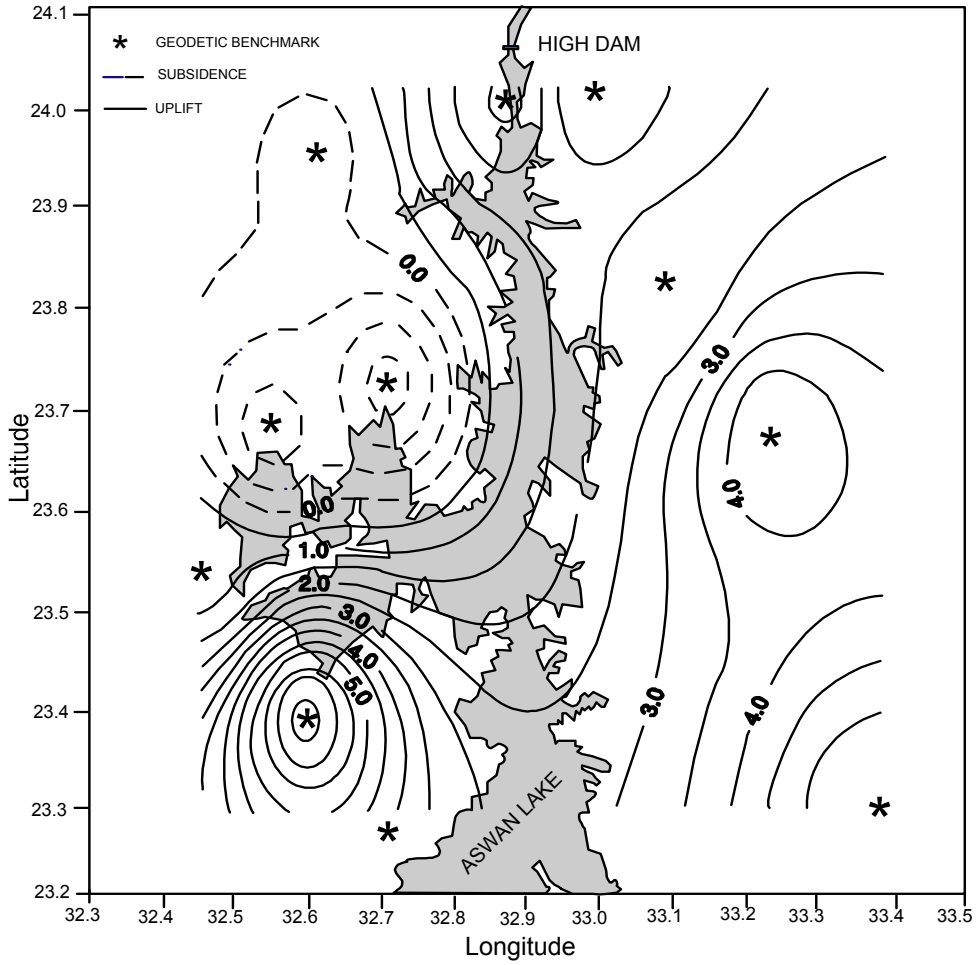

Figure 2.7. Isolines of vertical changes (mm) for the Kalabsha area to the north of Lake Aswan during the period from November 1997 to May 1998 (after Tealeb et al. 1999).

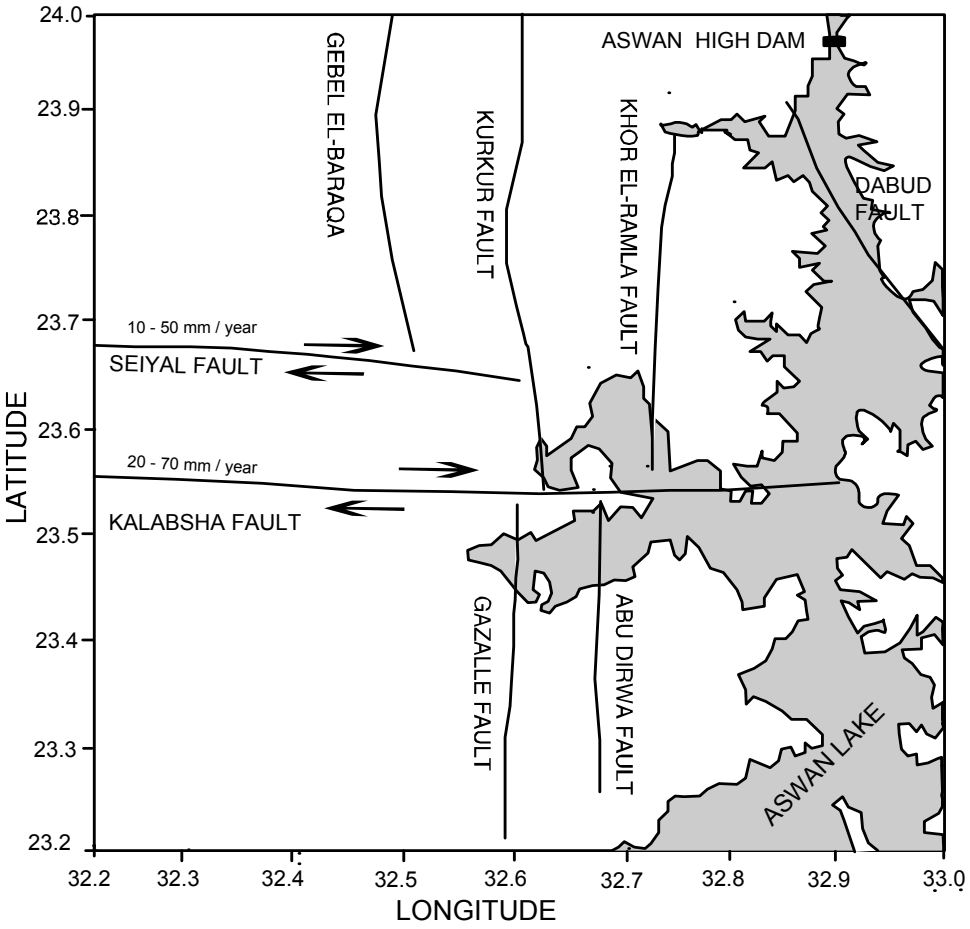

Figure 2.8. Horizontal movements along Kalabsha and Seiyal faults (after Tealeb et al. 1999).

3. Seismicity patterns at Lake Aswan

The study of earthquake activity in Aswan is of great importance for the safety of the high dam. This study started in 1981 with the November 14 event, of magnitude 5.4 which occurred not far from the High Dam (about 60 km). Reservoir Induced Seismicity (RIS) over 6th magnitude has occurred in Greece, India, China and on the Zambia/Zimbabwe border. Seven cases produced earthquakes with magnitude M > 5.5. Gupta (1992) lists 33 cases of RIS that triggered M >4 earthquakes.

3.1 Induced earthquakes

Most earthquakes are related to plate tectonics and are independent of human activity. However, as is well known, humans can induce earthquake activity in five major ways: Fluid injection or extraction, mining or quarrying, and through the impoundment of reservoir dams. For example, earthquakes listed in Table 3 may have been induced or triggered. RIS is the triggering of earthquake by the physical processes that accompany the impoundment of large reservoirs. Roeloeffs (1988) and Simpson et al. (1988) have suggested how some reservoirs could induce earthquakes immediately upon filling, due to change in elastic stress after a delay, as a result of pore pressure and fluid diffusion (Fig. 3.1). Some others are active after many years but only when the water level has changed. Some examples of this type are Aswan (Egypt), Koyna (India) and Oroville (California) (Simpson 1986).

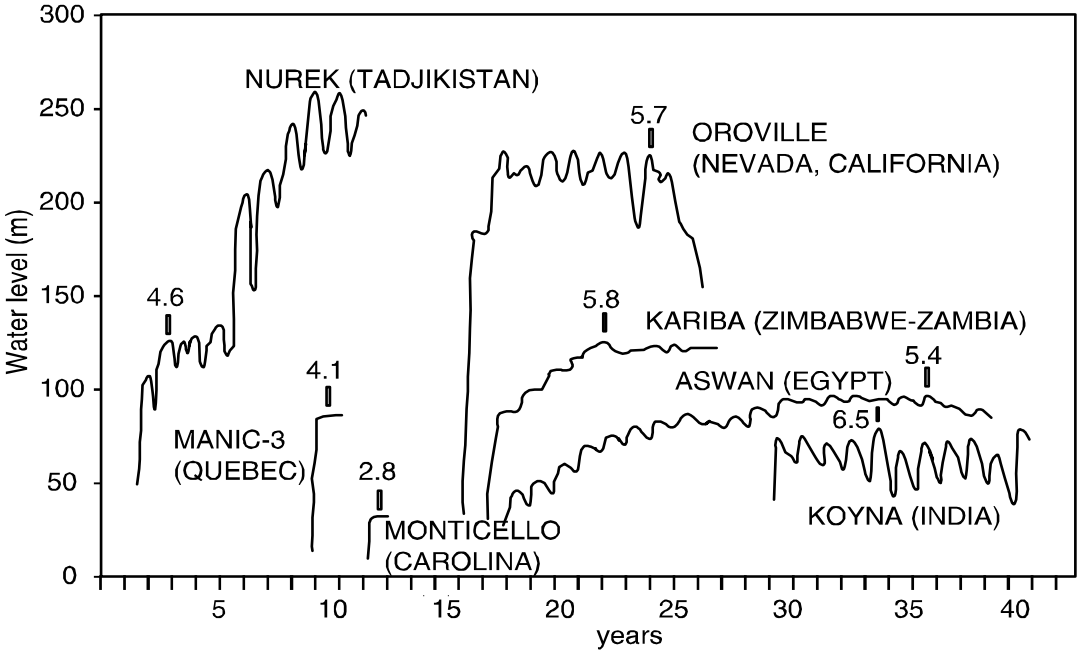

Figure 3.1. Water level and periods of main earthquake activity at selected reservoirs showing induced seismicity (Simpson 1986).

The filling of large reservoirs modifies the tectonic stress regime, either by increasing the vertical stress through the effect of loading, or by increasing the pore pressure that results in a decrease of the effective normal stress. The net effect on fault zones is to increase or decrease stress, depending on the

orientation, the geometry of the reservoir and the fault system (Snow 1972; Gupta and Rastogi 1976; Bell and Nur 1978 and Roeloeffs 1988). Mechanism of RIS involves a complex interaction between shear stress, normal stress and pore pressure.

Table 3 Examples of earthquakes that may have been induced or triggered (Schwartz et al. 1996)

Year	Magnitude	Location	Mechanism	Published papers
1971-78	M=4.6	Nurek (Tadjikistan)	Reservoir impoundment	Simpson and Negmatullaev (1981)
1978	M=4.1	Monticello (S. Carolina)	Reservoir impoundment	Simpson et al.(1988) Talwani and Acree (1985) Zoback and Hickman (1982)
1981	M=5.3	Aswan (Egypt)	Reservoir impoundment	Simpson et al.(1990) Simpson and Leith (1985)
1983	M=6.5	Cualinga (California)	Oil withdrawal	McGarr (1991)
1984	M=7	Gazli (Uzbekistan)	Gas withdrawal	Simpson and Leith (1985)
1992	M=6.5	Big Bear (California)	Triggered by M=7.4 Landers Eqs. 40 km away	King et al. (1994) Stein et al. (1992) Harris and Simpson (1992)
1993	M=6.1	Killari or Latur (SW India)	Reservoir impoundment	Seeber et al. (1995)

In the case of strike slip faulting of Aswan area, water loading and pore pressure tend to decrease fault stability, increasing the seismic activity on these faults (e.g. Roeloeffs 1988). Pore pressure increases instantly from the compaction of pore space due to the reservoir load and then from the raised water column with a delay due to diffusion (McGarr et al. 2002).

Kebeasy et al. (1982) suggested that Lake Aswan seismicity is reservoir-triggered. This suggestion gained credence after the occurrence of a remarkable seismic sequence in August 1982 during seasonal increase of reservoir level. Simpson et al. (1988) identified this sequence in the Lake Aswan area as a delayed reservoir-triggered seismicity.

3.2 Seismicity in Aswan area

Historical activity in Aswan starts very early. In Luxor (200 km north of Aswan), earthquake damage was reported in 600 BC, 967 and 1899 AD. It is worth mentioning that an earthquake damaged the temple at Abu Simbel, 230 km south of Aswan in 1210 BC (Maamoun et al. 1984). Before 1981, information on seismicity in the Aswan region is limited by the lack of local seismographs. The first

seismographs installed in Aswan capable of recording small local earthquakes are the Russian short period SMK instruments (1975). The operation of the stations was irregular. According to Gibowicz et al. (1982), few small shocks (M < 3) were detected in the Southwest part of Lake Aswan in January 1981 during a reconnaissance survey. The main contemporary earthquake (M = 5.4) in this area occurred on November 14, 1981. It was preceded by three foreshocks: two events on November 9 (M = 3.6 and 4.2) and one event on November 11 (M = 4.5). It was followed by an extended sequence of aftershocks (Kebeasy et al. 1982).

Kebeasy and Gharib (1991) mentioned that some low magnitude seismic activity had occurred near the reservoir after filling and prior to the November 1981 sequence. During three years (1978-1981) water level was always above 175 m. Reservoir extended to flood while the Wadi Kalabsha depression became fully saturated. After flooding of the eastern segment of Kalabsha fault, active seismicity started and continues till now (Figure 3.2). A telemetry network (Aswan Seismograph Network, ASN) was established around the northern part of Lake Aswan in July 1982. Each field station is equipped with a single-component vertical seismometer (Mod. S13), amplifier / VCO, radio-telemetry and solar battery. Since 1989, the ASN consists of 13 field stations. The seismic data are recorded at the Aswan Regional Seismological Centre (ARSC), Southwest of Aswan City (Figure 3.3).

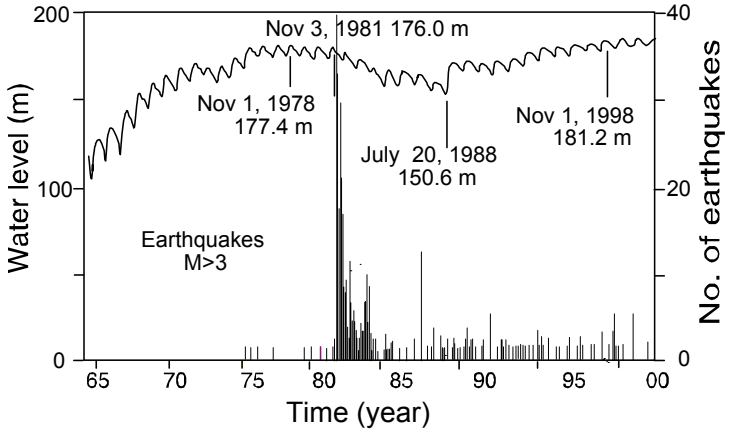

Figure 3.2. Water level relative to sea and seismicity (M >= 3) on Lake Aswan (1965-2002). Water level is measured relatively to Sea level. Level of 110 m corresponds to the lake floor.

3.3 The Aswan Catalogue

The data listed in the Aswan catalogue has been recorded by at least four stations, allowing an accurate earthquake location using the computer programme Hypo71 (Lee 1990). The earthquake catalogue of the ASN (1982-2001) contains about 4514 events (1.0 < M < 5.5). This catalogue was used to construct the spatial earthquake distribution (Fig. 3.4). The seismicity is concentrated along the easternmost section of Kalabsha fault, particularly at the intersection between the NS and EW fault systems. The easternmost segment of the Kalabsha fault is located beneath a large area covered by water and extends

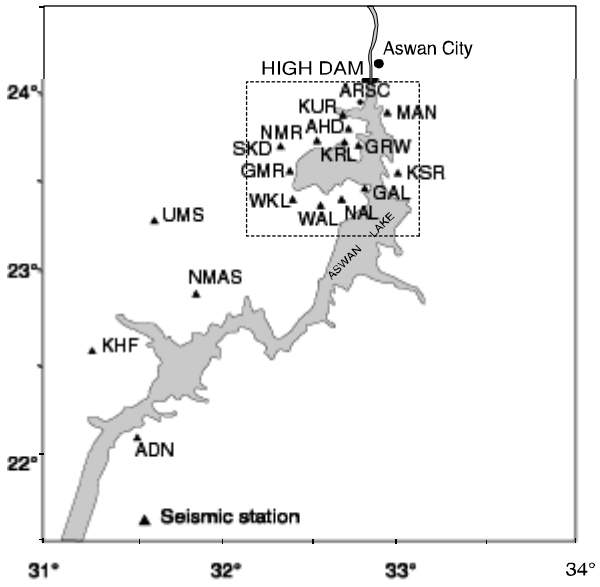

Figure 3.3. Seismograph network around Lake Aswan (Adapted from Kebeasy and Tealeb 1997).

over more than 150 km. It consists of several segments forming a conjugate fault pattern. The seismicity is concentrated in five main cluster zones: Gebel Marawa (K1), Khore El-Ramla (K2), East Gebel Marawa (K3), Abu Dirwa (K4) and an old stream zone (K5). Cluster K1 seismicity takes place at depths greater than 15 km. The seismicity of the other zones is characterised by shallow depths (<15 km) and ranges on the NS fault system intersecting Kalabsha fault (Simpson et al. 1990; Kebeasy and Gharib 1991). The average focal mechanism solution for each zone is shown in Fig. 3.5.

3.4 Structure determination from earthquakes

The interpretation of a cloud of earthquake hypocenters in terms of causative structures is not an easy task. Earthquake locations are subject to uncertainties and errors, arising from bad timing, an incorrect velocity structure or poor network geometry. The errors can be minimised by exercising care during the location process but uncertainties can never be completely eliminated at the observational data (Jones and Steward 1997). According to Deichmann and Baer (1990), a high RMS (root mean square) of the travel time residuals is an indication of inconsistency among the travel time readings or of inaccuracy in the velocity model. A low RMS alone does not guarantee an accurate location.

In order to determine significant structures from Aswan seismic data catalogue, we have chosen *erz* and *erh* (errors in vertical and horizontal distance) less than 3 km and magnitude greater than 2.0. After selection, about 1874 events were used in this analysis and a focal-depth map constructed. The distribution of earthquakes with focal depth clearly reflects the Kalabsha fault plane (Fig. 3.6). An automatic minimising routine was used with events from clusters K1 and K3 to find out the best fault plane in terms of the smallest RMS of the average distance to the earthquakes. This plane can be interpreted in term of a simplified model of the Kalabsha fault.

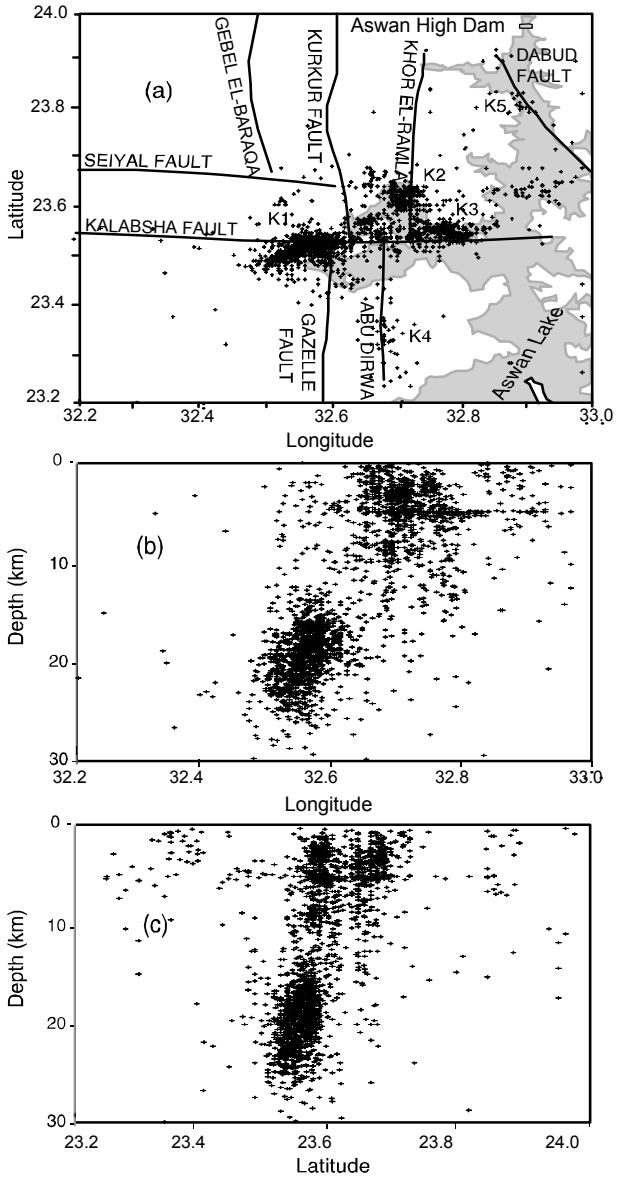

Figure 3.4. (a) The spatial distribution of earthquakes in Aswan area. The K_i denote cluster zones. (b, c) Epicenters and focal depths for (M >= 2).

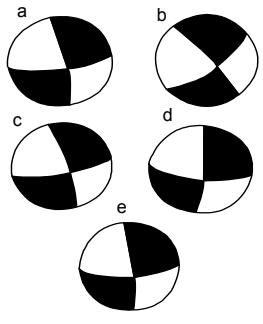

Figure 3.5a-e. Average focal mechanism analysis for the Aswan seismicity. Solution for the fault segment K1, K2, K3, K4 and K5 in Fig. 3.4a (after Awad and Mizoue 1995a).

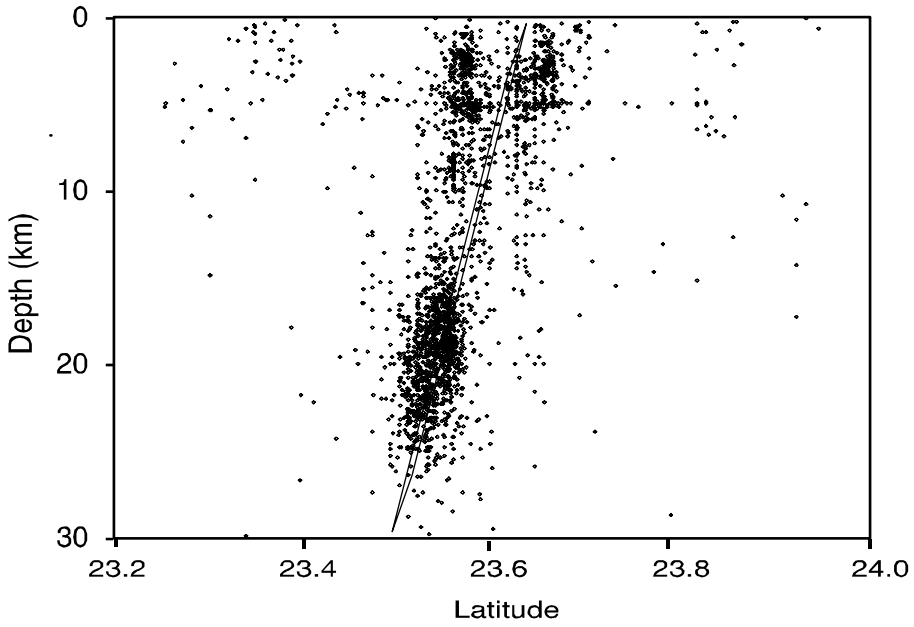

Figure 3.6. 2D spatial distribution of the earthquakes in Wadi Kalabsha area. The fault plane is obtained by minimizing the sum of squared distances.

If, however, we include cluster K2, the average fault plane direction is consistent with the results obtained from MT data (next chapter). Regional strike was determined at about N60ºE, instead of the almost perfect EW orientation of the fault at the surface.

3.5 Frequency-magnitude distribution

Because one of our objectives is to analyse the seismicity pattern over time, we must determine for which magnitude range the Aswan catalogue is complete. This is usually performed by examining the magnitude frequency distribution of earthquakes. The Gutenberg-Richter (1956) relationship of the frequency-magnitude distribution is defined as log N = a – bM, where N is the cumulative number of earthquakes, a and b are constants related to the activity and earthquake size distribution, respectively. The b-value is estimated by using the maximum likelihood method of Aki (1965):

$$b = \frac{1}{\ln(10)\left(\langle M \rangle - M_{\min}\right)}\ , \tag{39}$$

where <M> is the average magnitude and M_{min} the smallest considered magnitude. The M_{min} value is estimated to be 2.2 for both shallow (1400 events) and deep (1200 events) earthquakes (Figure 3.7a-c).

The variations in b-value are related to differences in stress, pore pressure and material heterogeneity (Wiemer and Benoît 1996; Wiemer et al. 1998). Therefore they can give important constraints when analysing the seismotectonic and hazard potential of a certain region (Malone and Wiemer 2001). Interestingly, high b-values are often correlated with the presence of magma in volcanic regions (Jolly and McNutt 1999 and Wyss et al. 2000).

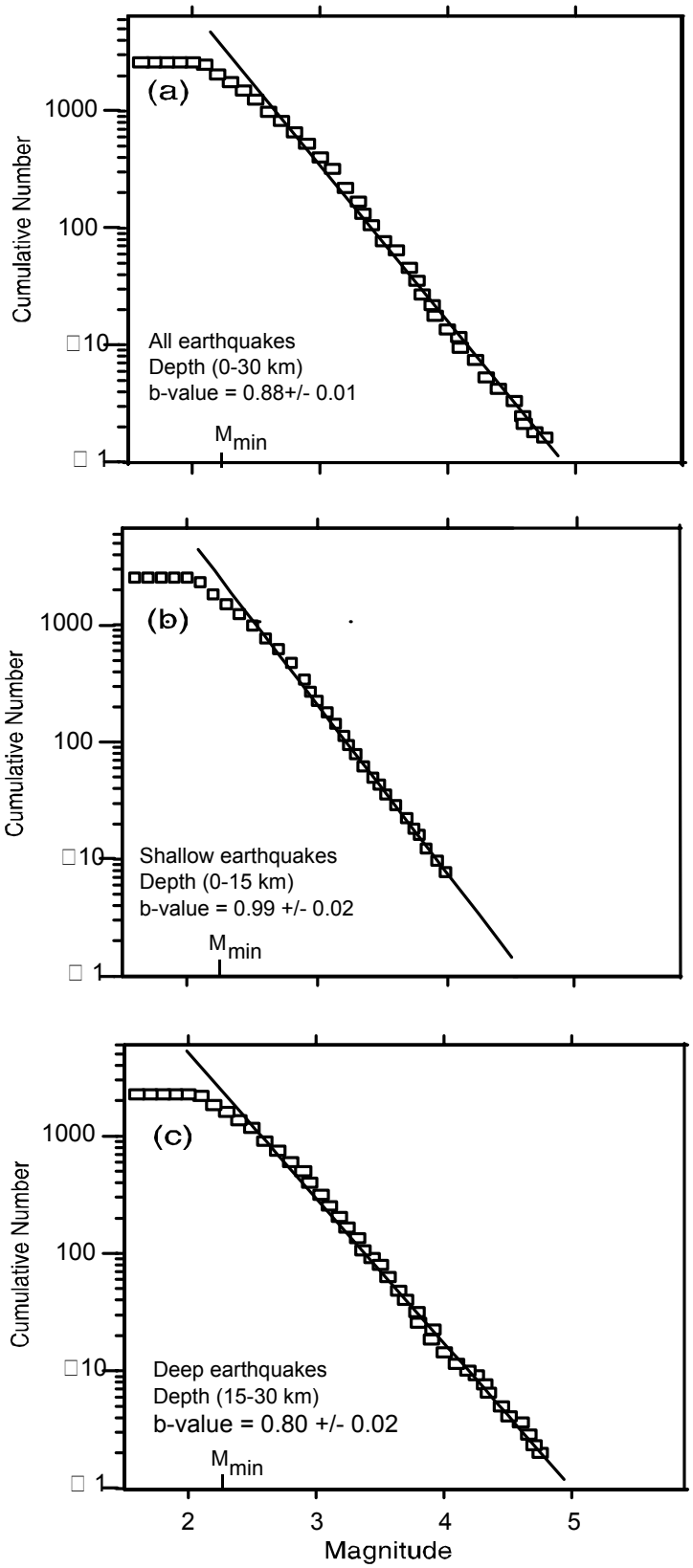

Figure 3.7. Frequency-magnitude distributions by depth for (a) all events, (b) shallow and (c) deep earthquakes. Plain lines show the maximum likelihood estimates of b-values.

Depth dependence of b-value could reflect the degree of material heterogeneity and stress conditions (Mori and Abercrombie 1997). The variation of b-value with depth is examined in the Aswan catalogue. There is a systematic decrease in b-value with increasing depth of earthquakes (Fig 3.8). We suggest that at shallow depth (0.1-15 km), conditions with more heterogeneous material properties and lower lithospheric stress prevail. The reverse prevails at greater depth (16-30 km).

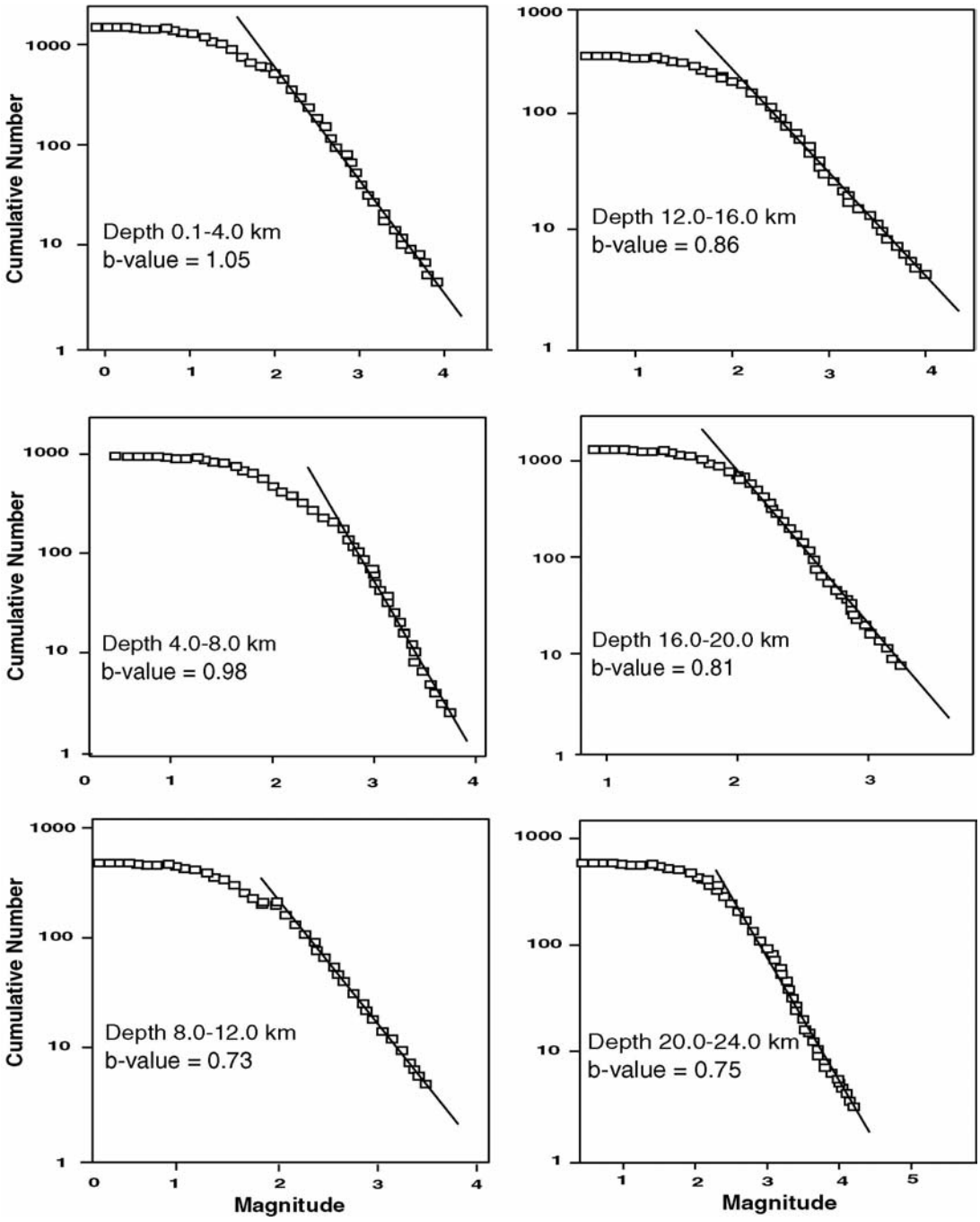

Figure 3.8. Frequency-magnitude distributions by depth for Aswan events 0.1-4, 4-8, 8-12, 12-16, 16-20 and 20-24 km respectively. Lines show the maximum likelihood estimates of b-values.

3.6 Water level and seismicity rate in the Lake Aswan area

The lake water level is measured twice daily. Complete list of daily water level and earthquakes can be found in CD. Table 4 shows the average water level and number of earthquakes from 1981-2001. Poro-elastic and diffusivity properties of the aquifer were estimated from observed water level fluctuation in wells. The analysis of twenty-three years of data from three wells (drilled prior the filling of the lake) has been used to find storage coefficients, permeability and stiffness of the Nubian formation (Evans et al. 1991a, b; Beavan et al. 1991).

Several studies have shown similarities between the temporal distribution of seismicity and reservoir level following the construction of the High Dam (Simpson et al. 1990; Kebeasy and Gharib 1991, Awad 1995a). They concluded that increase in seismic activity was linked to the water level variation. When the water recovered away from cluster K1 (Fig 3.4), seismicity decreased.

Table 4. Annual earthquake number and average water level

Year	Total number	Max. magnit.	Max. depth	Max water level	Average magnit.	Average depth/Y	Average water level/Y
1981	86 (Dec.)	5.4	30.0	176.5	2.56	17.0	175.5
1982	1380	5.3	29.5	175.0	2.41	17.73	175.0
1983	386	4.5	29.3	172.3	2.34	14.35	172.3
1984	373	4.5	25.7	170.0	2.32	12.24	165.0
1985	75	3.4	25.3	164.0	2.29	9.85	162.0
1986	79	3.4	26.6	163.8	2.15	10.14	160.0
1987	338	4.5	26.5	161.7	2.21	11.52	159.0
1988	149	3.7	29.0	169.3	2.10	9.93	157.0
1989	106	4.1	29.8	170.0	2.32	13.29	166.0
1990	197	4.1	29.9	170.4	2.03	9.75	168.0
1991	132	3.5	27.5	171.0	2.08	10.63	168.0
1992	147	3.5	29.3	172.0	1.93	10.70	169.0
1993	141	3.1	22.9	174.0	1.78	8.66	172.0
1994	109	3.8	29.0	177.0	2.0	5.50	173.0
1995	153	3.5	24.1	177.5	1.95	6.72	175.0
1996	113	3.3	23.2	178.5	1.94	5.57	176.0
1997	59	3.5	28.65	179.0	1.89	7.14	177.0
1998	92	3.9	21.0	180.0	2.11	6.53	1.77.0
1999	146	4.0	20.56	181.5	1.9	5.57	178.5
2000	147	4.0	20.0	182.0	2.1	3.64	179.0
2001	141	3.7	25.34	182.5	1.85	3.89	179.0

Figure 3.9 shows water level and seismicity average in ten days intervals during 1982-2001. The water level varies daily and is also characterised by an annual cycle with high in November-December and low in July-August. Monthly distribution of Aswan seismicity and water level in the lake is shown in Fig. 3.10.

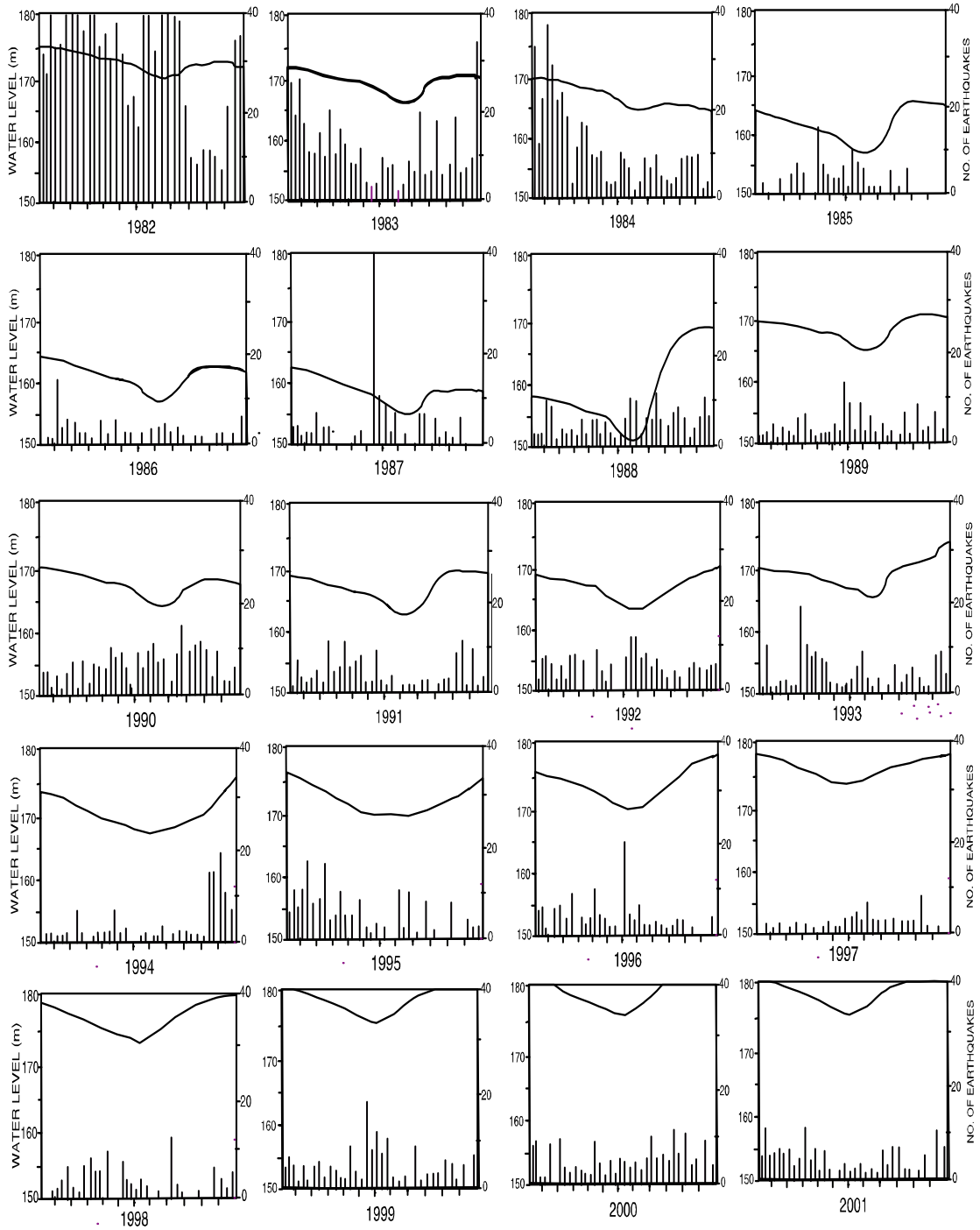

Figure 3.9. Water level change (m) and earthquake number in Lake Aswan (1982-2001).

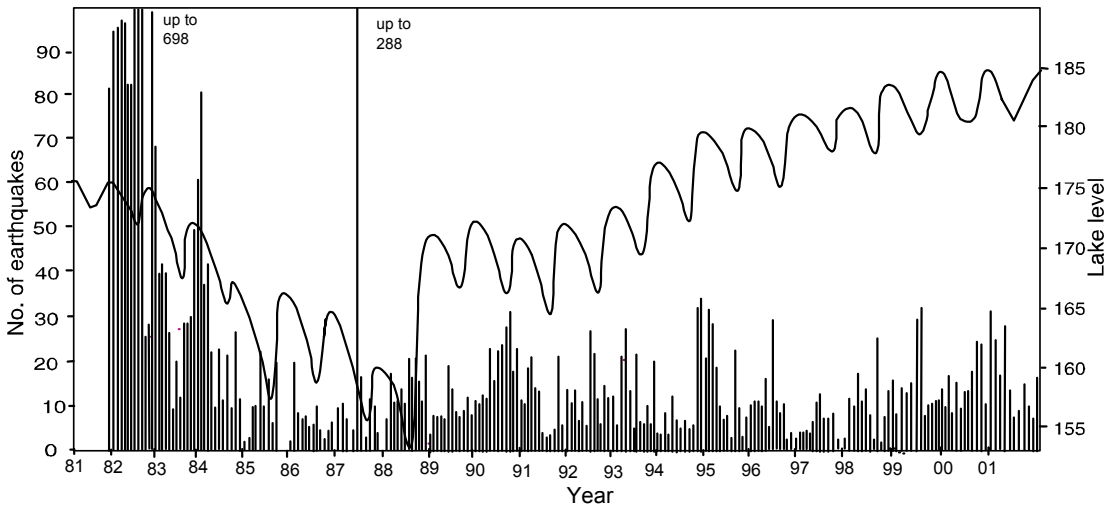

Figure 3.10. Comparison between earthquake activity and water level (m) in the period 1982-2001.

When comparing water level and seismicity between 1982 and 2001 (Fig. 3.9 and 3.10), correlation between level fluctuations and seismicity is difficult to assess. As an example, the gradual decrease of the seismicity rate in the period 1982-1988 could be correlated to the simultaneous decrease of water level. However, such a decrease of seismicity over time after an M = 5.4 event is the generic aftershock sequence for most natural earthquakes (Omori 1894). Analysis of seismicity rate in the period 1982-1990 by Mahmoud et al. (1998) confirms the exponent value of the Omori law close to unity, i.e. a standard value for tectonic earthquakes (Utsu 1995). Accordingly, the observed decrease of seismicity rate in the period 1982-1988 below Lake Aswan can be expected as from a natural seismicity pattern, without any requirement for water level decrease.

In order to characterise the link between water level and seismicity rate, we study the annual correlation between water level variations and seismicity. The correlation is carried out for all events, shallow events and deeper earthquakes (Fig. 3.11a-c), and for magnitudes greater than 2.0. The Aswan seismicity separates into shallow and deep seismic zones (Figure 3.4). Shallow events have focal depths between 0.1 and 15 km. Deep events extend from 15 to 30 km.

On Figure 3.11 we observe a phase shift between the two time series, i.e. a time delay between water level, the hypothesised cause, and earthquakes. The time delays are 2 and 4 months for shallow and deep seismicity respectively. This was confirmed by continuous monitoring of the groundwater level in the area using several piezometers (Evans et al. 1991a, b). It was mentioned that the speed of water through Nubian formations of high porosity is about 0.6 km/day. But the velocity of water propagation should increase in the fractured basement as discussed above, taking only two months for triggering shallow earthquakes.

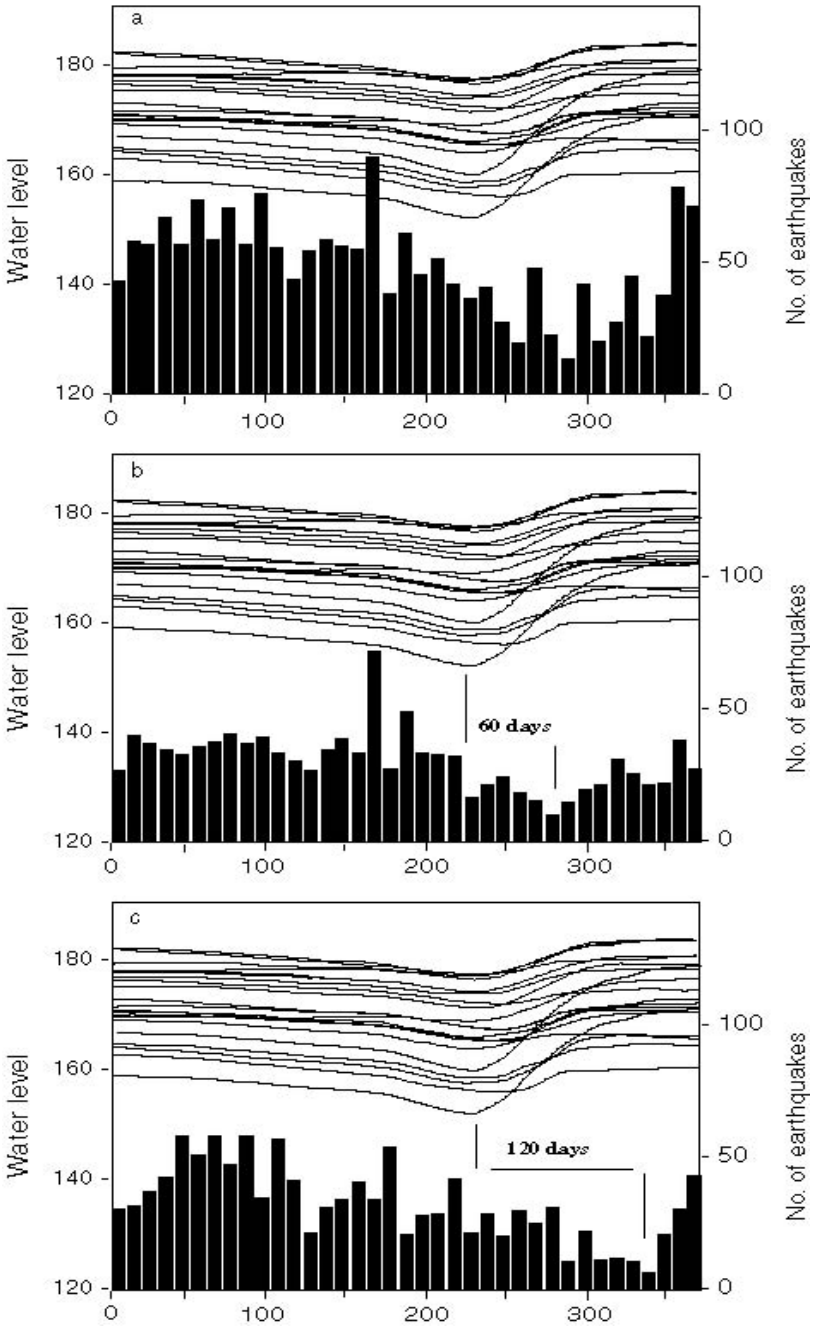

Figure 3.11. Correlation between seismicity (histogram) and water level (lines) during 20 years for (a) all event, (b) shallow and (c) deep earthquakes.

To better emphasise possible correlation, we transformed time series of water fluctuations and earthquake data into frequency domain by using Fast Fourier Transform (FFT). Well-resolved peaks of water level and seismicity are shown at 1 year $^{-1}$, proving the correlation between the two variables (Fig. 3.12a-c). The strongest seismicity peak is obtained for the deepest events in the earliest period. This peak disappears for all events in the period 1989-2001 (Fig 3.13 a-f), indicating that the water pressure has no longer any triggering effect.

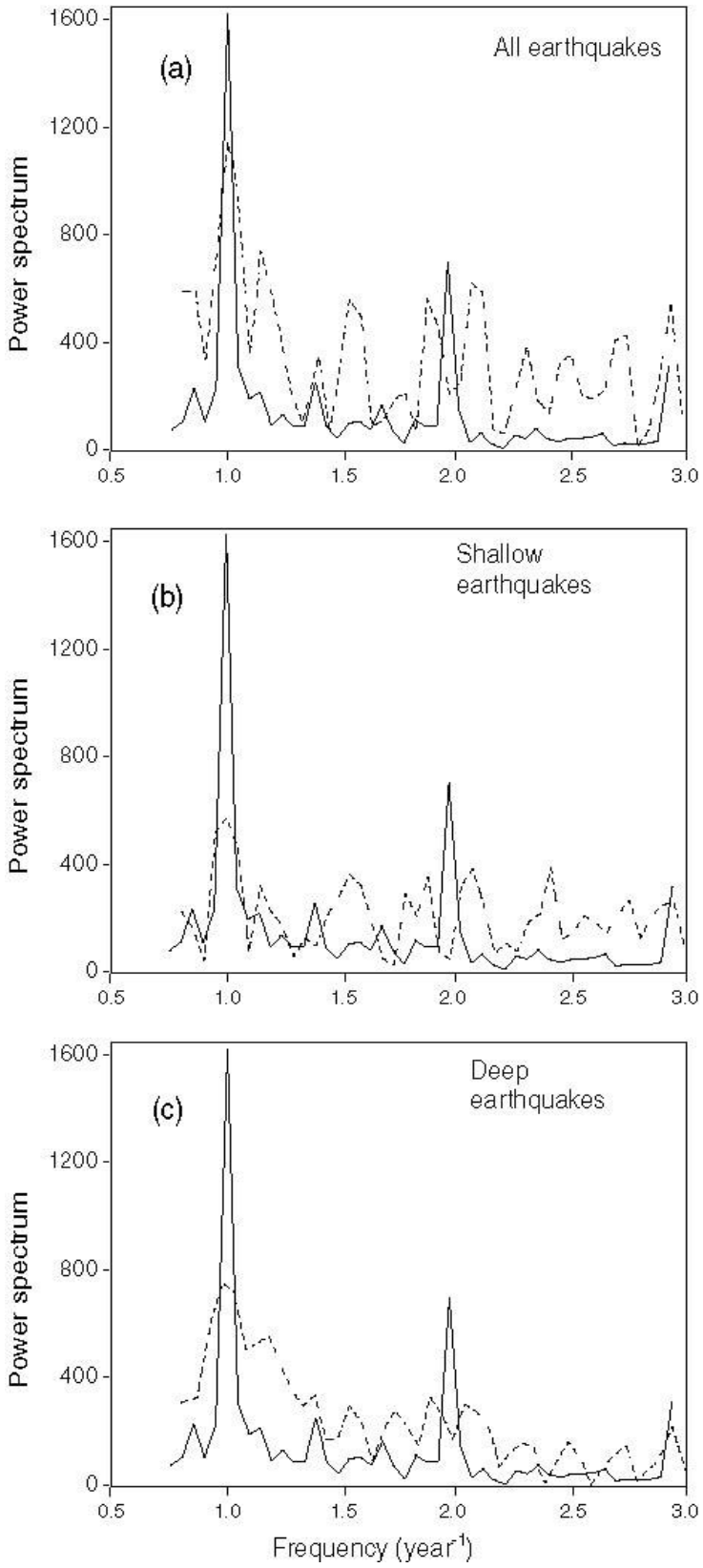

Figure 3.12. Amplitude Fourier spectra representing seasonal peaks of the water level and number of earthquakes during the period 1982-2001 for (a) all events, (b) shallow and (c) deep earthquakes.

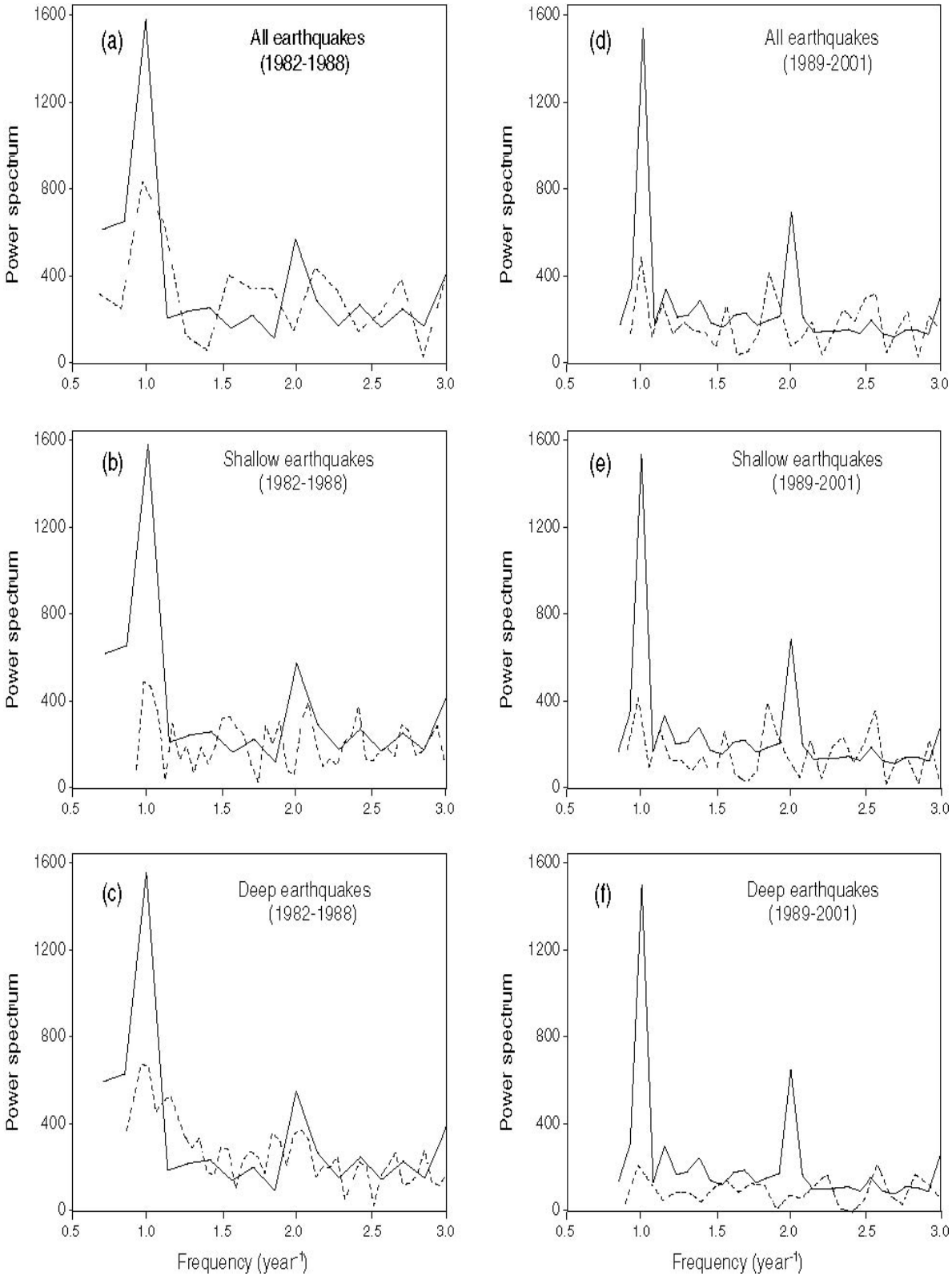

Figure 3.13. Amplitude Fourier spectra representing seasonal peaks of the water level and number of earthquakes during (a, b, c) the periods 1982-1988 and (d, e, f) 1989-2001 for all events, shallow and deep earthquakes.

3.7 Evolution of the seismicity patterns during the period 1982-2001

To analyse spatial and energy patterns of the seismicity as a function of time, we chose magnitudes greater than 2, to avoid biases possibly induced by catalogue completeness. Fig. 3.14 shows the distribution of earthquake epicenters (longitude and latitude) with time. Solid lines are the mean values of longitude and latitude. To evaluate the seismicity patterns, we used statistical techniques, such as average spatial behaviour, fractal spatial clustering and b-value change over time.

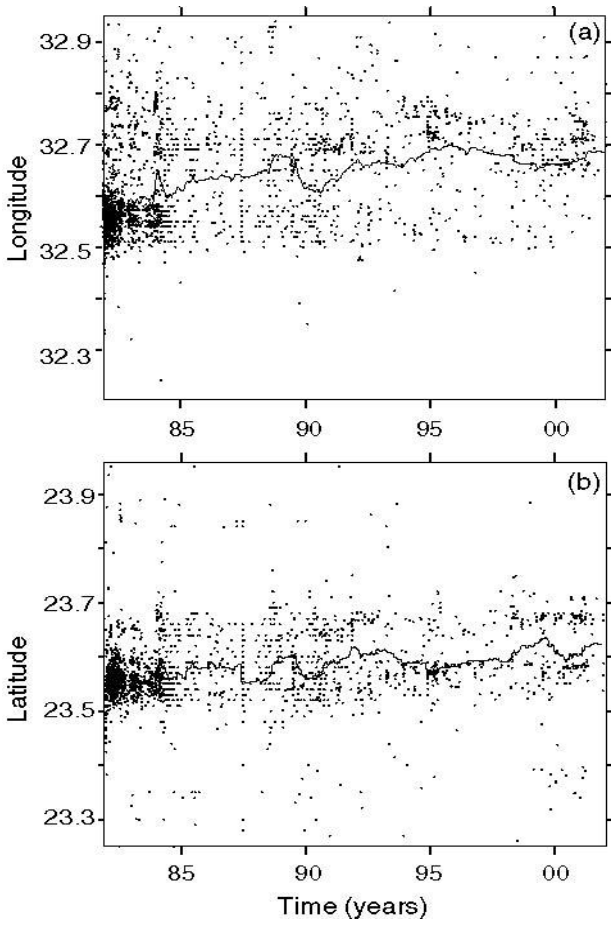

Figure 3.14. Geographical distribution of earthquakes with time during the period 1982-2001 (a) with longitude (b) with latitude.

The major trend of hypocenter locations over time is the change of average depth (Figure 3.15). A robust decrease in average depths is resolved for the whole dataset during the period 1982-2001, with a slower decrease rate in the period 1986-1994. In this latter period, the average depth for deep events increases at the same rate the shallow event depth increases. Between 1982 and 1986 the average depth decreased strongly for the shallow events. Since 1986 they are merging the surface at slower rate. Since this year, average depth for deep events did not change significantly.

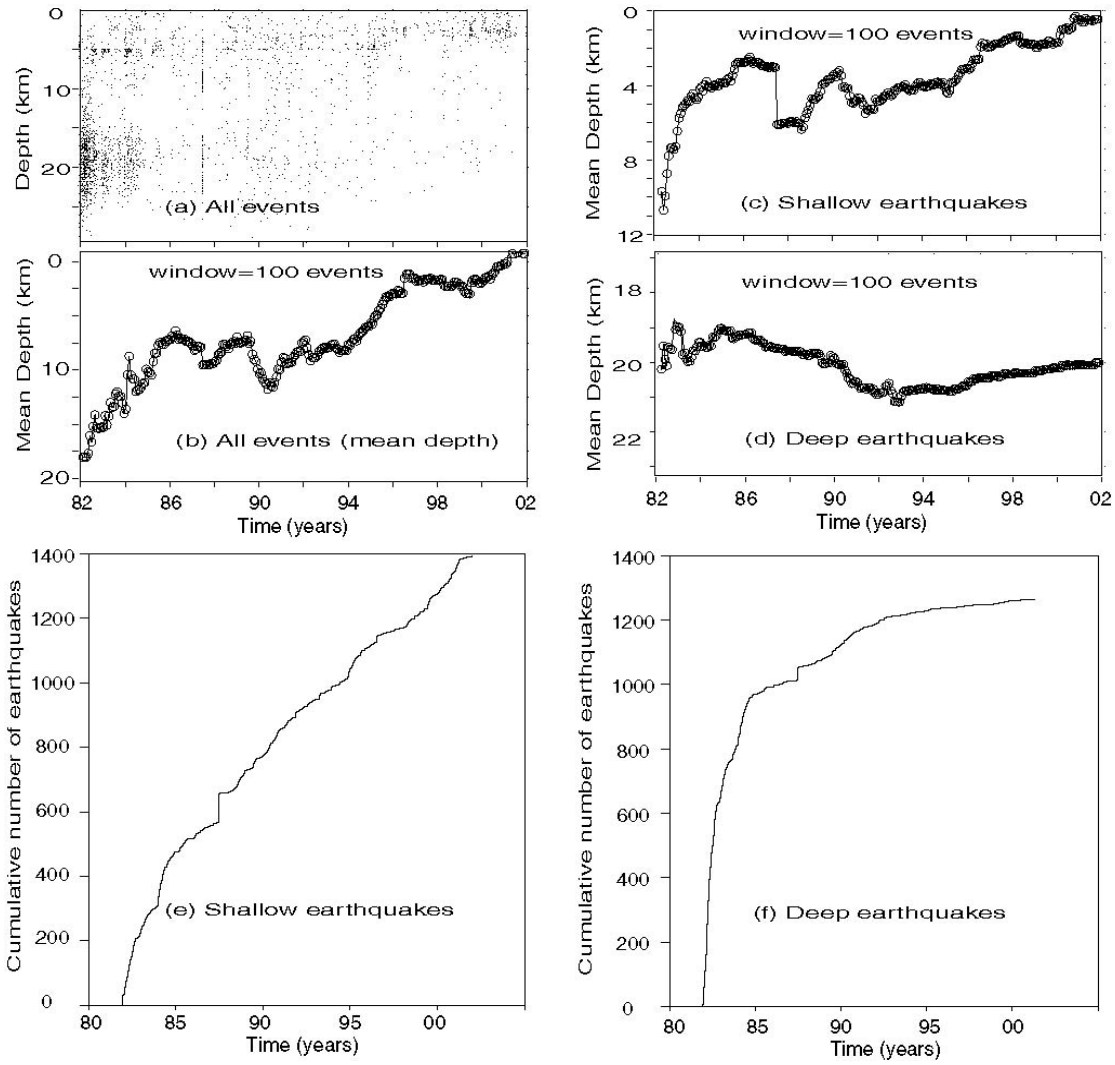

Figure 3.15. (a) Time-depth distribution of earthquakes for all events. Time variation of the mean depth of earthquakes for (b) all events, (c) shallow and (d) deep earthquakes. Cumulative number of (e) shallow and (f) deep earthquakes.

The nearly linear ascending curve of figure 3.15e attests for a roughly constant seismicity rate of shallow events. This is not the case for the deep events for which the seismicity rate dropped drastically after 1988 (Fig 3.15f).

To analyse the evolution in spatial clustering we used the correlation integral method (Grassberger and Procaccia 1983). The correlation dimension D is obtained from

$$D = \lim_{(r \to 0)} \log C(r) / \log(r) \tag{40}$$

$$C(r) = 2N_{R<r} / N(N-1) \tag{41}$$

where C(r) is the correlation function, r is the distance between two epicenters / hypocenters and N is the number of event pairs separated by a distance R< r.

We estimate the correlation dimension by fitting a straight line to a plot of log C(r) vs. log(r). The minimum and maximum values of r are chosen by taking into account the error in epicenters and the finite size of the studied zone. The maximum value of D for the epicentre distribution is 3, corresponding to a uniform distribution of earthquakes in 3D space. Smaller values of D suggest a tendency toward clustering. In a 2D space, D is equal to 2 for a uniform distribution. Decrease of D-values indicates an increase of clustering. In Table 5 we estimate D-value for all events, shallow and deep earthquakes in 2D and 3D respectively (Fig. 3.16a-f).

Table 5. D-values for two and three dimensions

	D2	D3
All events	1.45	1.92
Shallow events	1.36	1.76
Deep events	1.55	2.14

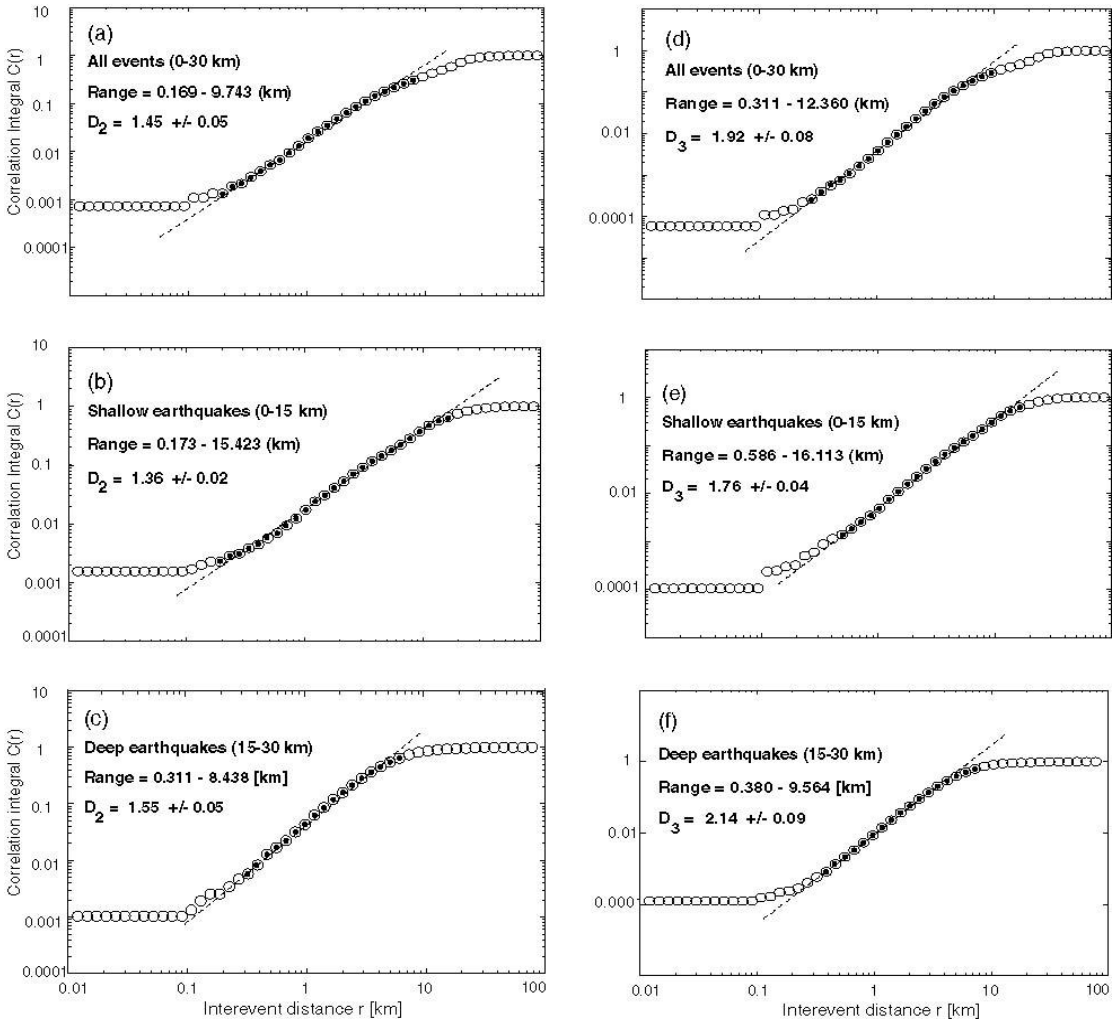

Figure 3.16. 2D (left side) and 3D (right side) estimation of the correlation dimension D of the epicentre distribution of selected earthquakes by fitting a straight line to a plot of log C(r) against log r for all events (upper), shallow (middle) and deep earthquakes (lower).

Table 5 indicates that the earthquake clustering is strong, because the earthquakes are bounded on a roughly planar structure in 3D space. The change of D-value with time for all events, shallow and deep earthquakes is shown in Figs. 3.17 - 3.19. Large fluctuations in D values prevent extracting a robust pattern on the whole period. In the period 1990-2000 a decrease in D values shows up for the whole seismicity, whereas an increase of D value occurs for deep events in the 1980-1990 period.

In the energy domain and in the range $2.0 \leq M < 4.8$, the Gutenberg-Richter distribution is recovered for the Aswan seismicity. The b-values, obtained for all events, and for the shallow and deep earthquakes are respectively 0.88, 0.99 and 0.80 (Fig. 6a-c). The time evolution of b-value for shallow and deep events is different as well. The b-value for deep events decreases up to 1985, whereas the b-value of shallow events increases in the same time period and is still continuing to increase up to 1998 (Figure 3.17 - 3.19).

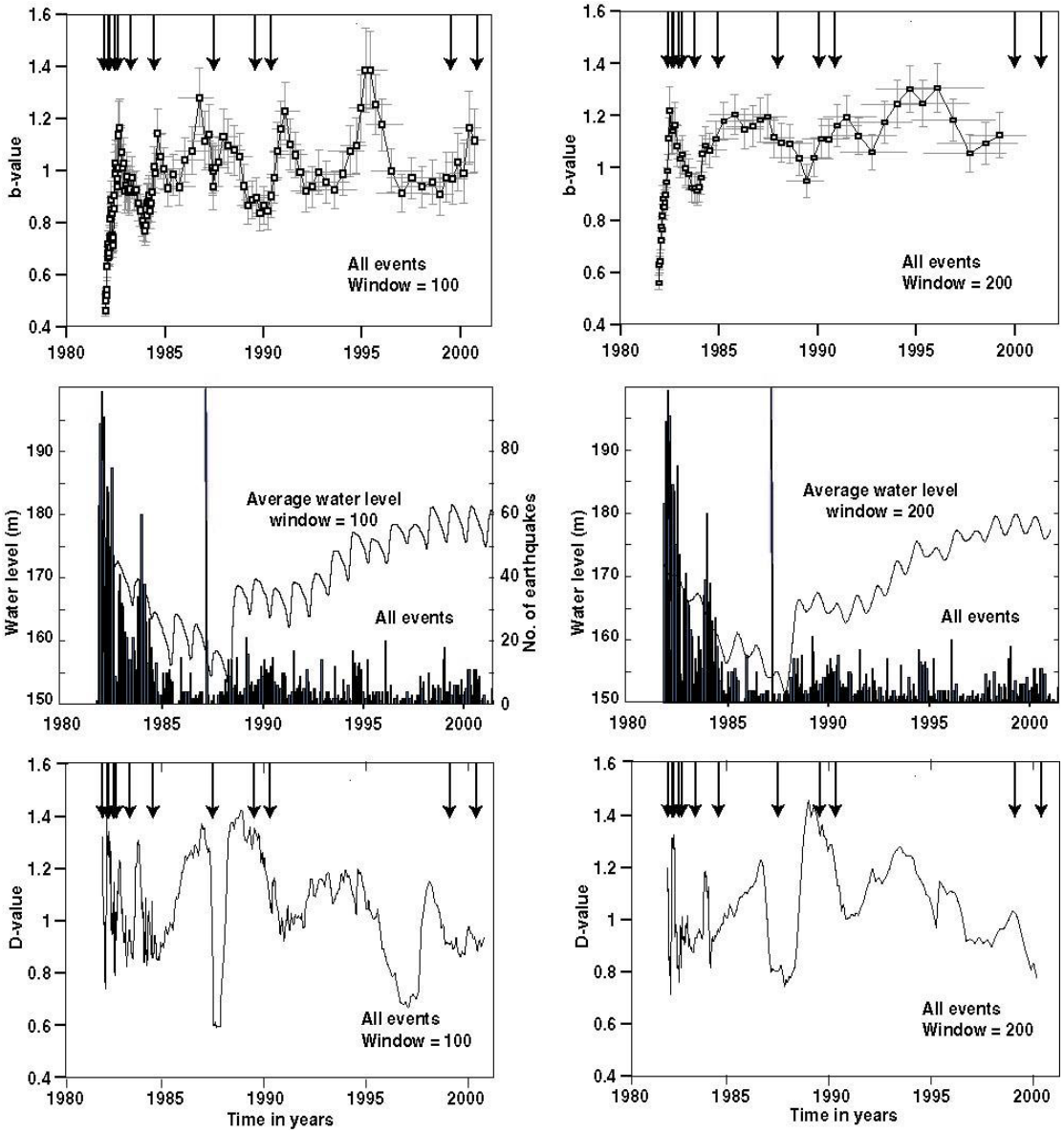

Figure 3.17. 2D fixed window temporal variation of the fractal dimension D and b-value for all events. Comparison with average water level and earthquake activity. Arrows indicate events with M >= 4.

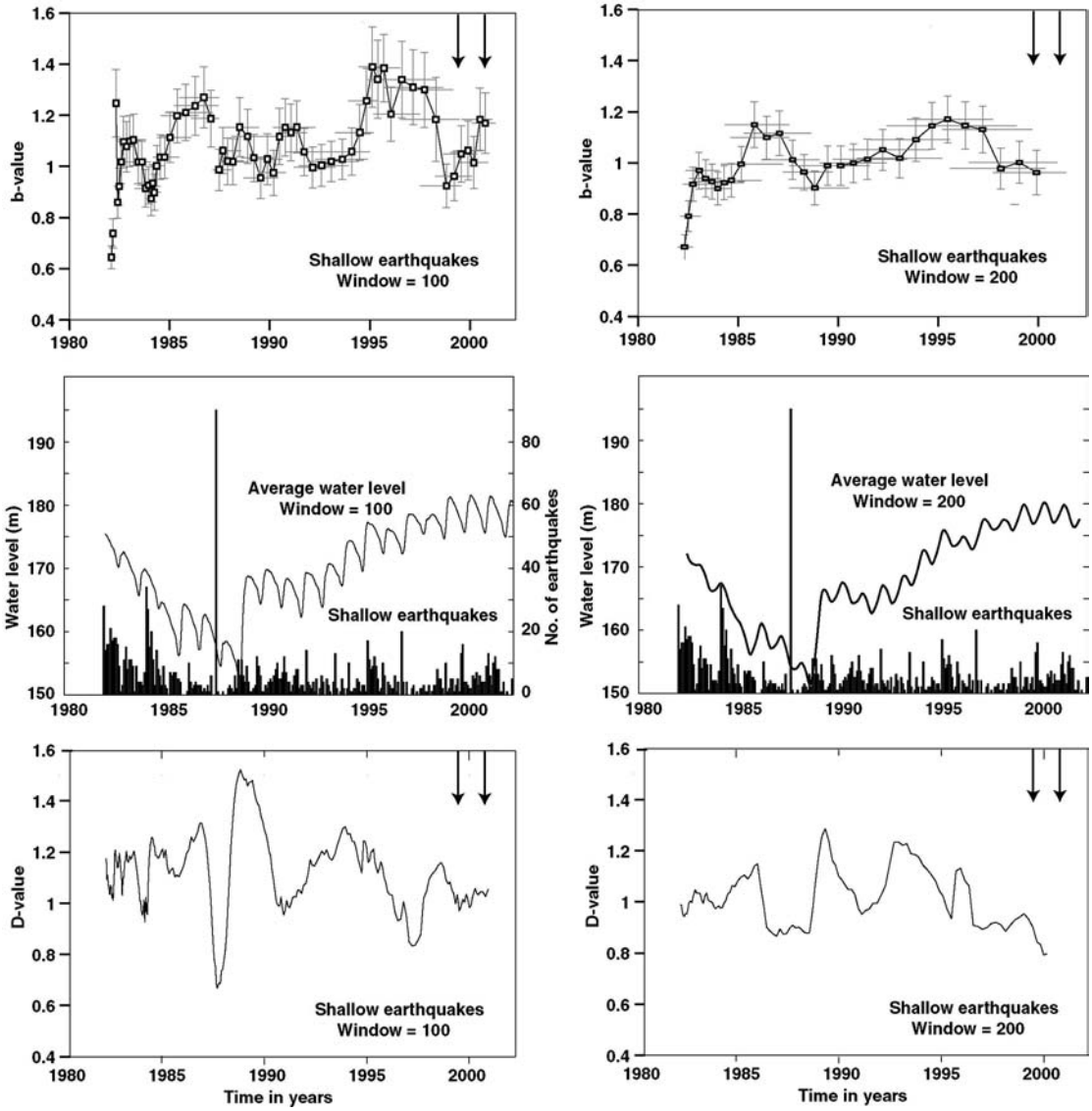

Figure 3.18. 2D fixed window temporal variation of the fractal dimension and b-value for shallow earthquakes. Comparison with average water level and earthquake activity. Arrows indicate events with M >= 4.

3.8 Discussion

Because the Aswan seismicity source is located directly beneath the second largest man-made reservoir in the world, several authors suggested that this seismicity be induced by the reservoir impoundment (Kebeasy et al. 1982; Simpson 1988). In order to test the influence of water level change on the seismicity pattern we analyse the statistical property of Aswan seismicity in the period 1982-2001. We report two types of results. First the seismicity response over time is depth dependent. The Aswan seismicity has been previously proposed to be localized in two spatial swarms, respectively between shallow (<15 km) and great (>15 km) depth (Simpson et al. 1990). This pattern is still relevant for describing the seismicity pattern on the 1982-2001 period (Figures 3.4b-c, 3.11b-c and 3.15c-d). Secondly, when the seismicity rate is correlated to a water level change, the fluctuations of event distribution in space and energy appear not to be primarily driven by the lake level.

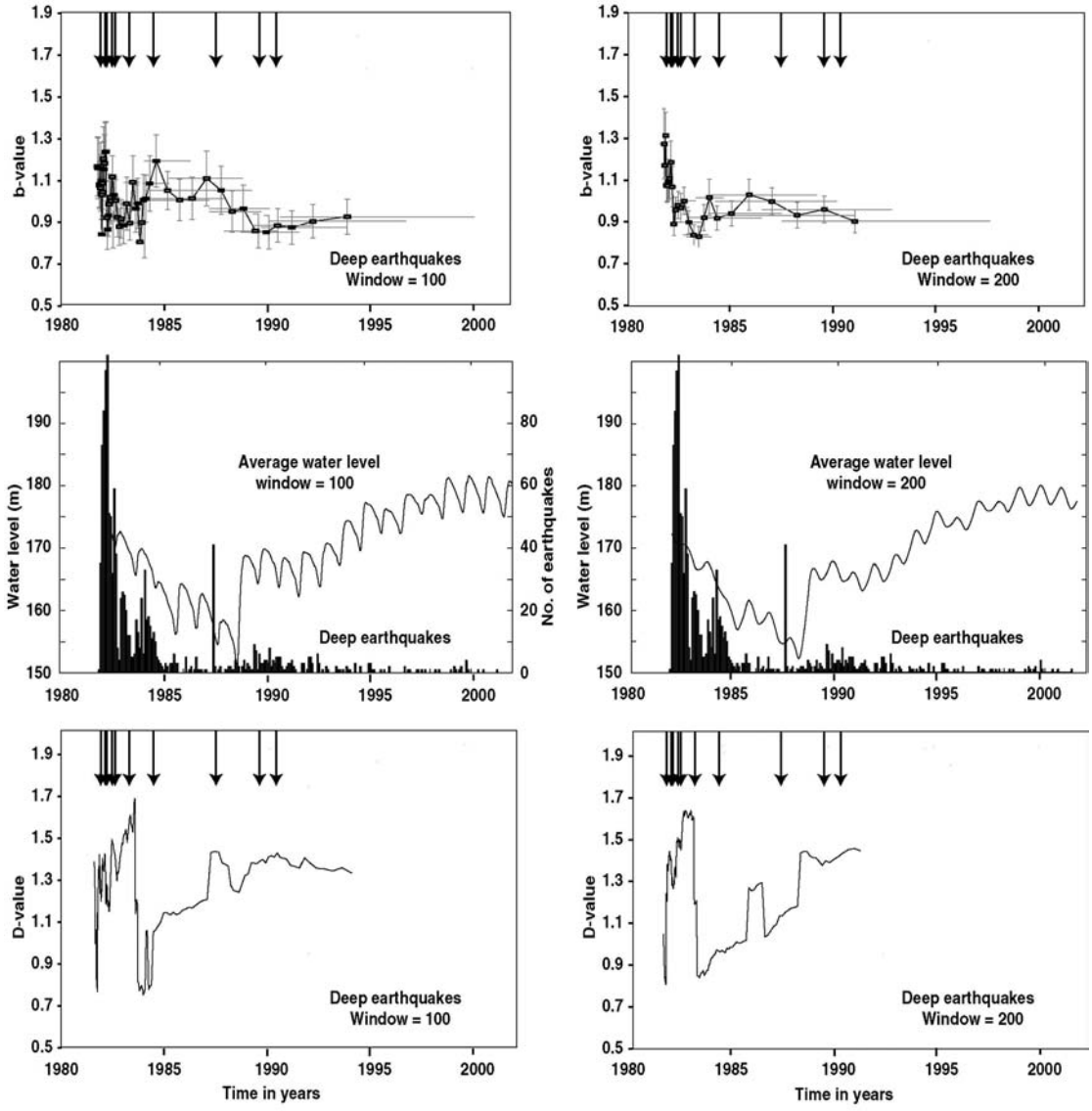

Figure 3.19. 2D fixed window temporal variation of the fractal dimension and b-value for deep earthquakes. Comparison with average water level and earthquake activity. Arrows indicate events with M >= 4.

We further analyse how such patterns can be unified in terms of the influence on the seismicity of the external loading of the system, i.e. water level change. We do not address the question as to whether or not the M = 5.4 1981 event, which is at the onset of our catalogue, was induced by the reservoir impoundment.

The depth evolution over time argues for the seismicity of Aswan to be due to a transient dynamics, not yet in equilibrium after 20 years of seismicity. The strong epicentre localisation on the northern part of the lake, with its small (if any) horizontal migration over 20 years, attests for just one specific patch of the Kalabsha fault to have been close to failure in the area around Lake Aswan before the reservoir impoundment.

If a global upward migration of seismicity exists, when sorting shallow and deep seismicity the pattern is reversed. The average depth of deep hypocenters is stable or slightly increases over time, whereas for shallow events it decreases. Both patterns can be reminiscent of aftershock diffusion patterns proposed after a tectonic main shock (Mogi 1968; Imoto 1981; Tajima and Kanamori 1985a, b; Helmstetter and Sornette 2003b). The weak depth increase of the deep events is possibly bounded by the brittle-ductile transition at these depths. The spatial clustering as estimated through the correlation dimension, also argues for different patterns between shallow and deep events. D-value remains constant with large fluctuations for shallow events and increases for the deep events in the period 1983-1990. The large D-value fluctuations are possibly induced by recurrent aftershock sequences after $M > 4$ events, as suggested on Figs. 3.17-3.19. Accordingly, the first-order changes in seismicity location, i.e. deep migration and D-value variation, do not appear to be driven by water level changes on the studied period.

In the energy domain again, shallow and deep earthquakes behave differently. The deep events show larger b-values than the shallow events. A relative decrease of b-value is observed at the beginning of our catalogue for deep events, whereas it is an increase during the same period for the shallow events. Although many processes could be involved in producing b-value changes, low b-values with increasing depth appear to result form the generic transition from brittle to ductile behaviour. This was proposed by model and laboratory experiments (Amitrano et al. 1999; Sue et al. 2002; Amitrano 2003) and reported for genuine earthquakes (Mori and Abercombie 1997; Gerstenberger et al. 2001). Again it is difficult to extract the influence, if any, of the water level changes on the b-values that appears just driven by seismicity depth.

The seismicity rate is the only seismicity index that correlates with the water level loading, e.g. the annual peak (Fig. 3.12a). This correlation appears strong during the whole period when using all the events. It is suggested that the main effect is caused by the deep events in the 1982-1988 period (Fig. 3.13c). During this period the global Aswan seismicity follows the Omori law decrease over time with an exponent close to unity (Mahmoud et al. 1998). This argues for the Aswan seismicity rate to not be solely driven by the water level. The seismicity fluctuations in space or energy as described by the b- and D-values are not simply related to water level changes. They appear as genuine fluctuations, typical of natural earthquakes. The b-value varies with depth and the D-value changes are induced by aftershock sequences. These results are different from another induced seismicity case study where pore pressure drop in a gas field has been observed as correlated with b- and D-value changes (Lahaie and Grasso 1999).

We propose that the dynamics of earthquake interaction, as measured by numerous genuine aftershock sequences in the Aswan catalogue (Figs. 3.17-3.19) reproduces most of the observed fluctuation of the Aswan seismicity catalogue. This can be expected from the generic cascade model of earthquake interaction (e.g. Kagan and Knopoff 1981; Ogata 1998; Helmstetter 2002, Helmstetter and Sornette 2003a). The main input of energy in the system was the $M = 5.4$ earthquake of November 1981, which

triggered a genuine aftershock sequence. This sequence developed at least up to 1990, as estimated by a p-value of the Omori law close to unity (Mahmoud et al. 1998). The deep seismicity vanished as time increased since it was not sustained enough by the water level change. Cascade models of seismicity predict a vanishing seismicity rate on finite time, if no external loading is added to the system (e.g. Helmstetter and Sornette 2003a). Shallow seismicity, still active until 2001, appears to be sustained by more efficient water loading at shallow than deeper depth. More earthquakes are triggered at shallow depth, as driven by water level change, inducing more aftershocks and increasing the seismicity rate. For shallow earthquakes in the period 1990-2001, we propose that the weak correlation with seasonal water level emerges from an acoustic noise induced by the cascade of earthquake sequences. These sequences have their own dynamics that is driven by the generic control parameter of seismicity, i.e., primarily the exponent of the Gutenberg-Richter and the Omori laws. When the water level change contributes to part of the triggering processes, most of the seismicity is induced by earthquake interactions.

Our observations and phenomenological model suggest that most of the Aswan seismicity is not directly driven by water level changes. The main contribution to the seismicity rate appears to be earthquake interaction through aftershock sequences. However, the water level contribution to Aswan seismicity may not negligible at all. This effect cannot exist without seasonal changes in water circulation within the fault network or at least, pore-pressure variations, leading in both cases to enhancement of the electrical conductivity. The MT method is employed for measuring this enhanced conductivity across the major fault (Kalabsha fault).

A next step of this work could be to test this cascade model for earthquakes on the Aswan catalogue as a null hypothesis (e.g. Helmstetter et al. 2003) in order to quantitatively estimate the variability of the seismicity pattern as driven by earthquake interaction solely.

4. Magnetotelluric investigations in the Kalabsha area

MT profile across the major Kalabsha fault is thought to deliver a detailed view of the electrical conductivity distribution of the area. We want to study how closely a model of this parameter would correlate with the well-known distribution of earthquake foci, and to detect any resistivity anomaly associated to the seismic activity of the fault network.

4.1 Practical aspects of data acquisition

The acquisition of MT data in the Kalabsha area took place during two weeks in September/October 2001. Fieldwork was carried out during the low water season in Wadi Kalabsha in order to increase the profile coverage in an otherwise flooded area. Two MT stations recorded continuous data during two days. Every day, one station was dismantled and re-installed at a neighbouring site. The Group of Geomagnetism of our university developed the instruments used in this study. With regard to the general practical aspects of data acquisition, including the problems of finding convenient sites for the measurements and the cultural noise handling, we refer to Schnegg (1998). A good MT site must be protected against weather effects like wind and direct heat from the sun. Also, it must be set up at least 200 m away off the road, since trucks would generate noticeable variations of the magnetic field at shorter distances.

We used two different sets of magnetic induction coils (Andrieux et al. 1974). Magnetic field variations of short period (audio magnetotellurics, AMT) were measured with ECA CM16 coils, whereas long periods (MT) used CM11E coils. The instruments make it possible to switch between the overlapping (AMT) and (MT) modes. Pairs of non-polarisable Ag-AgCl electrodes designed for ocean studies (Filloux 1987) measured the electrical field variations. They were slightly modified for use in fieldwork on dry ground. The telluric lines were oriented in the direction of magnetic north and in the corresponding perpendicular (E-W) direction (magnetic declination was smaller than 3°). The length of the telluric lines was 50 or 100 m, depending on the topography.

The MT data were collected at two sampling rates, using two sets of records with different magnetic induction coils but with the same electrodes. Block diagram of the MT data acquisition system and general set-up is shown in Fig. 4.1. MT measurements were carried out in the period band 0.0046-420 s at nine sites of an N-S profile crossing the Kalabsha fault. The length of the profile was 15.5 km. The AMT field was recorded in a period band 0.0046-0.3 s. The long period (MT) was installed for 48 hours, recording variation in the range 0.1-420 s. According to the corresponding available skin depth at 420 s, the MT allowed investigation of the conductivity distribution of the upper crust. Most of recordings at nine sites were close to Lake Aswan (1-2 km). The data quality was generally satisfactory. Table 6 shows the listing of the MT sites (see also Fig. 4.2 for location across Kalabsha fault).

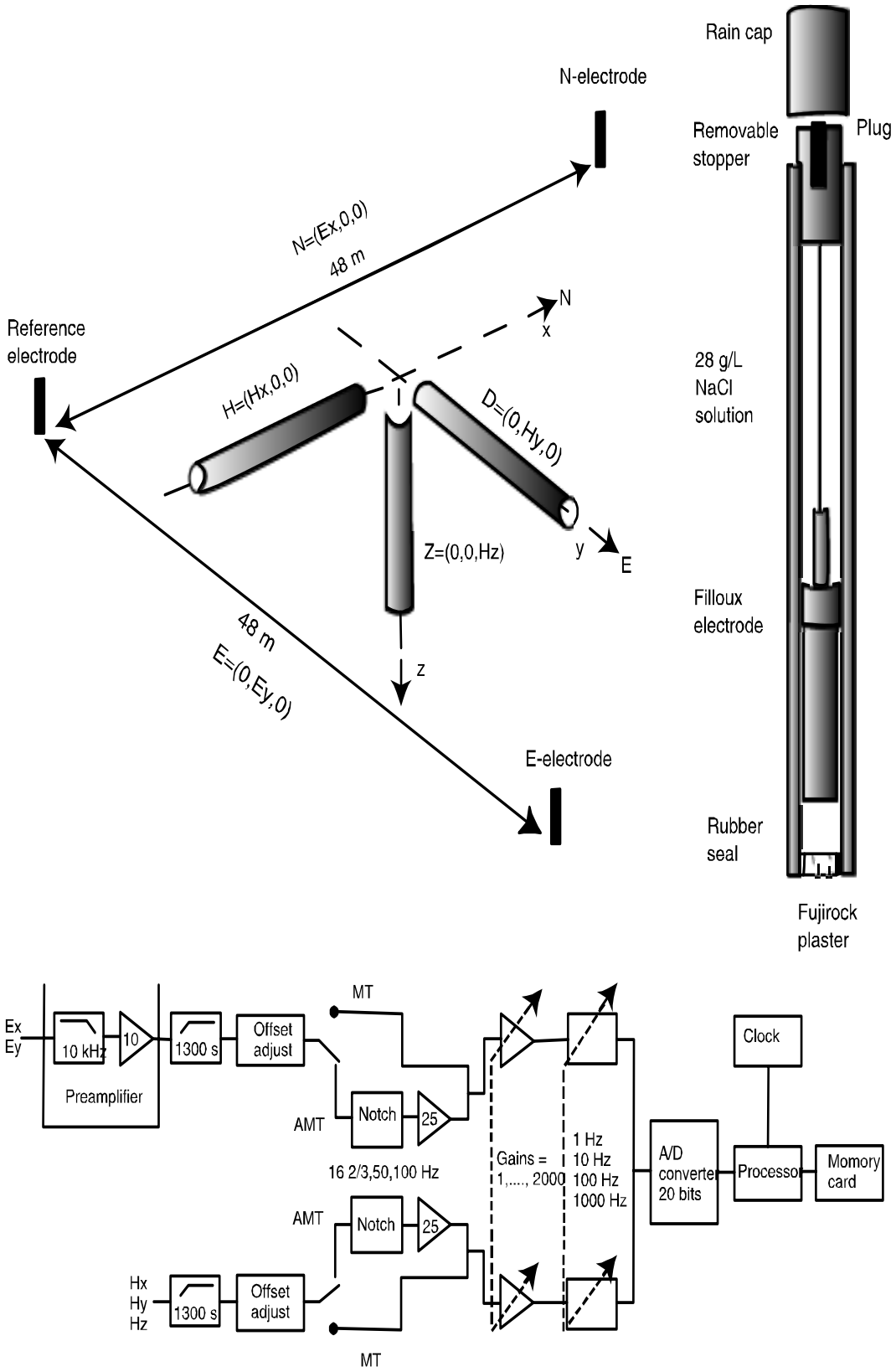

Figure 4.1. Upper left: MT set up showing three magnetic induction coils aligned toward north, east and downward. The telluric current is measured as potential difference between electrode pairs, using a single electrode as reference. Upper right: Non-polarisable Ag-AgCl telluric electrode with Plexiglas housing and porous tip. Overall length with weather cap is 32 cm. Lower: Block diagram of the MT data acquisition system (Schnegg 1998).

Table 6. MT sites listed in chronological order

Site name	Date	Latitude	Longitude	Remote reference
W02	29,30. 09.2001	23.53850	32.46714	-
W03	1,2.10.2001	23.54752	32.46757	W04
W04	2,3.10.2001	23.56637	32.46786	W03,W05
W05	3,6.10.2001	23.53160	32.46729	W04, W06,W07
W06	4,5.10.2001	23.58756	32.46160	W05
W07	6,7.10.2001	23.51150	32.46700	W05,W08
W08	7,8.10.2001	23.48750	32.46700	W07,W09
W08	8,9.10.2001	23.44764	32.46702	W08,W10
W10	9,10.10.2001	23.52191	32.46730	W09

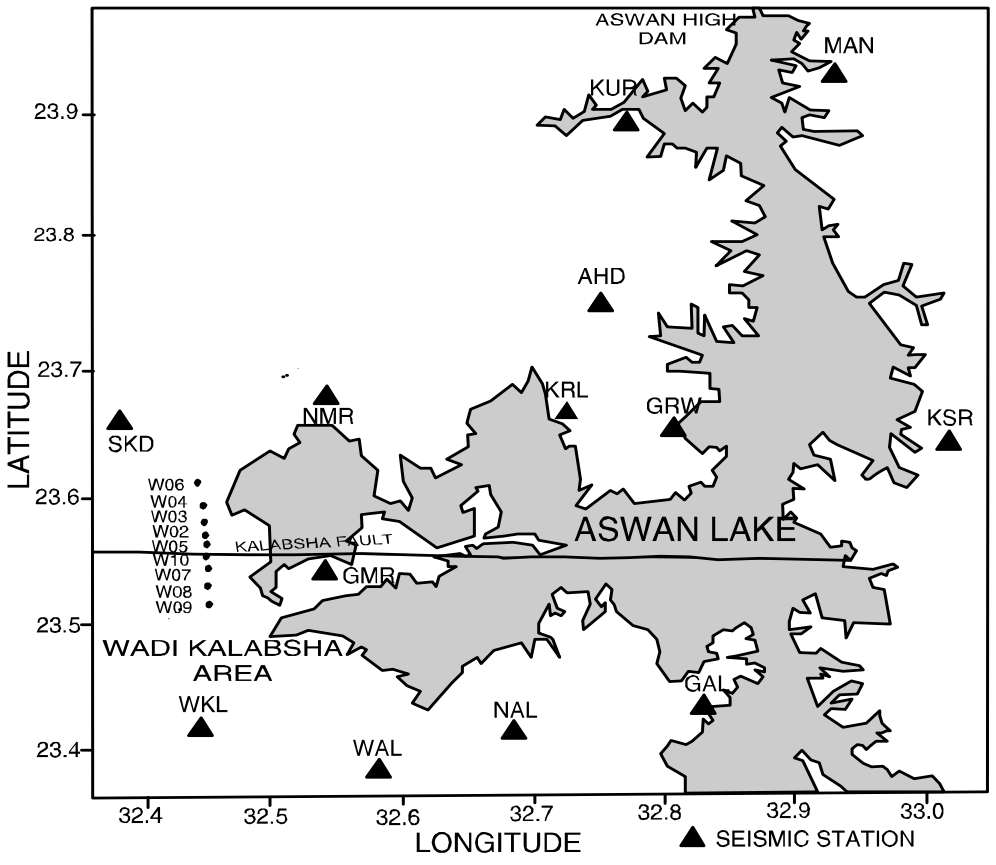

Figure 4.2. Location map of Wadi Kalabsha area and seismograph network around the epicentral area. MT profile crossing the Kalabsha fault.

4.2 Processing and analysing MT data

The MT data consisted of four components (Ex, Ey, Hx and Hy). Technical problems arose with the coils, due to excess temperature, static electricity caused by air dryness, and connector problems due to dust. These problems prevented us from measuring the vertical magnetic component, since we had to use the Hz coil as spare coil for the horizontal components.

The different data-processing steps leading to the final model of electrical conductivity distribution are described in Chapter 1.

4.2.1 MT transfer function of Kalabsha area

Plots of apparent resistivity and phase for Z_{xy} and Z_{yx} (TM and TE modes) impedance tensors are shown along with coherency and skew parameters in Fig. 4.3. The sites W02, W03 and W05 are near the Kalabsha fault (see figure 4.2).

The MT data quality seems good according to the coherency value. The coherency parameter is sensitive to noise. Some sites display similar sounding curves; they show splitting of the two components (Z_{xy} and Z_{yx}) for long periods and are identical in the short period range. For short periods, there is an increase in skew values, not exceeding 0.6, however. The skew for long periods (T > 1 s) and for all sites is below 0.2. Therefore the data should be treated at least as 2D, but 3D handling is not required (Fig. 4.3). An obvious increase of the apparent resistivity (5-500 Ωm) can be seen at periods 0.0046-10 s, with an accompanying phase drop. This reflects the presence of thin water-saturated sediments and fractured granitic layers in the Wadi Kalabsha area. For period up to 420 s the phase increases and the resistivity decreases.

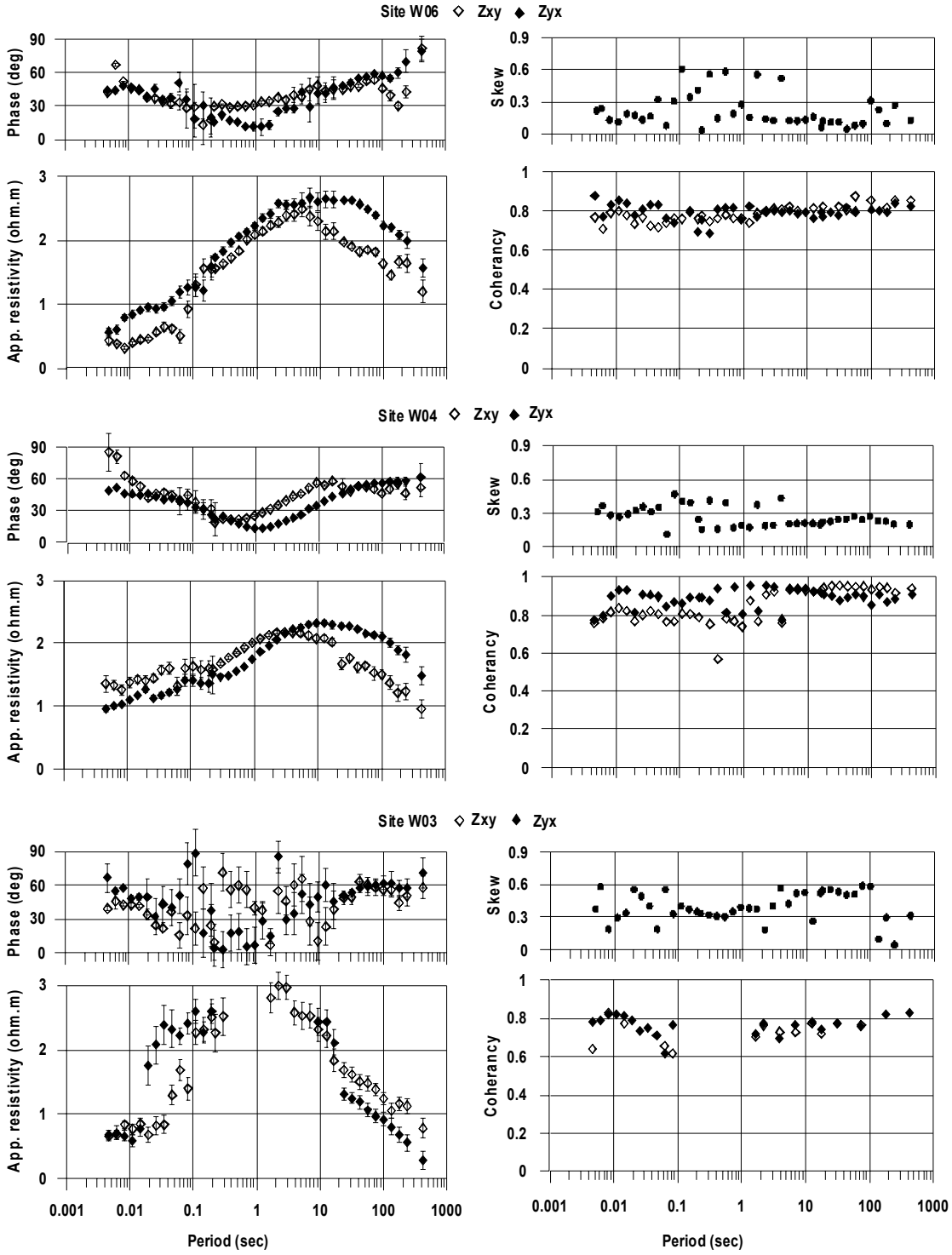

Figure 4.3. Apparent resistivity, phase for both TE and TM modes vs. period. Skewness and coherency functions.

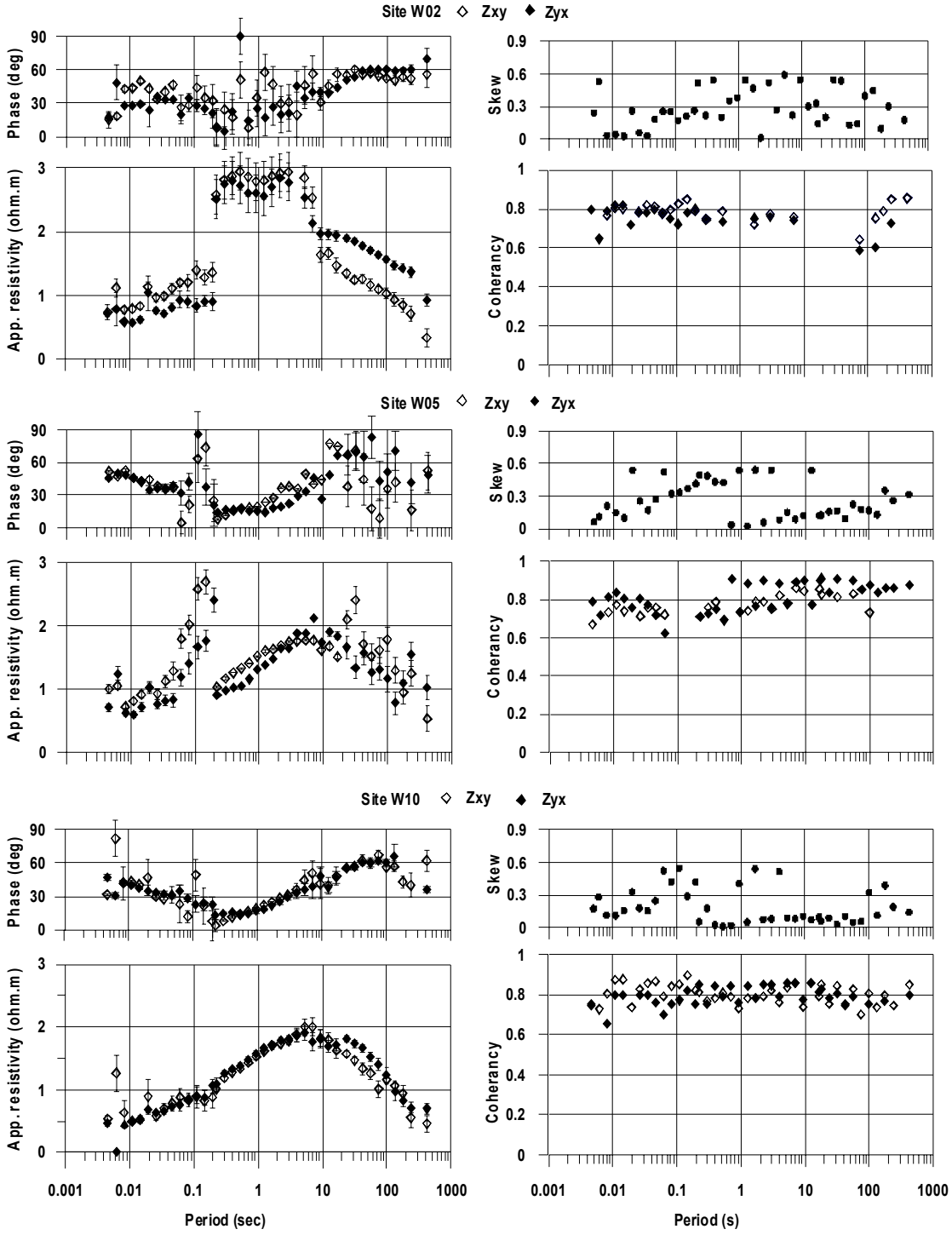

Figure 4.3. (Cont.) Apparent resistivity, phase for both TE and TM modes vs. period. Skewness and coherency functions.

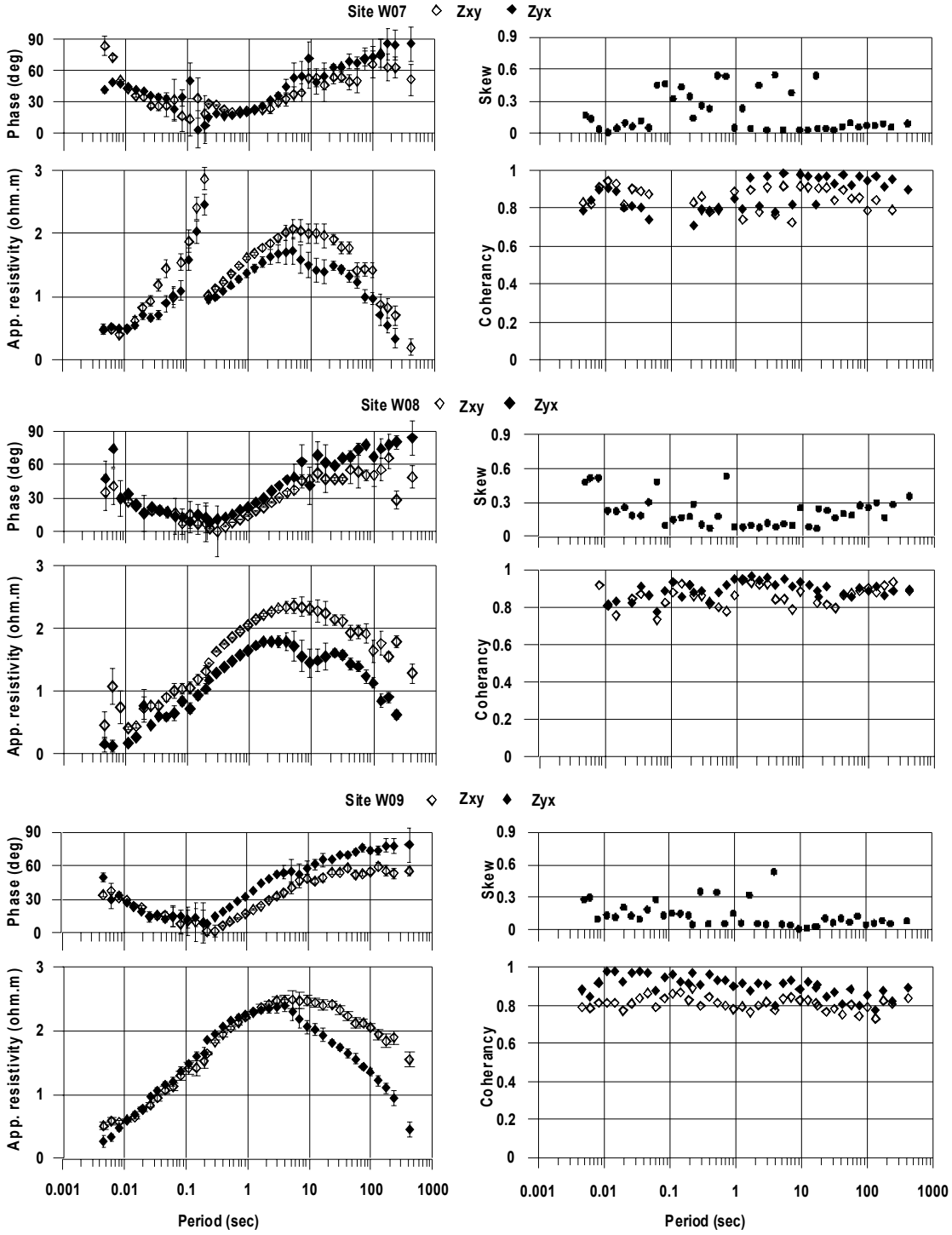

Figure 4.3. (Cont.) Apparent resistivity, phase for both TE and TM modes vs. period Skewness and coherency functions.

Before starting to model the resistivity structures the impedance tensors were investigated to account for distortion. To find a common rotation angle (common to all sites) we applied the Groom-Bailey (GB) decomposition scheme to the profile.

We show the results of distortion analysis in Figure 4.4. Strike angles are often variable even when the twist and shear angles are relatively invariant with frequency. For the long period range the GB decomposition at sites W07, W08 and W09 yield a regional strike close to N60°E. Twist and shear are generally small and around zero. Interestingly, the same result was obtained by fitting all earthquake epicenters with a completely independent method in Chapter 3 (Fig 3.6). After rotating the impedance tensors of all periods and all sites into this coordinate frame, 2D modelling was carried out to look for the best 2D model of the geology able to explain the field data.

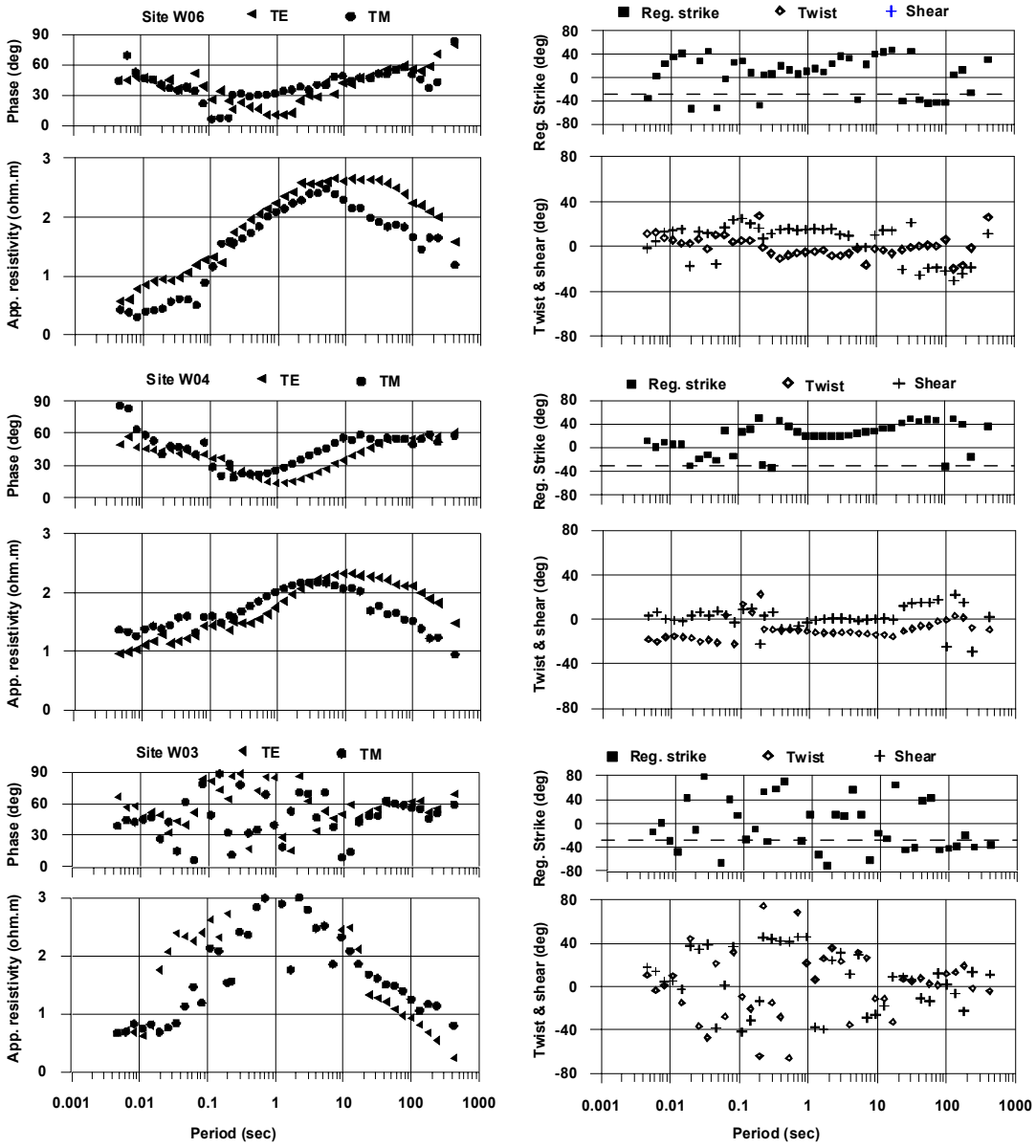

Figure 4.4. Results of the frequency-independent GB decomposition. (Left): Apparent Resistivity and phase curves predicated by the GB decomposition. (Right): Regional strike, Twist and shear angles.

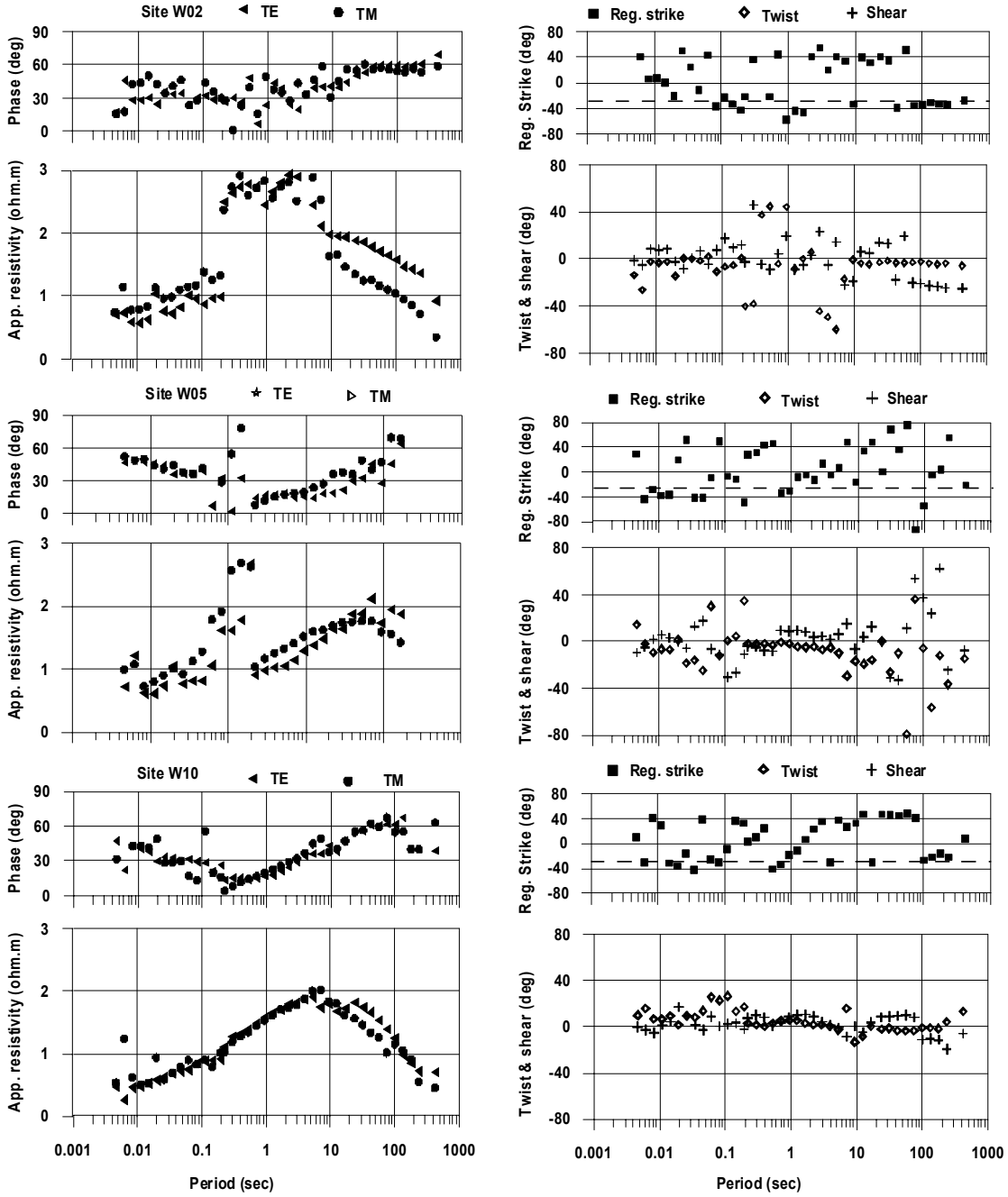

Figure 4.4. (Cont.) Results of the frequency-independent GB decomposition. (Left): Apparent Resistivity and phase curves predicated by the GB decomposition. (Right): Regional strike, Twist and shear angles.

Sites close to the Kalabsha fault fail to yield the same MT strike. This can be understood by the presence of cluster K2 to the north. Actually, only a 3D model would account for such an asymmetry of the conductivity distribution. Additionally, this cluster makes the mean electrical strike deviate by 30° from the geological one (EW).

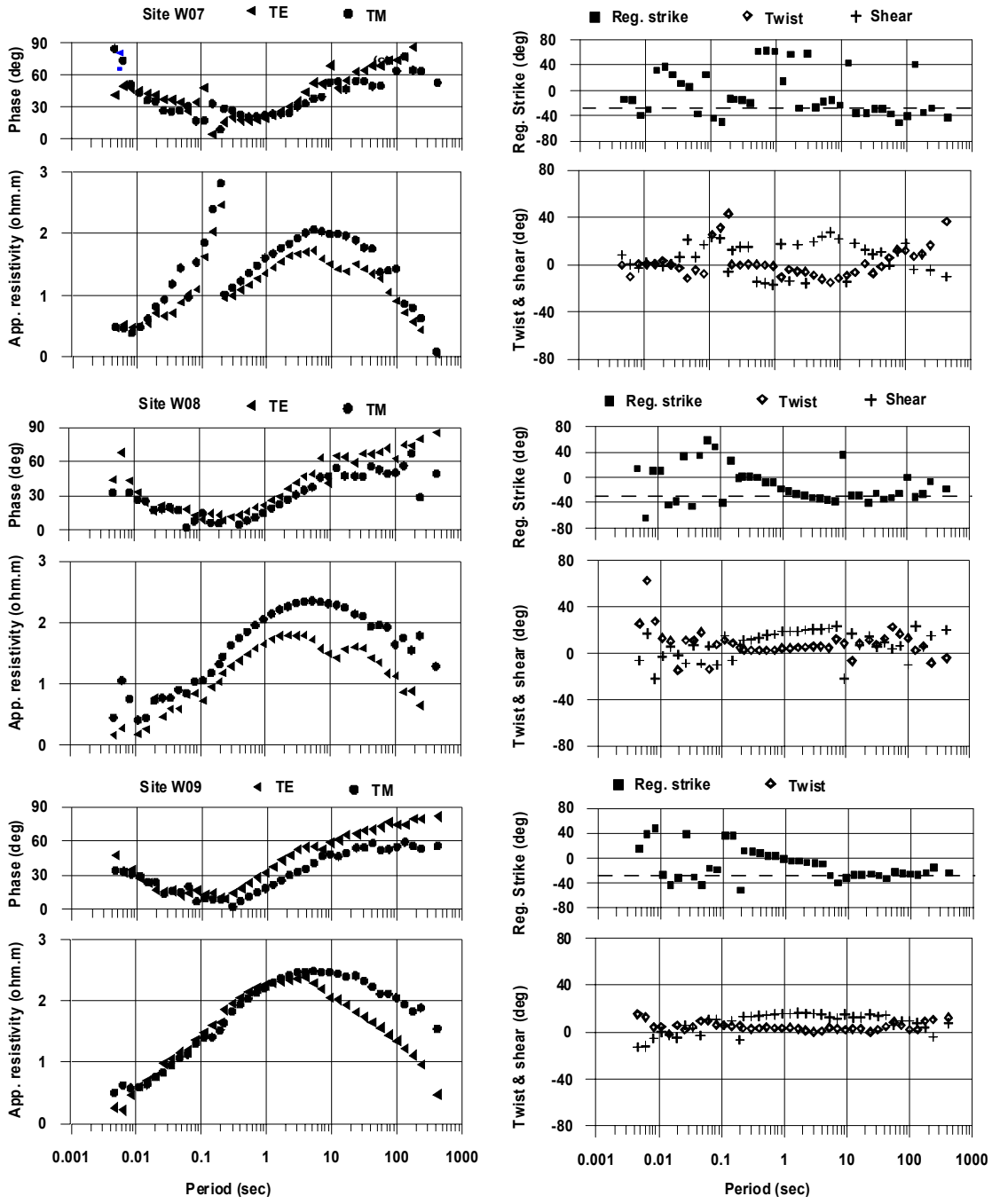

Figure 4.4. (Cont.) Results of the frequency-independent GB decomposition. (Left): Apparent Resistivity and phase curves predicated by the GB decomposition. (Right): Regional strike, Twist and shear angles.

4.3 Two-dimensional magnetotelluric modelling at Kalabsha

The aim of our work in this Chapter is to find a model that can account for the MT data at the nine sites in the Kalabsha area. As mentioned in the introductory part, we use the modelling program REBOCC.

Our real field data set consists of TE and TM mode responses at 40 periods from 0.0046 to 420 s. The initial model contains 34 layers (plus 10 air layers for TE mode) and uses 10 Ωm half-space as a starting model. The results of the inversion (after 7 iterations and RMS= 3.52) are shown on Fig 4.5-4.7. Automatic static-shift removal is fully successful, as visible for both modes at sites 1 and 9. The greatest residuals arise at longer periods for TE mode. They probably originate from 3D effects at depth (presence of off-axis cluster K2?).

The final 2D model (Fig 4.7) consists of resistive and conductive layers. The resistivity increases with depth (until 10 km). The uppermost part of the model (< 5 km) reflects the main geological structure and tectonic stresses prevailing in the area. Specific resistivity increases from both sides towards the centre of the model (25-250 Ωm). A series of plots of apparent resistivity and phase curves at each site for two modes (Zxy and Zyx) illustrates the fit between modelled and observed data (Figs 4.8, 4.9). The fit is quite good with relatively small residuals. They are represented as difference section plots, which directly compare the observed and calculated model response at each site and period.

4.4 Discussion

A detailed view of the final Kalabsha electric 2D model correlated with the well-known distribution of earthquake foci (Fig 4.7) is given in order to detect any resistivity anomalies associated to the seismic activity. It shows that there are two resistive zones at northern and southern part of the model. Between them there is a thin conductive zone that could be attributed to the fault plane. There is also a layer of high conductivity at the top of the model with about 500 m thickness, resulting from high porosity of Nubian sandstone and water percolation during the season in which the Lake covers the area. The shallow earthquakes (<15 km) are concentrated at the interface between the conductive and resistive zones. This area is known to be highly fractured (Issawi 1978). The water penetrating along fractured basement and fault plane could cause a pore pressure built up. **We draw the conclusion that the reservoir-induced seismicity is triggered by an increase of pore pressure due to reservoir loading**. The increase in pore pressure can drive a fault system to failure by the mechanism of dilatency. Studies on some recent earthquakes in the San Andreas Fault area suggest that stress changes as low as 0.1 bar are sufficient to induce failure in critically stressed zones (Stein 1999).

Seismic tomography has imaged both velocity contrasts across Kalabsha fault (Awad and Mizoue 1995b) and a low velocity anomaly within the fault. A high velocity anomaly appears at depths deeper than 16 km. This observation is significant since low velocity may indicate the presence of fluids associated with the mechanics of the shallow earthquake rupture. The changes in seismic velocity have

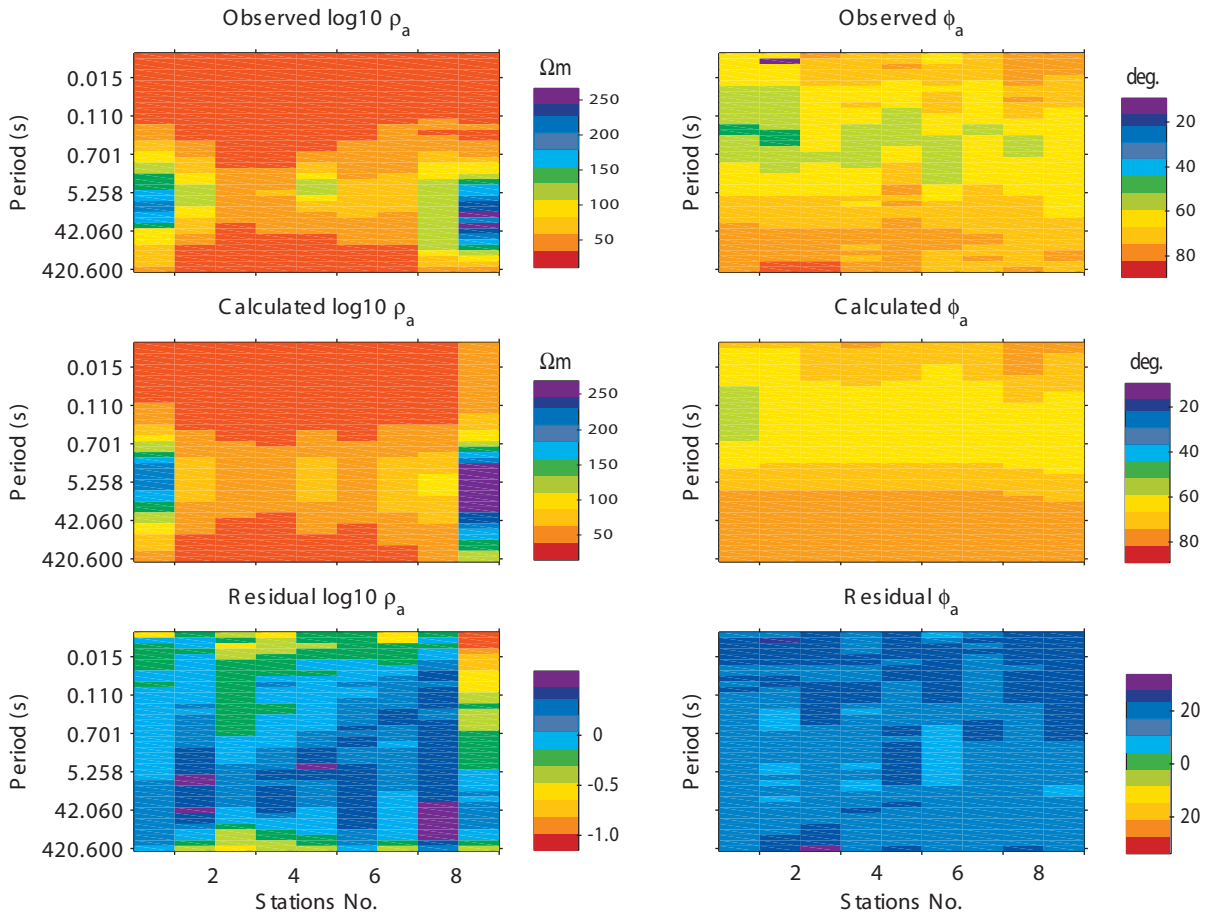

Figure 4.5. Observed and calculated pseudo-sections of MT data along the Aswan profile. TM mode

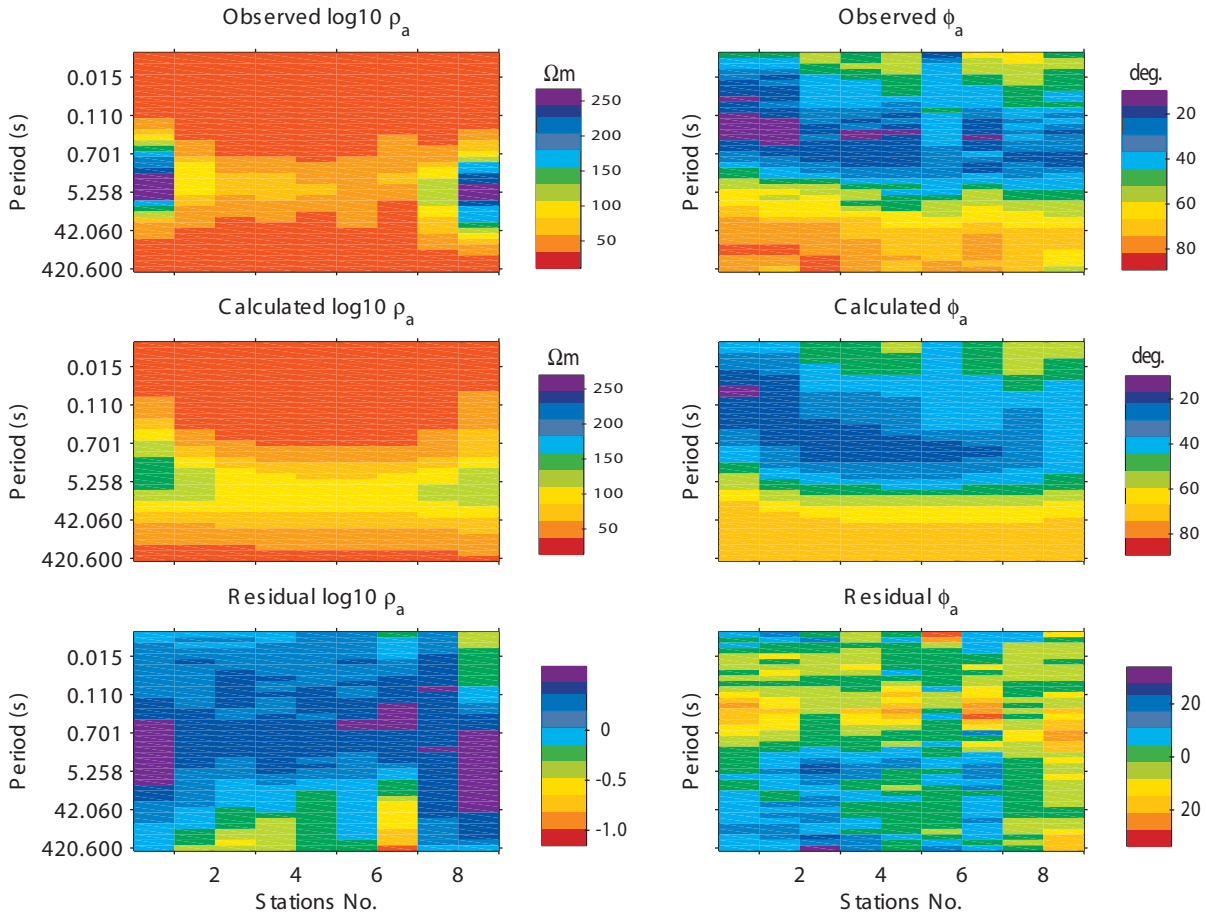

Figure 4.6. Observed and calculated pseudo-sections of MT data along the Aswan profile. TE mode

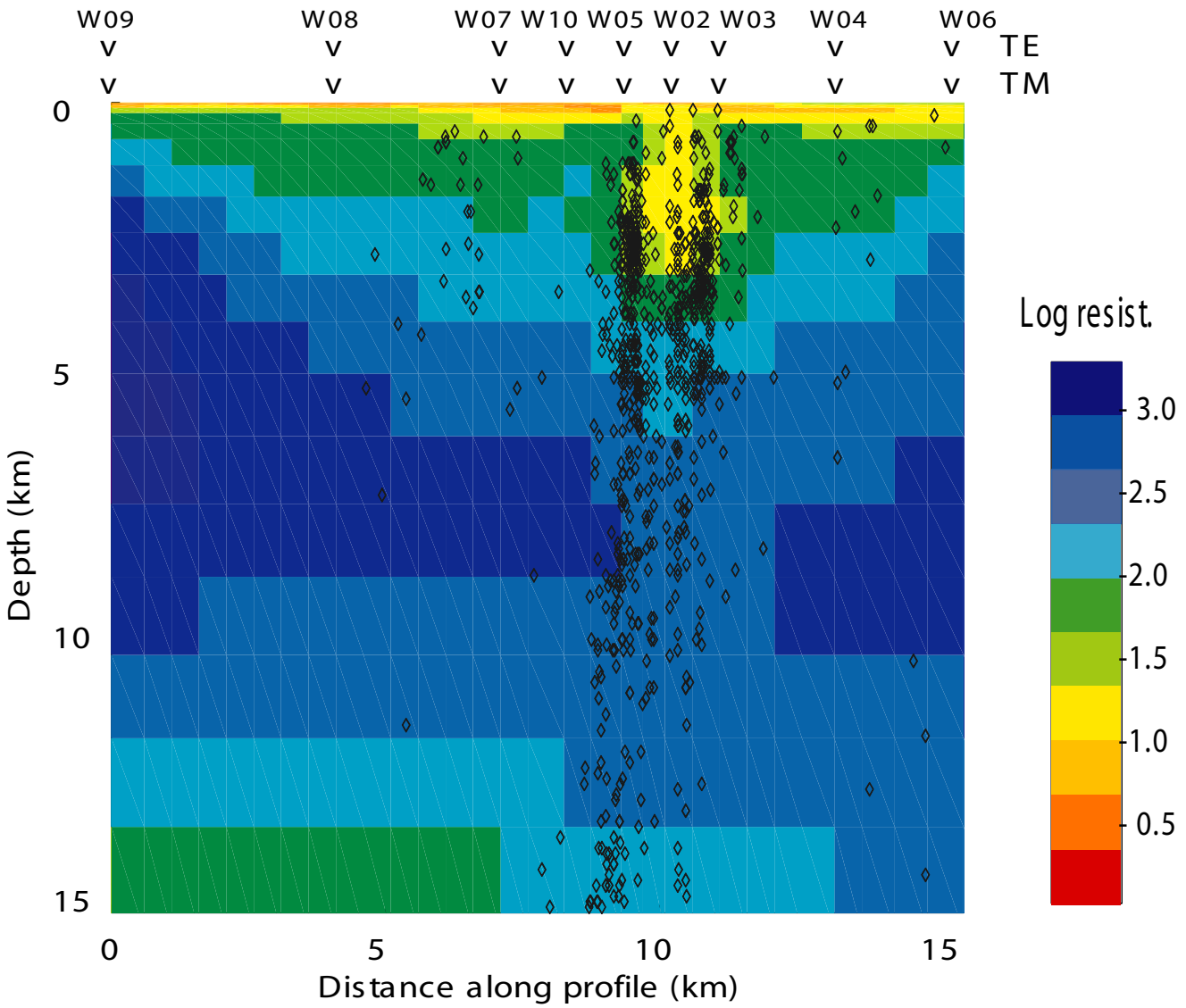

Figure 4.7. Final 2D model based on MT data of both polarizations (TE, TM) along a profile crossing the Kalabsha fault in N-S direction. The symbols above the model identify the MT sites. The location of the profile and the measurement sites are shown in Fig 4.2. Earthquake foci are shown to align in the middle of the good conducting feature.

been related to the variation of pressure and /or temperature of the medium (Raleigh and Evernaden 1981).

Mekkawi et al. (2003) analyse the Aswan seismicity pattern in the 1982-2001 period in an attempt to explain how water level loading can drive the seismicity in this period. The Aswan seismicity separates into shallow and deep seismic zones, between 0-15 km and 15-30 respectively. These two seismic zones behave differently over time as mapped by seismicity rate, depth migration, b-value, and spatial clustering. These results suggest the Aswan seismicity patterns emerge from the interplay between induced earthquakes themselves and the water level fluctuations. Our MT profile confirms the presence of fluids in the faults.

The influence of stress could be related to the two resistive zones (Fig. 4.7) in terms of stress-modulated porosity, as follows:

1) Vertical compressional stress due to loading of Lake Aswan increases pore fluid pressure.
2) Fault system of Wadi Kalabsha is strike-slip faulting and occurs under the influence of maximum compressional stress NW-SE while the direction of tensions is NE-SW (Kebeasy and Gharib 1991).

Seismicity in the Aswan reservoir is controlled by the Kalabsha fault, particularly at the intersection between NS and EW fault systems. According to Byerlee (1990), groundwater plays a major role in fault frictions, by triggering shallow earthquakes. Shallow earthquakes (< 15 km) in the area are controlled by the fluids along the fault plane (resistivity > 250 Ωm). The mechanism involves the pressure of pore water that induces a reduction of the normal stress across the fault, allowing slip to occur, and the release of ambient stress. The fault creeps from the conductive (ductile) zone and propagates to the brittle materials (i.e. granite) at the border of the resistive zone.

We believe that the present work can significantly contribute to the problem risk assessment, by bringing new information of EM origin on the fault system and its triggering mechanism. There was also a great opportunity to carry out MT soundings in an area with a high-quality seismic data catalogue extending over 20 years. As regards the quality of the MT measurements, the Kalabsha area was ideally suited due to the absence of any man-made EM perturbation source (70 km off Aswan city).

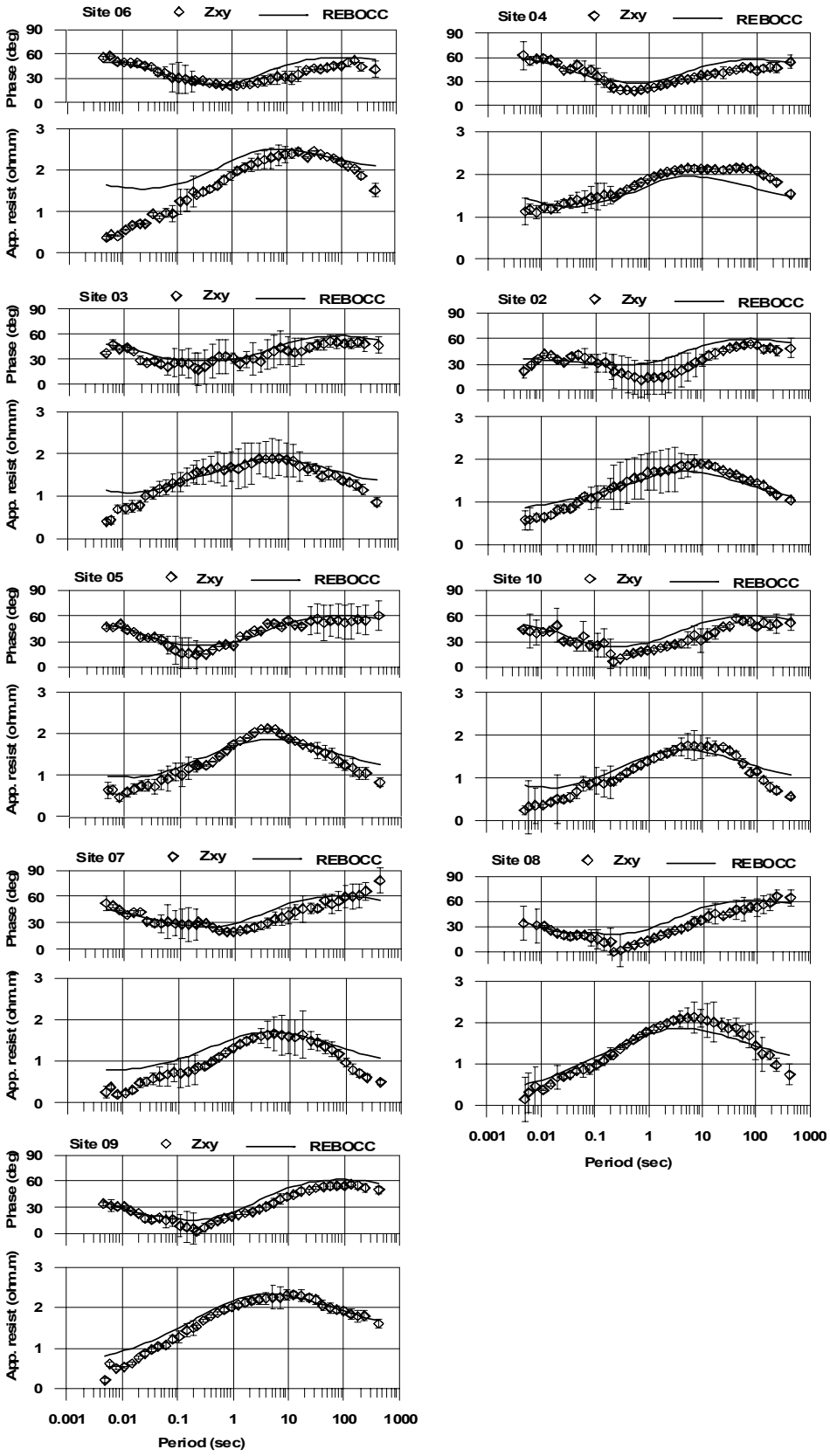

Figure 4.8. Observed and calculated apparent resistivity and phase (TM mode) of the Kalabsha 2-D model.

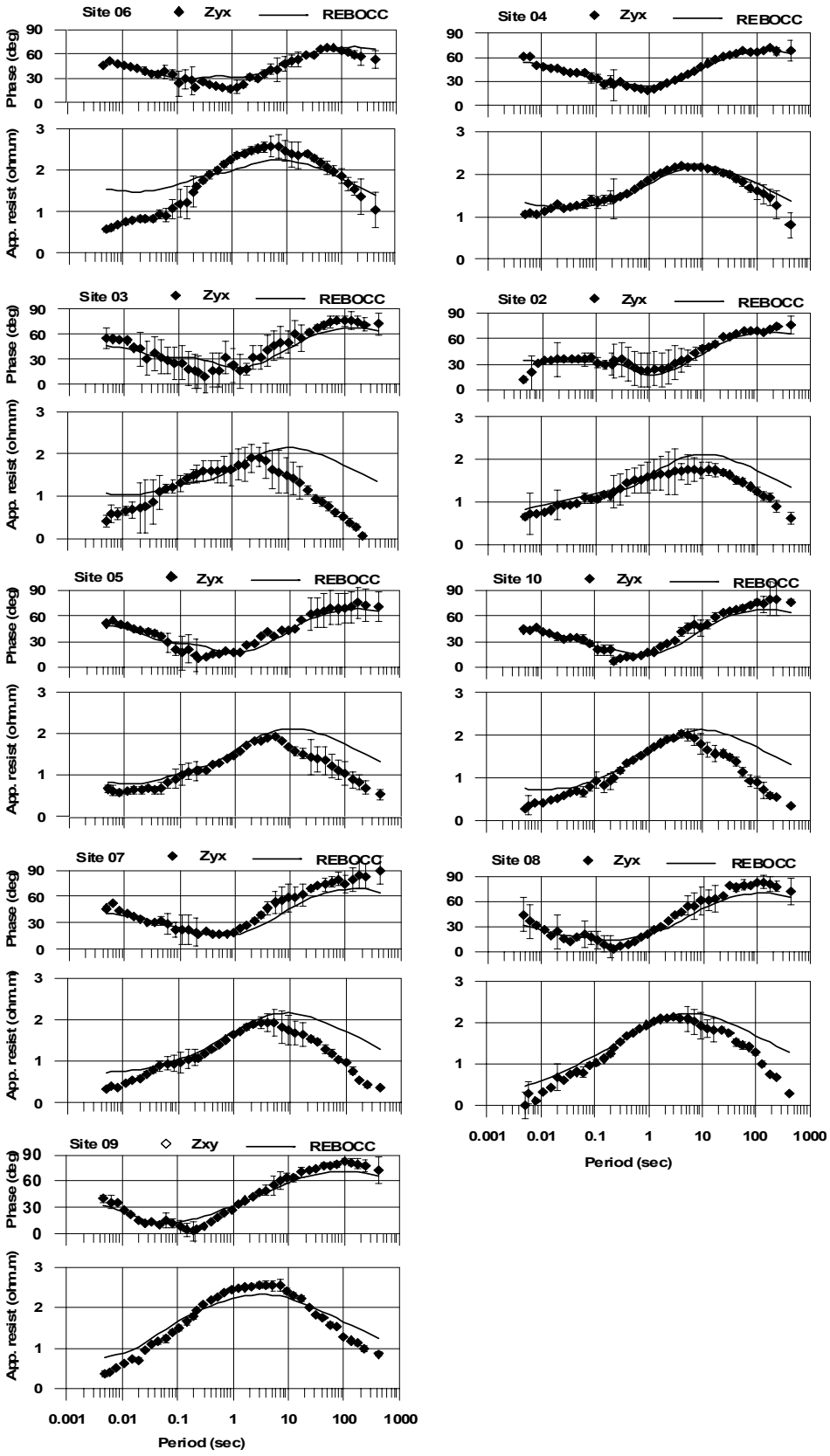

Figure 4.9. Observed and calculated apparent resistivity and phase (TE mode) of the Kalabsha 2-D model.

5. The Remiremont area

5.1 Introduction

A recently published paper (Audin et al. 2002) attracted our attention on a totally different area. For the sake of completeness and comparison between seismicity and crustal conductivity in various conditions, we decided to bring our attention to the Vosges Mountains in eastern France. More precisely, our investigations were extended to the Remiremont fault zone, where a seismic crisis developed in the Eighties.

The Remiremont area lies west of the Rhine graben which is a major element of the Cenozoic rift system of western and central Europe (Fig. 5.1); it has been tectonically active since the late Eocene. It was parallel by the development of the East Africa-Red Sea-Gulf of Suez rift systems (Ziegler 1992).

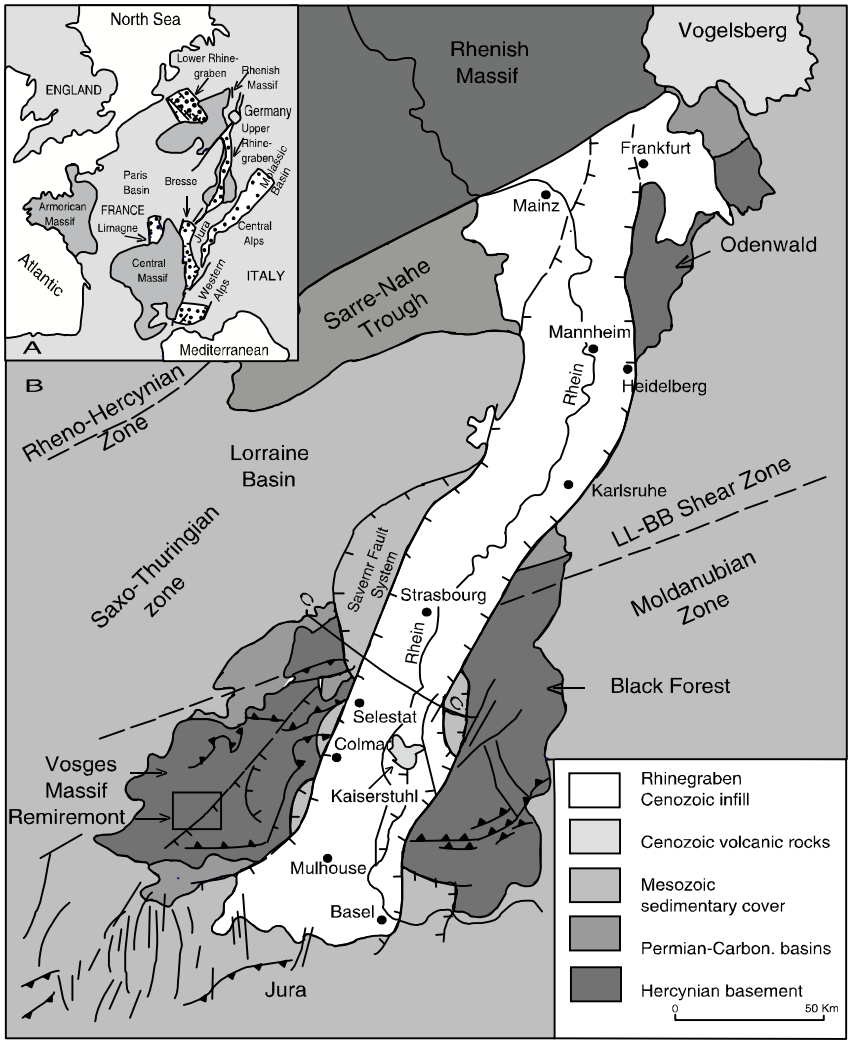

Figure 5.1. (A) General outline of the West European rift system (B) Geological and Structural map of the Rhine graben showing location of the ECORS-DEKORP line (C-C`) and Remiremont area (after Brun et al. 1991).

Since the middle Pliocene, the activity in the southern Rhine graben has been dominated by left lateral shear on the N-S faults that run parallel to the graben axis (Abhorer 1975). The Lalaye-Lubine-Baden-Baden shear zone (LL-BB) is a major fault that separates the Moldanubian zone to the south from the Saxo-Thuringian zone to the north. It crops out as a steep, southward dipping shear zone and shows evidence of multiphase movement history (Fig. 5.1). Basement exposure in the Black Forest and Vosges Mountains indicate that the Moldanubian crust is mostly composed of high-grade amphibolite to granulite facies polymetamorphic gneiss intruded by voluminous late carboniferous granitoids (Brun et al. 1992).

5.2 Major structure of the Rhine graben

The Rhine graben is one of the best-studied continental rifts in the world. Numerous geological and geophysical studies have been carried out during the last 25 years. Seismic refraction and reflection surveys, geothermal, geomagnetic deep sounding and magnetotelluric measurements provide detailed information about structure of the crust and upper mantle.

The thickness of the crust and the nature of the layer under the graben are shown in Fig. 5.2. The upper crust with velocities 5.9 to 6.2 km/s extends until 20 km. There is a lithospheric channel (low velocity layer) between 7-10 km containing crystalline material of lower density that makes some level of brittleness and instability. The lower crust is clearly thinned between 20 and 24 km. The upper mantle (velocities 7.9 to 8.1 km/s) makes up a broad convexity (Sitter 1983).

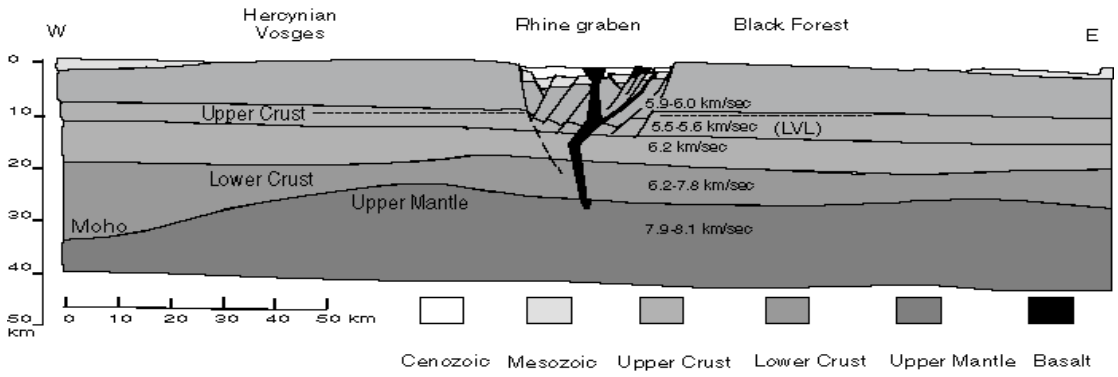

Figure 5.2. Structural cross-section of the southern Rhine graben provided by seismic refraction data. Notice the two weak and ductile horizons: the lithospheric channel of the upper crust and the layered lower crust (Sitter 1983).

The seismic reflection profile (C-C') obtained by the ECORS/DEKORP groups (Fig. 5.1) confirmed what preceded, and in particular the bedded structure of thinned lower crust in an asymmetrical way. Brun et al (1991) stated that the Moho is sharply defined at the bottom of the lower crust. It is clear under the Black Forest and is particular obvious below the Vosges Mountains (Fig. 5.3a).

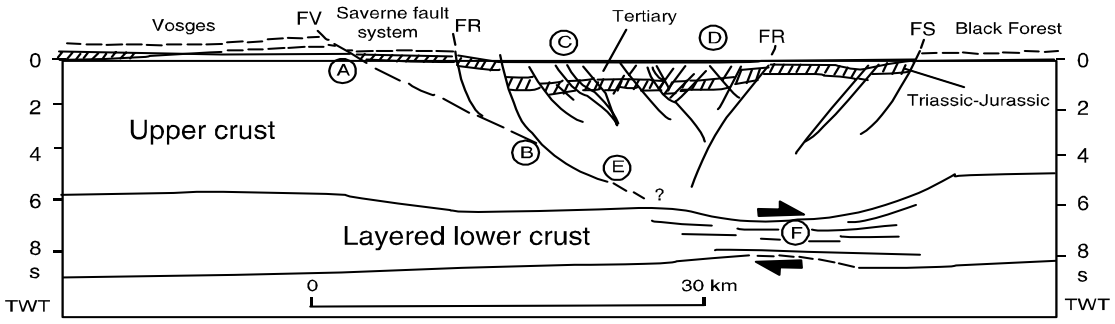

Figure 5.3a. Interpretative cross-section of the Rhine graben by deep seismic reflection results. The main graben border faults (A, B) combine to a listric master fault (E). Thinning of the laminated lower crust (F) indicates clearly asymmetry. The graben is characterized by synthetic and conjugate normal faults (C, D) in the particular area of the deep Sélestat basin; elsewhere collapse steps are due essentially to antithetic faults.FV: Vosges fault, FR: Rhine fault, FS: Black Forest fault (after Brun et al. 1992).

According to Sitter (1992), the mechanism that can be considered for the Rhine graben to explain the thinning of the lower crust is as follows: uplifting of the asthenosphere in the upper mantle resulted from Alpine collision with Africa plate. The Alpine collision zone may have been playing a role in the tensional reactivation of the Permo-carboniferous fracture system, thus controlling the localisation of its individual graben (Ziegler 1992). This upper-mantle plume or thermal interplating in the southernmost part of the Rhine block would have caused thinning of the lower crust. Collapse could result from the thinning of the ductile crust or the stress of the mantle.

Magnetic variation and magnetotelluric data (Richard et al. 1981 and Berktold et al. 1986) have been inverted to obtain electrical resistivity distribution as a function of depth in the Rhine graben. These authors found the existence of a high conductive zone between 10-15 km, a depth coinciding almost exactly with the low velocity channel. High temperature was also found at shallow depths in the Rhine graben. Werner and Parini (1980) interpreted these high temperatures as hydrothermal circulation at greater depths (6 km). Thus, the transition between brittle and ductile crust should become noticeable in seismically active regions (Plenefish and Bonjor 1997) using the distribution of the deepest earthquakes (Fig. 5.3b). They concluded that the deepest earthquakes in any locality should not be deeper than the brittle-ductile transition.

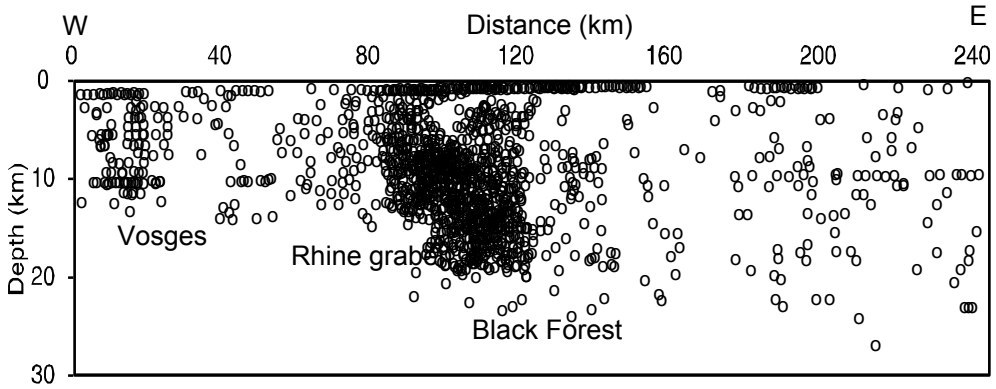

Figure 5.3b. Depth distribution of foci (1971-1994) in a cross-section perpendicular to the strike of the southern Rhine graben (Plenefish and Bonjor 1997).

5.3 Seismicity in the southern Rhine graben.

The historical seismic activity in the southern Vosges is high (yellow rectangle in Fig. 5.4). The most damaging earthquake occurred in the area in 1682. This earthquake was felt as far away as Versailles (400 km to the west) and destroyed the roof of Remiremont church (Audin et al. 2002).

Seismic activity occurs along the entire graben system. The upper Rhine graben and its Northwest prolongation through the Rhine Massif belong to the most seismically active regions. The seismicity in the southern Rhine graben represents the largest data set. The majority of the events are located in or close to the Rhine graben (eastern and western) fault system (Fig. 5.4).

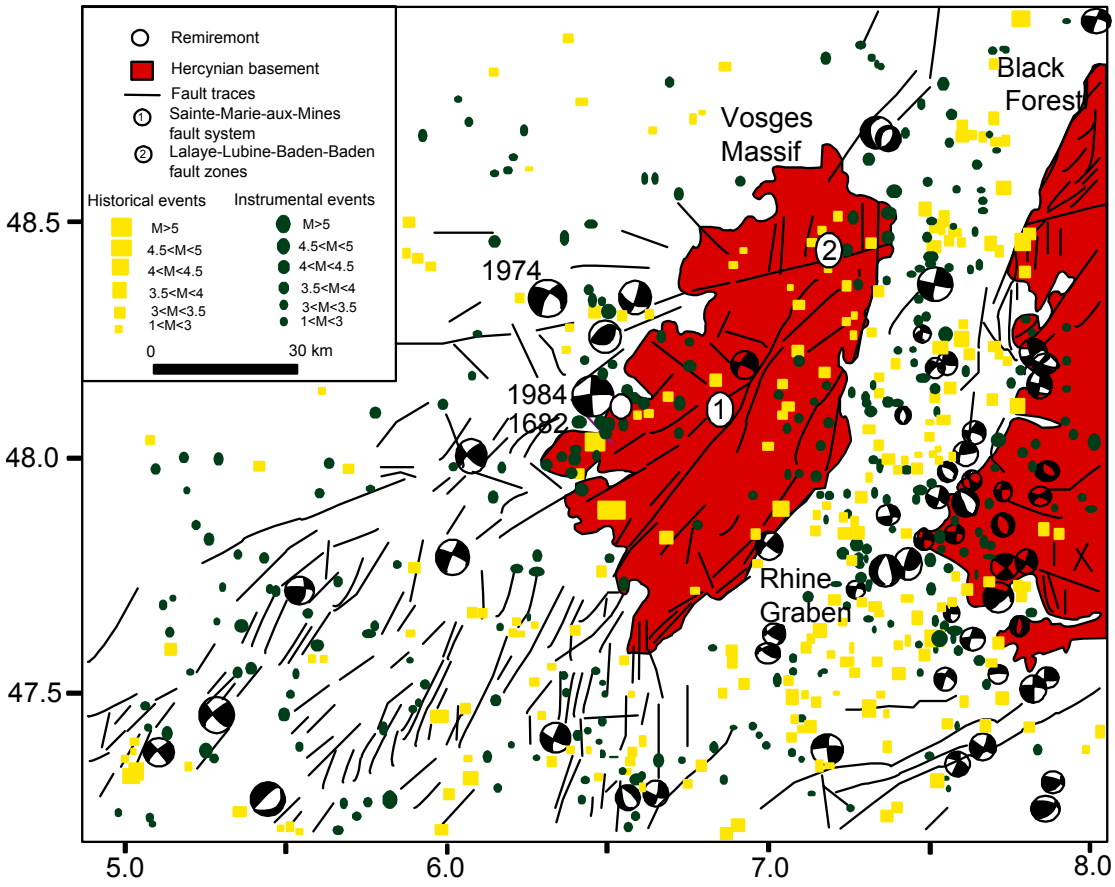

Figure 5.4. Simplified tectonic map (faults are drawn with black lines) of the Remiremont area around the southern Rhine graben showing location and corresponding fault plane solution of events (Audin et al. 2002). Focal mechanisms are given in equal-area projections of the lower hemisphere.

The largest density of seismic stations is located in the Black Forest and in the Swiss Jura, allowing very precise determination of the focal mechanisms in the region. Most of the earthquakes are strike slip movement. There are also a significant number of normal faulting events. All mechanisms exhibit some oblique component of slip.

The maximum compressional axis acts in a SE-NW to SSE-NNW direction and the minimum compression axis in a SW-NE to WSW-ENE direction (Plenefish and Bonjer 1997). The accuracy of earthquake location is ±1.5 km horizontally and 2 km vertically. It indicates that the thickness of the seismogenic layer of the crust shows strong lateral variations: >15 km in Vosges and >30 km in Rhine graben and Black Forest, (Bonjer, et al. 1984).

The earthquake catalogue of the EOST (Ecole et Observatoire des Sciences de la Terre) and RéNaSS (Réseau National de Surveillance Sismique) was used to construct an earthquake distribution map from 1980 to 2003 (Fig. 5.5). It contains about 230 events ($1 < M \leq 5.5$). The area became still more interesting after the M = 5.5 quake of 22 February 2003 that occurred about 10 km north of Remiremont. The seismicity of this area is characterised by a shallow depth (< 15 km). Error for the RéNaSS catalogue in the vertical distance *erz* is ±5 km. The magnitude distribution with time is shown in Fig. 5.6. This value is smaller than 4 for all except two periods. The first period (1984-1985) is clustered about Remiremont whereas the second one is near Epinal (M = 5.5).

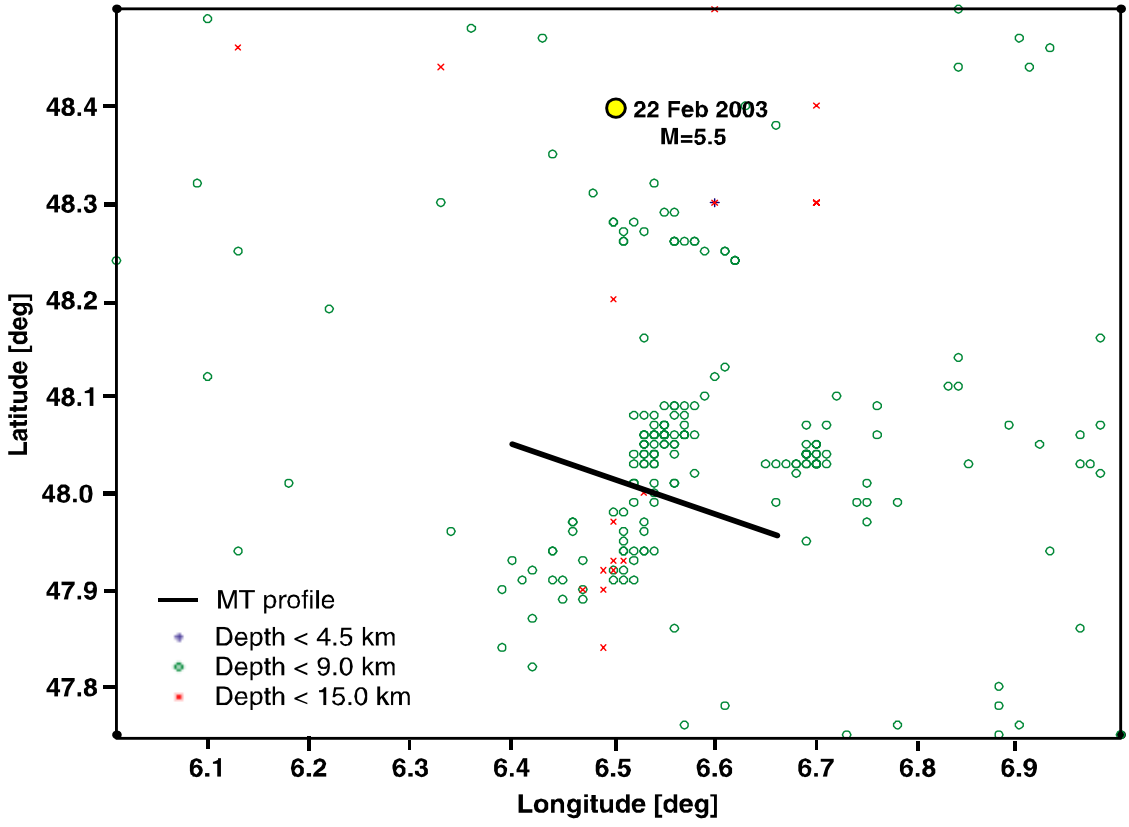

Figure 5.5. The 2D space-distribution of earthquake activity in Remiremont area with focal depth.

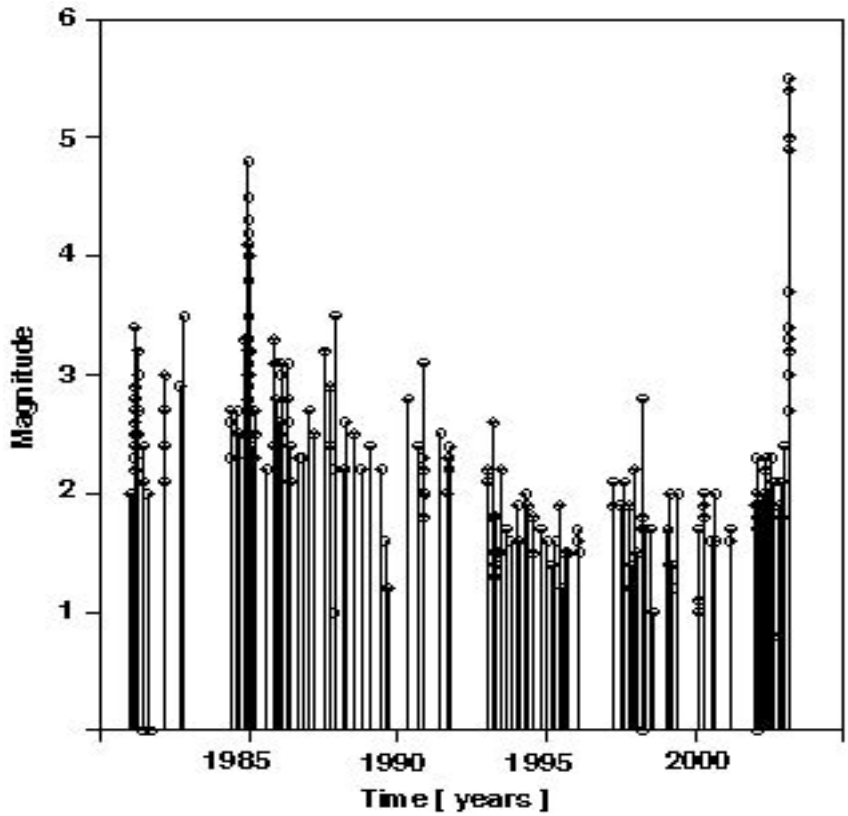

Figure 5.6. Time-magnitude distribution of earthquakes with 1< M < 5.5) between 1980-2003.

Seismicity is observed in the area during 1973-1974 (Epinal sequence, Fig. 5.7). The trends of Remiremont and Epinal are NE-SW and NW-SE respectively. The seismic events of Remiremont (M = 1.0-4.8) are found to align on 40 km along the southern Vosges Massif to the west. The b-value of the Gutenberg-Richter distribution of Remiremont seismicity is 0.83 ±0.03 (Audin et al. 2002). The focal mechanism in the area, including those related to the main shocks near Remiremont and Epinal, are roughly N30ºW principal compressive axis and N60ºW minimum principal axis, consistent with the World stress map (Delouis et al. 1993; Mueller et al. 2000).

Migration patterns of seismicity in the Remiremont area (Fig. 5.7) lead Audin et al. (2002) propose that intrusions of fluids might be at the origin of the earthquakes. They attribute the migration pattern to connectivity of fluids; linear seismicity migration would reflect a zone of high permeability, allowing the propagation of transient pore pressure changes. Periods of cluster activity could be ascribed to periods of pore pressure build-up around barriers.

The article by Audin et al. (2002) and its conclusions attracted our attention and it was decided to include in this thesis MT investigations of this area, since the problems displayed close similarities with our previous Egyptian site.

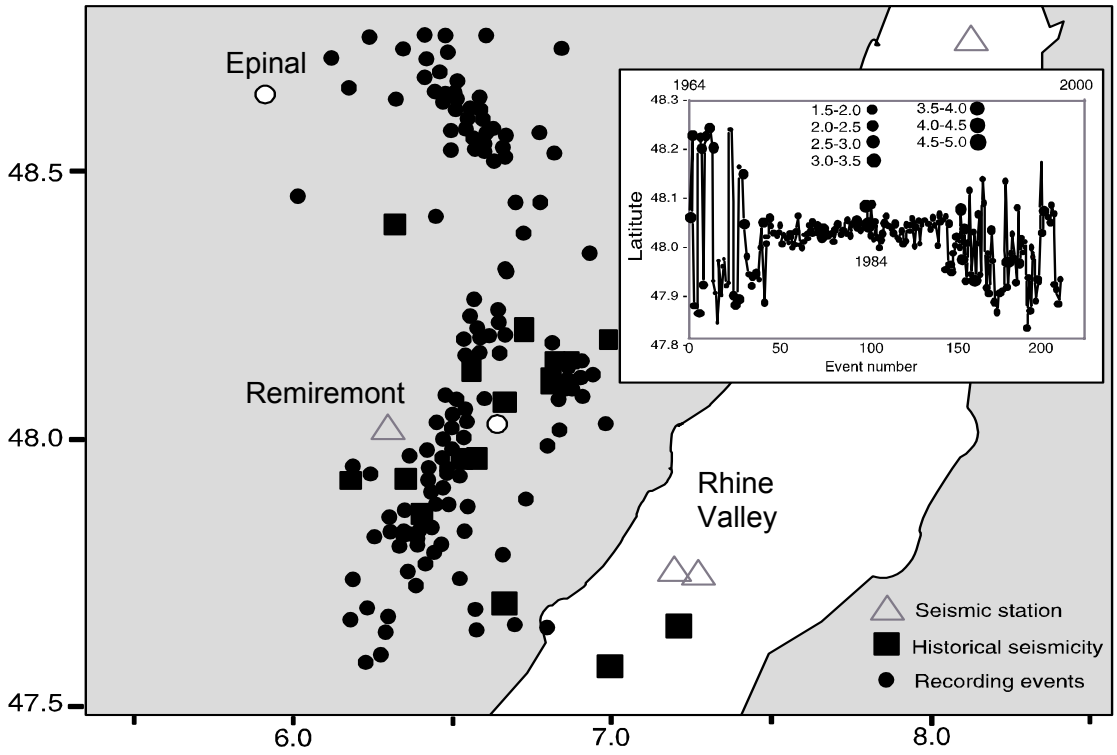

Figure 5.7. (Upper) The seismic activity in southern Vosges Mountains, showing two cluster zones. (Lower) Spatial and chronological seismic pattern in the area (Audin et al. 2002).

5.4 Tectonic and geological setting of southern Vosges

The uplifted lower crust/upper mantle boundary (Moho) reaches its shallowest depth 24-26 km in southern Vosges. The interface depth was determined by using seismic profiles and different gravity models (Grellet et al. 1993). They concluded also that the major tectonic episodes were Hercynian and Triassic and played important role in the tectonics of the area. The Hercynian Vosges Massif is composed of two regions, the Saxo-Thuringian and Moldanubian Vosges, which lie respectively south and north of the LL-BB fault zone (Fig. 5.1). Triassic layers are found in the sedimentary basin of Vosges Massif. These layers contain evaporites and salt.

The Remiremont area lies in the southern Vosges which consists mainly of crystalline rocks (granitoids, migmatites, leucogranites) overlain with upper Devonian to Dinantian cover (Fig. 5.8). The Dinantian consists of volcano-siliceous deposits and greywacke (sandstone), assembled in 'Culm' and is characterised by Lower Carboniferous (Schneider 1990). Mesozoic is only represented by Triassic clastic sediments.

Quaternary covers most middle parts of the area. It is composed of sandstone, argillaceous gravels and alluvial of Remiremont (Fig. 5.2). The major tectonic feature is the Sainte-Marie-aux-Mines fault that cuts the southern Vosgian Massif from NE to SE (Fig. 5.4). This fault is considered ductile left-lateral strike slip fault (Fluck et al. 1991). The long geological history has resulted in a complex fault pattern (BRGM 1979).

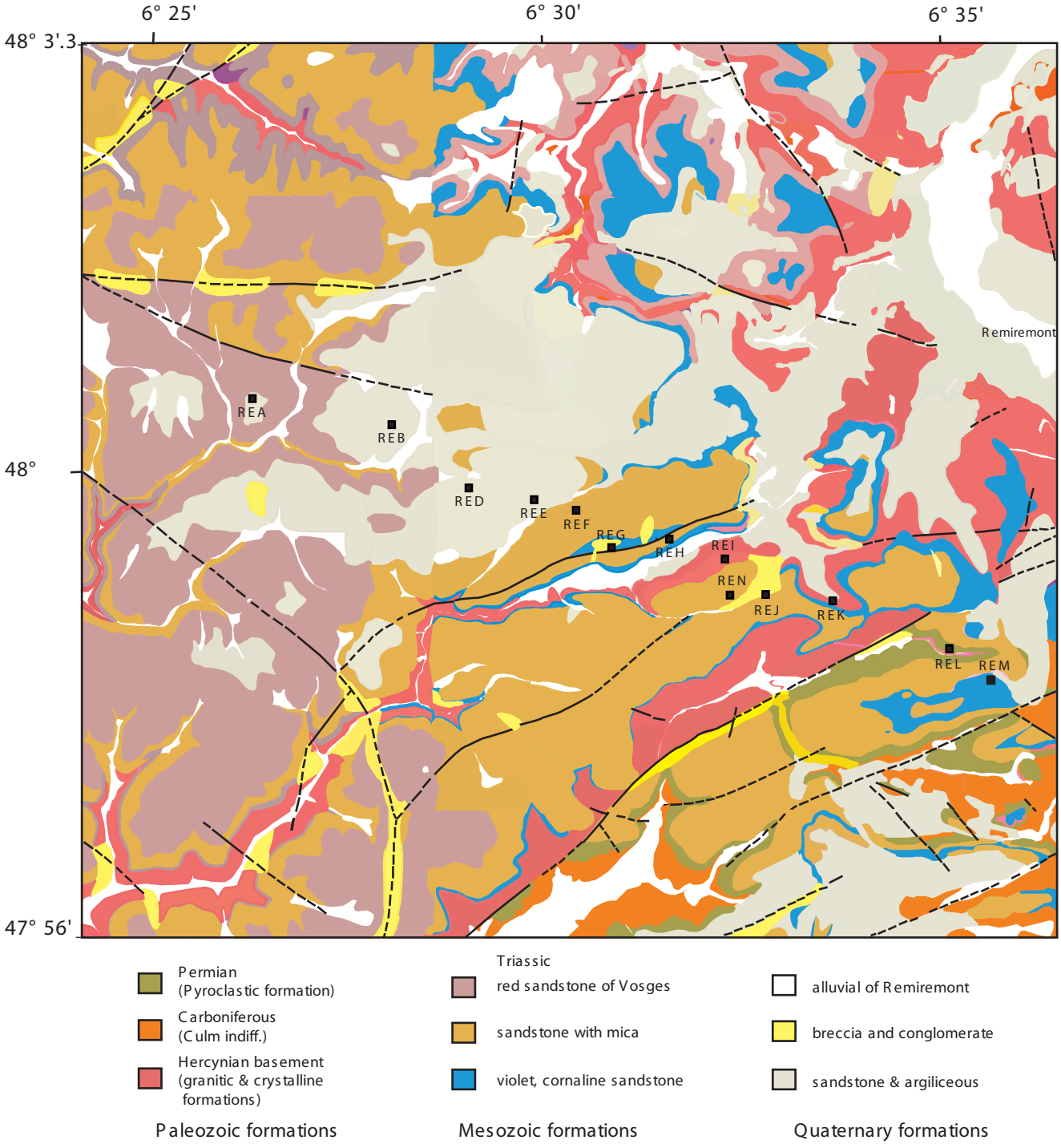

Figure 5.8. Geological map of the Remiremont region (BRGM, 1979), and location of MT stations.

5.5 MT acquisition and analysis

As we mentioned above, a series of recently published papers (Unsworth et al. 2000; Adam 2001; Bedrosian et al. 2002) have suggested the possibility of conductive materials (fluids) playing a significant role in areas of high seismicity. Supposing that hydrothermal fluids and ore minerals (e.g. graphite, salt or sulphides) accumulated in the conductive fractures (faults, dykes), decreasing the bulk resistivity, the high seismicity in the area can be explained by these conducting materials. Thus, the goals of our measurement are to determine the precise location of the active fault(s) in the area and to study the connection of the Remiremont seismicity to the resistivity structure. To do so, a MT profile was carried out across documented fault(s) in the Remiremont region, choosing the best profile location in terms of maximum focal density and minimum cultural noise.

The MT measurements took place along a single profile in two field trips during August and September 2002. The profile extends 13 km from NW to SE (Fig 5.8), and consists of 13 observational stations, with an average spacing of 1 km. Most stations were located at significant distances off the road. Table 7 shows the listing of the MT sites.

Table 7. MT sites listed in chronological order.

Site Name	Date	Latitude	Longitude	Elevation (m)	Remote Ref.
REK	19.8.2002	47º 58.93 N	06º 33.47 E	675	REM
REM	19.8.2002	47º 58.19 N	06º 35.69 E	735	REK
REJ	21.8.2002	47º 58.99 N	06º 32.52 E	620	REL
REL	21.8.2002	47º 58.49 N	06º 35.10 E	590	REJ
REH	22.8.2002	47º 59.51 N	06º 31.17 E	590	REI
REI	22.8.2002	47º 59.32 N	06º 31.96 E	540	REH
REF	23.8.2002	47º 59.78 N	06º 29.87 E	600	REG
REG	23.8.2002	47º 59.43 N	06º 30.36 E	570	REF
RED	17.9.2002	47º 59.99 N	06º 28.36 E	546	REE
REE	17.9.2002	47º 59.88 N	06º 29.27 E	570	RED
REA	18.9.2002	48º 00.83 N	06º 25.32 E	521	REB, REN
REB	18.9.2002	48º 00.58 N	06º 27.28 E	545	REA, REN
REN	18.9.2002	47º 58.99 N	06º 32.02 E	610	REA, REB

Three instruments were used simultaneously in this study, with full measurement of the three magnetic components. The MT data were measured in the north-south and east-west directions. The electric dipoles were 50 m long.

5.6 Induction vectors and strike determination

The geological strike is more safely obtained by measuring the vertical magnetic field induction coefficients (induction arrows, Schnegg 1998). The directions of the induction vectors, which are less affected by static effects than electric fields, safely indicate the geologic strike (or rather, a direction perpendicular to strike). The ratio of vertical to horizontal magnetic fields (induction arrows) may be used to infer the presence of linear zones of anomalous current concentrations in the subsurface. In 2D case, the real arrows point away from electrical conductors or nearby conducting contrasts. No vertical magnetic field component is observed generally in the absent of lateral contrast (1D case).

In Fig. 5.9a-b the real and imaginary tipper arrows are plotted versus the logarithm of the period. In the upper part of the subsurface, i.e. at periods <1 s, the real components at **RED and REE point in opposite directions**, suggesting the presence of a conducting structure, probably a **fault running between the two sites**. The same situation can be observed at REI and REJ, culminating at REN, a location with strong 3D effects, according to its MT response.

The electric conductivity structure becomes more complex with increasing induction range (longer period). The induction arrows at sites REL and REM are small, because the shallow subsurface is conductive in all directions at the respective depths. The arrows become larger for the longer periods, because as the induction range widens, a greater volume of the highly conductivity area is sampled.
The real induction arrows at different periods are superimposed on the known geological features in Figures 5.10a-b for comparison. Figure 5.10a shows the induction arrows at a period of 1.24 s. Their uniform WNW-ESE direction indicates that on the whole area the subsurface faulting occurs toward a fixed azimuth, at right angle with the arrows.

For periods in excess of 1 s, the induction arrows slowly rotate into a new direction, reflecting the electrical strike at depth. Before computing MT apparent resistivity and phase, the measuring axis is mathematically rotated into that direction (N40ºW). This angle is in good agreement with both MT impedance axis and tipper direction. Surprisingly, the newly determined strike of the electrical conductivity is no longer aligned with the faults directed NE-SW, but instead at right angle, in direction NW-SE.

After rotation, the two impedances yield Rhomax and Rhomin curves. In case of a 2D structure, the tipper points toward the high resistive zone. Rhomax coincides with the strike direction. It is designated as E-polarisation. Rhomin (H-polarisation) is perpendicular to the strike for further 2D modelling.

Obviously, the geology or at least, the electrical conductivity distribution is neither horizontally nor vertically uniform. Therefore, we will treat the subsurface and the deep effects separately.

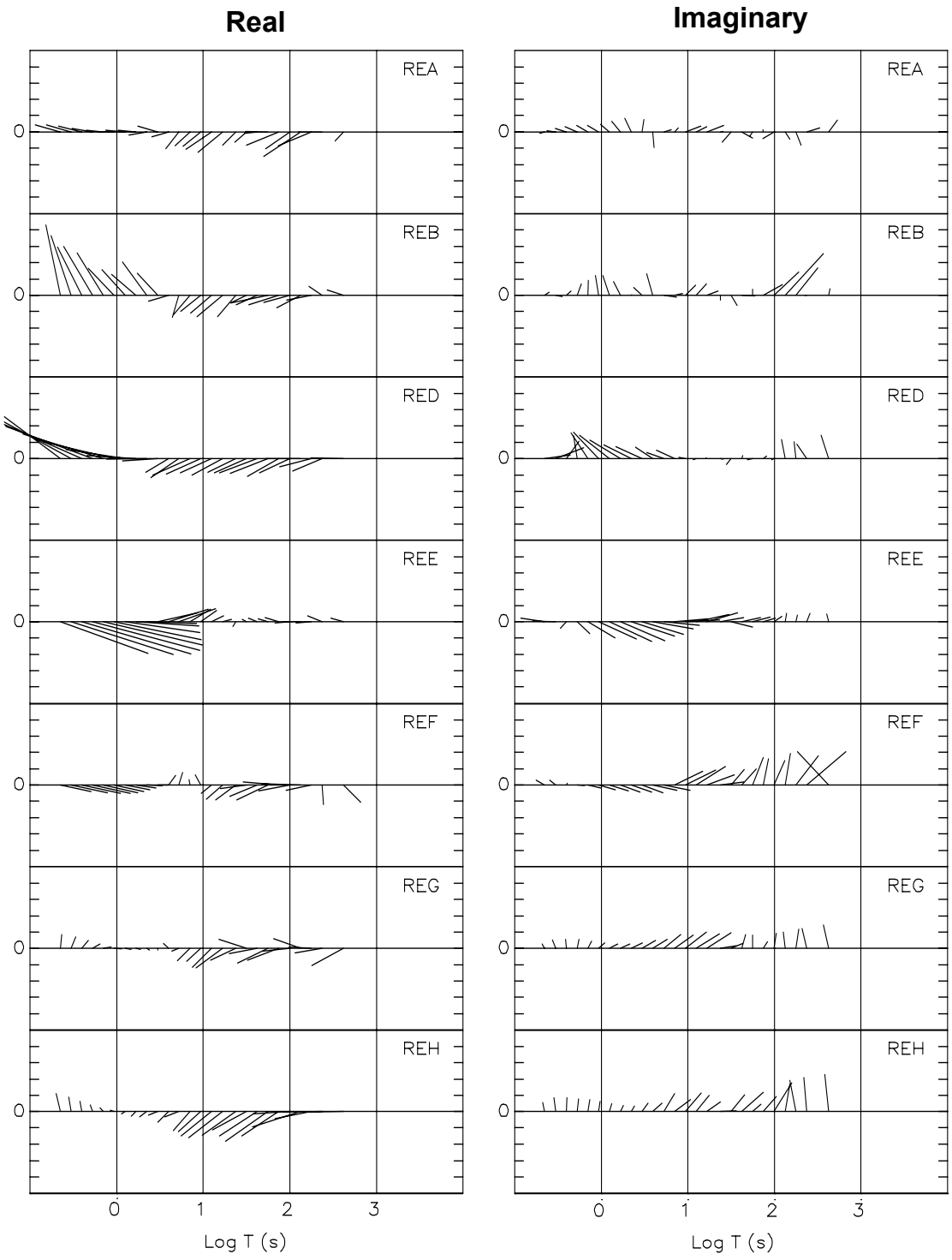

Figure 5.9a. Real (left column) and imaginary (right column) components of the tipper at sites REA to REH (geographic north is perpendicular to the time axis). In the upper part of the subsurface the real components at RED and REE point in opposite directions, suggesting the presence of a conducting structure -probably a fault- between the two sites. Vertical axis varies between –1 and +1.

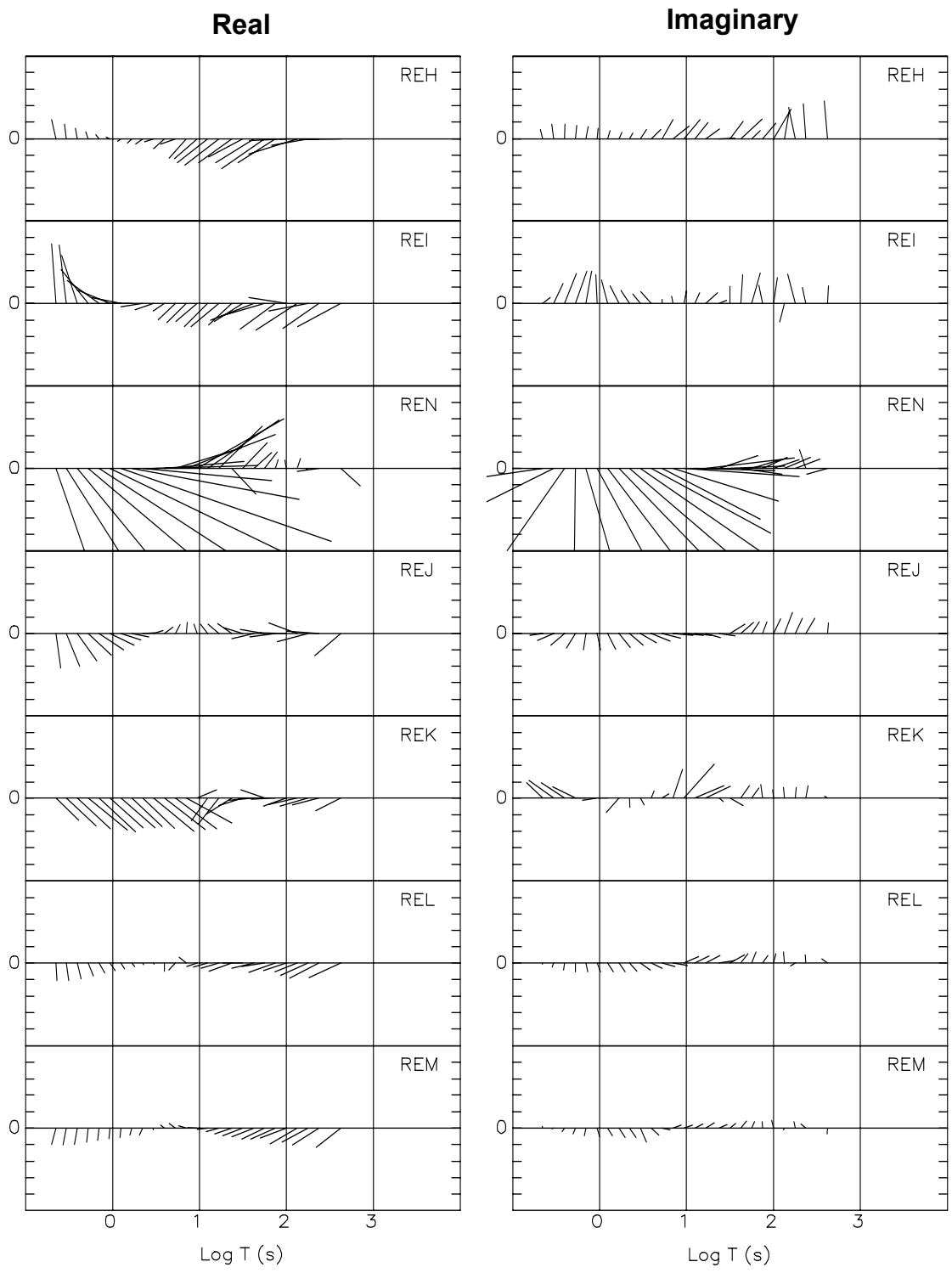

Figure 5.9b. Real and imaginary components of the tipper at sites REH to REM (geographic north is perpendicular to the time axis). The direction of the real components at REI and REJ indicate the presence of a conducting structure -probably a fault- between them. Vertical axis varies between –1 and +1.

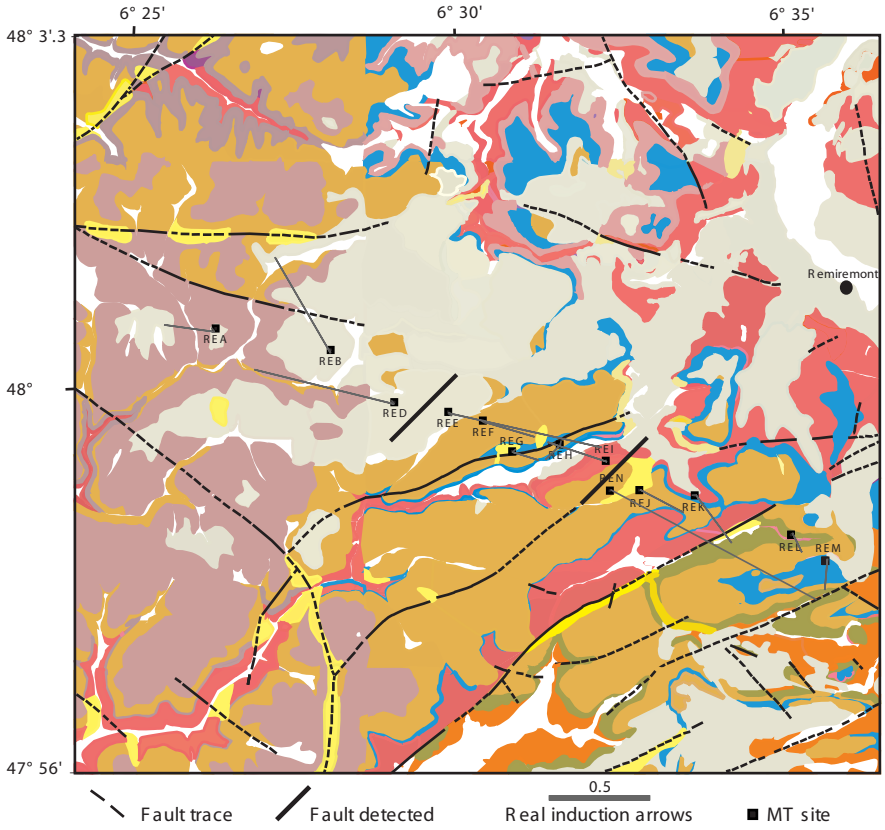

Figure 5.10a. Real tipper arrows at period 1.24 s and sites REA to REM, superimposed on a geological map. Two conductive features of the subsurface - probably faults- are detected with the tipper. One of them is located on a documented fault.

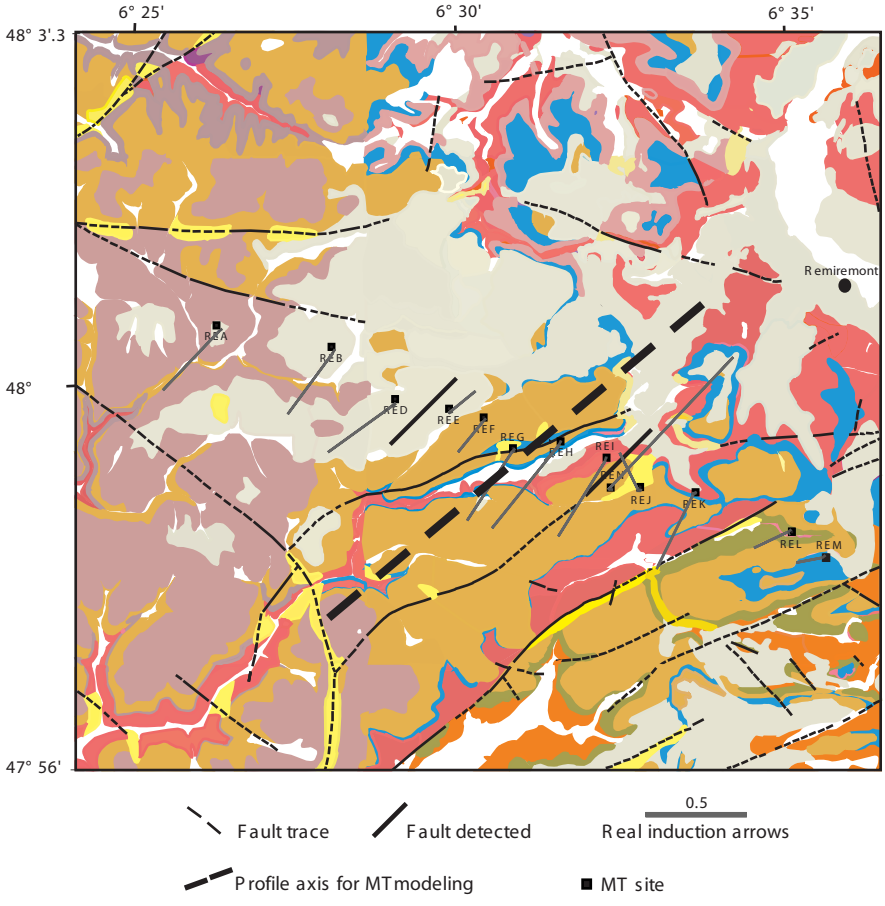

Figure 5.10b. Real tipper arrows at period 12.4 s at sites REA to REM, superimposed on a geological map. on a documented fault.

5.7 Apparent resistivity and phase

Fig. 5.11 shows the apparent resistivity and phase for two polarizations Zxy and Zyx at the sites REA to REM of the rotated impedance tensor with the coherency and skewness parameters. The MT sounding curves are very similar from site to site along the whole profile. The apparent resistivity modes Zxy and Zyx diverge above period 1 s, indicating 2D geometry. The two modes steadily increase from values of hundreds of Ωm at the surface (0.001 s) to thousands of Ωm. That is no surprise, since the profile is never far away from the high-resistive granite. Rhomax curves are gently increasing between 1,000-10,000 Ωm, whereas Rhomin curves show decrease, hinting at a deep conducting body (fault?) embedded into a resistive matrix.

According to the coherency values of Fig. 5.11 the MT data seem to be of good quality except at station REN, for undetermined reason. From the skewness values, structural dimensionality suggested simple 2D conditions, at least for periods < 100 s. A more complex structure or a gradual strike angle variation is suggested at periods above 100 s.

Maximum apparent resistivities of 30,000 Ωm or more are observed at periods 10-100 s of site REL and apparent resistivity curves decrease gradually between 100-420 s. The Zxy- polarisation indicates phase close to 45º at long periods and between 10º and 30º at short periods. For Zyx-polarisation, the phase behaves in an unexplained way at longer periods.

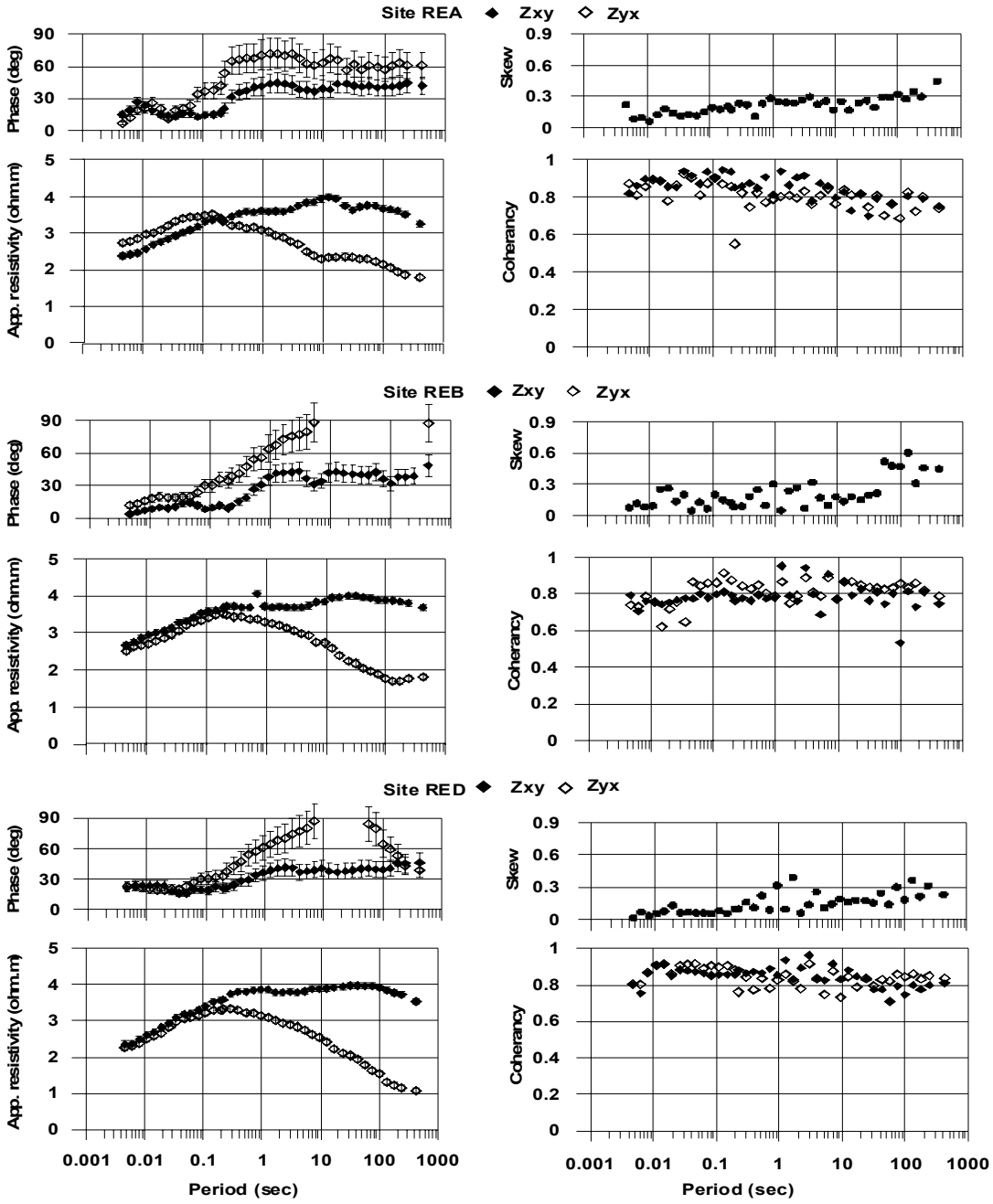

Figure 5.11. MT transfer function (Zxy, Zyx), skew and coherency versus period.

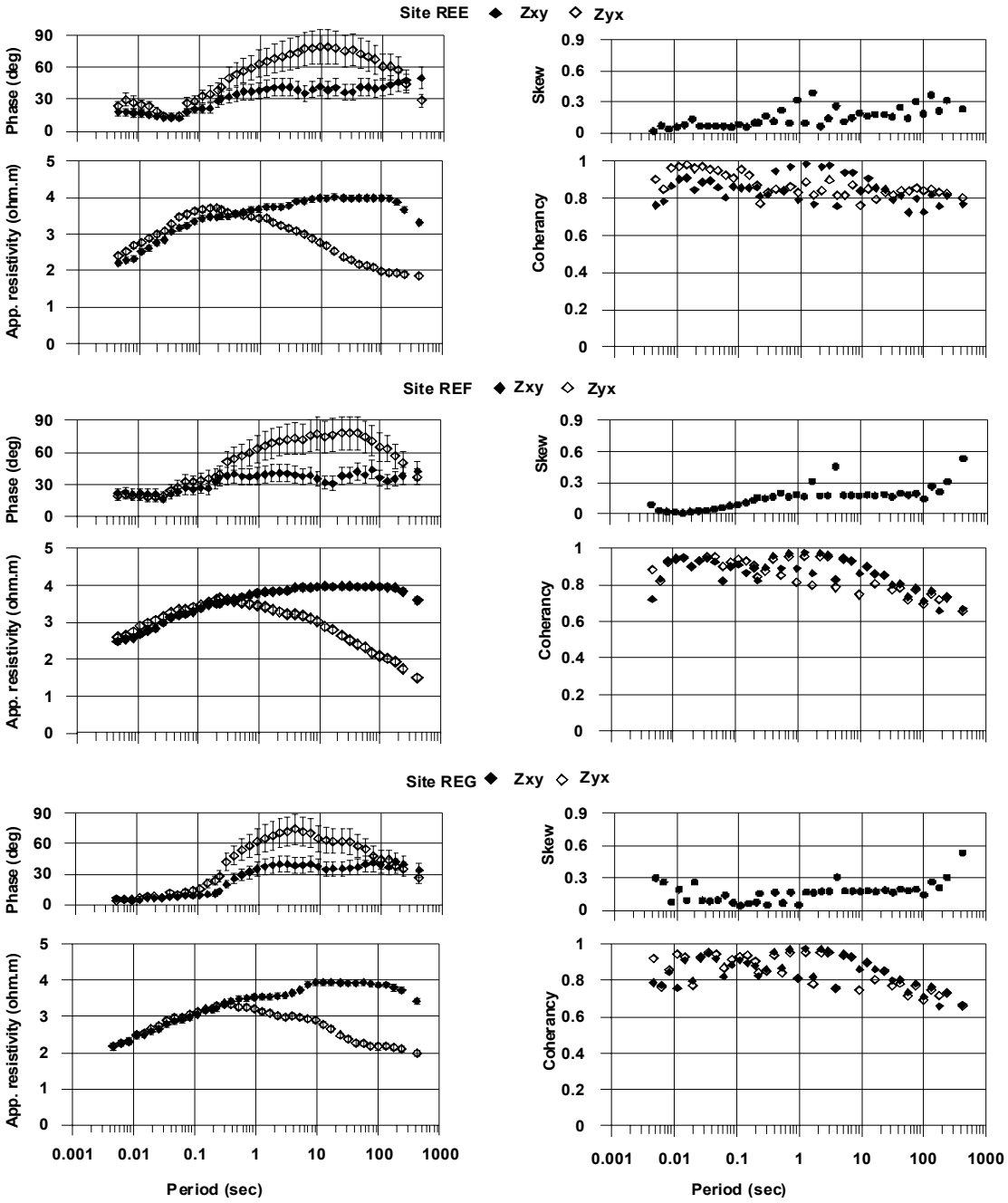

Figure 5.11 (Cont.) MT transfer function (Zxy, Zyx), skew and coherency versus period.

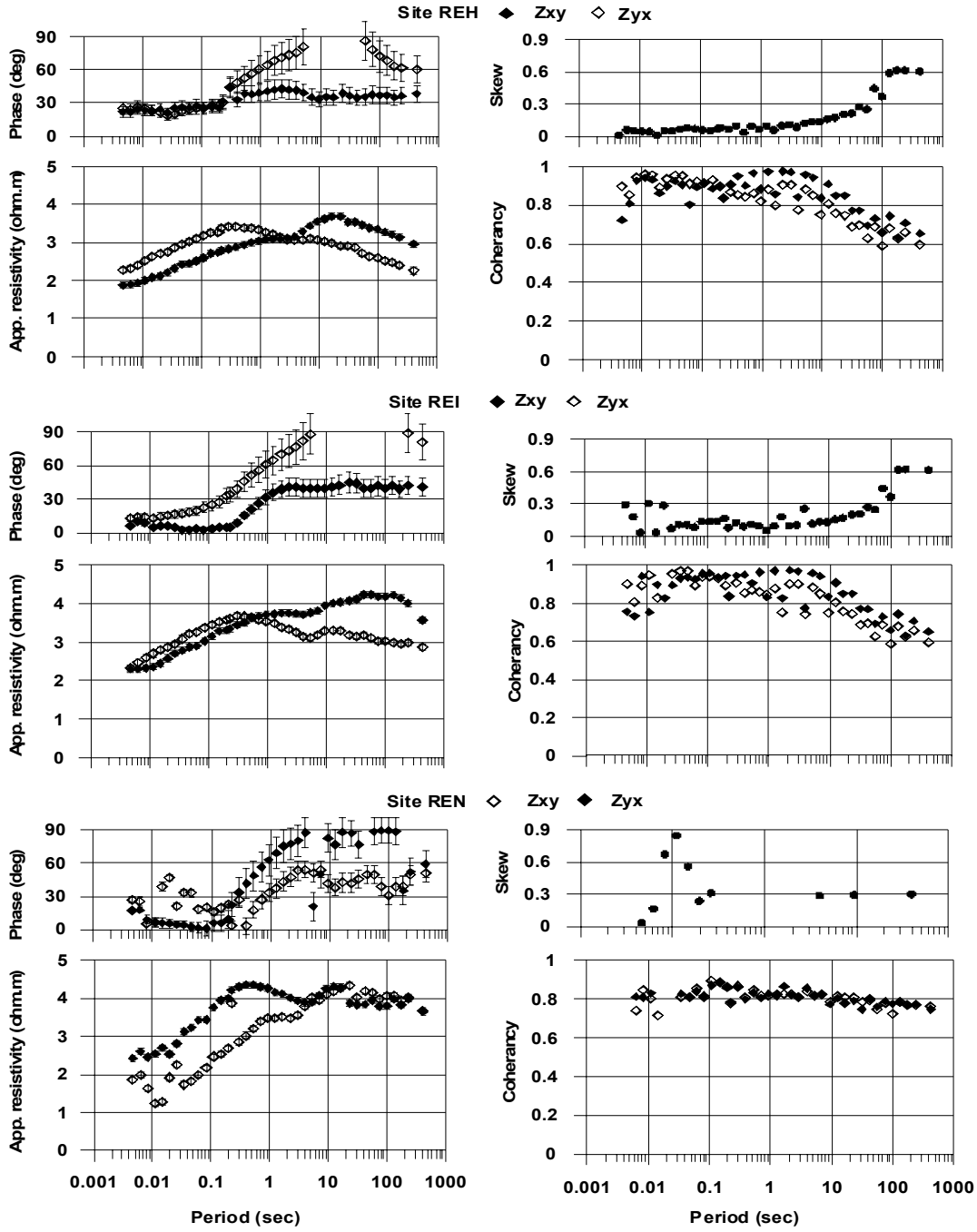

Figure 5.11 (Cont.) MT transfer function (Zxy, Zyx), skew and coherency versus period.

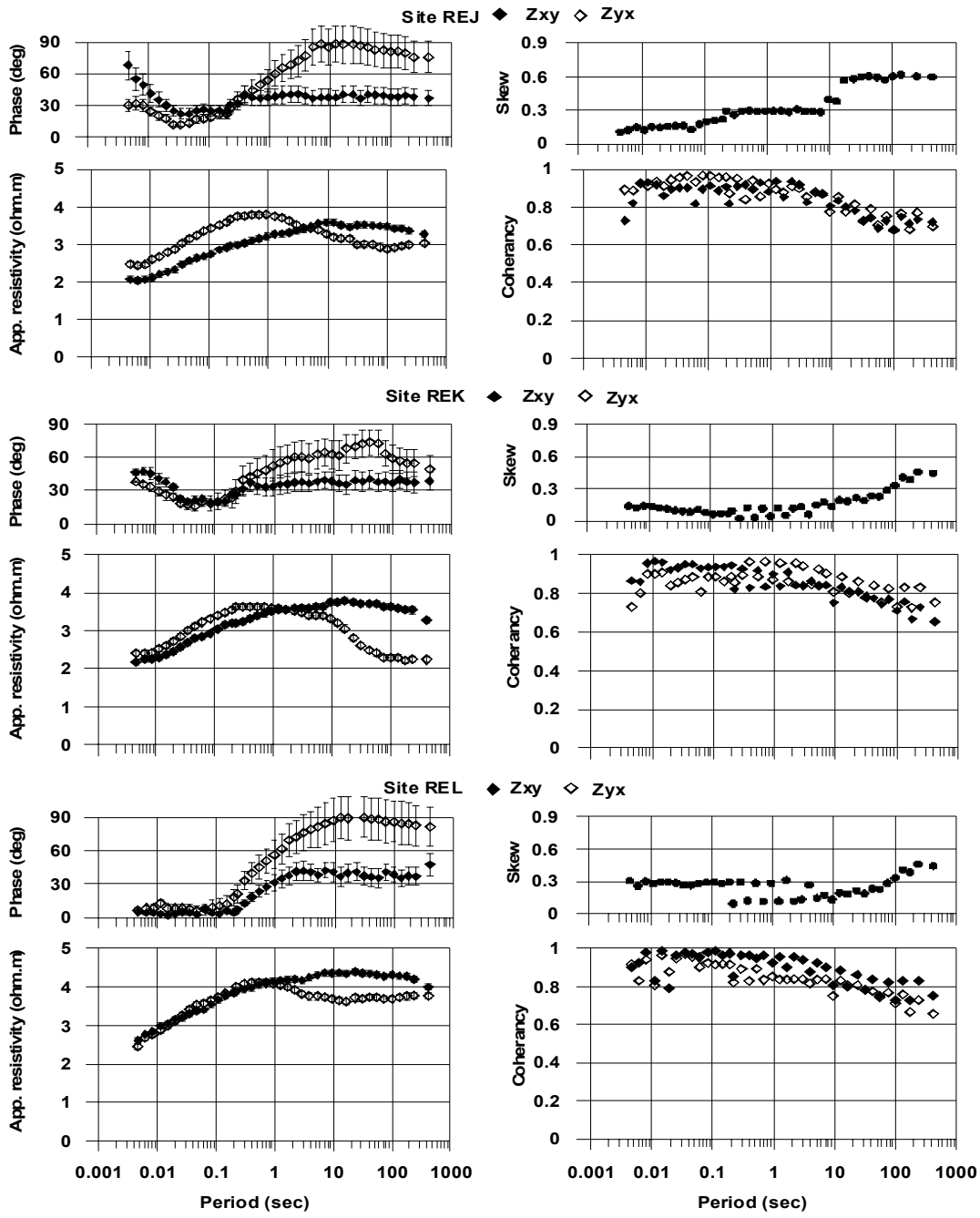

Figure 5.11 (Cont.) MT transfer function (Zxy, Zyx), skew and coherency versus period.

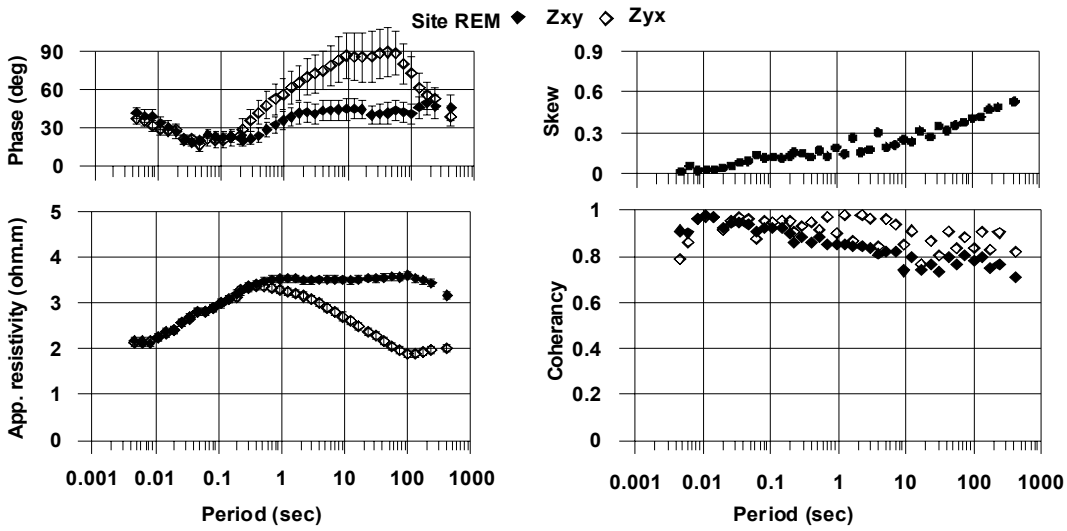

Figure 5.11 (Cont.) MT transfer function (Zxy, Zyx), skew and coherency versus period.

5.8 Data modelling

As usually, our target is to find a 2D model of the geology that can explain the MT and tipper data found at 13 stations. The orientation of the short-period tipper suggests that our profile is crossing two faults; one between RED and REE and a second between REI and REJ. One of them does not appear on the geological map. Two other faults mapped by geologists were not detected, due to insufficient profile coverage. In principle the magnitude of the tipper should not exceed one (the height of the grid in Fig. 5.9a, b), so the values at site REN suggest that something special (a fault?) is located in the immediate vicinity of the site. This anomaly makes the geology to depart strongly from the starting 2D-model hypothesis. For this reason the induction arrows and MT data of this site have not been included in the calculation of the final 2D model. For 2D modelling, we have projected the 13 sites on a profile perpendicular to the adopted strike (trending N40W).

Simultaneous inversion of TE, TM modes and tipper (real induction arrows only) was carried out using REBOCC inversion program (Siripunvaraporn and Egbert 2000). The static shift distortion parameters were set free so that the program could automatically adjust the values. A 3rd strip selection was used (i.e. every 3rd period counts). The results of the inversion are shown in Fig. 5.12a-d. After 12 iterations, the inversion finds a model with R.M.S. misfit of 2.1.

Fig. 5.12a-c compares the pseudo-sections of the apparent resistivity, phase and tipper with the model response. Fig. 5.12b clearly shows that the TM-mode phase cannot be accounted for at periods above 5 seconds.

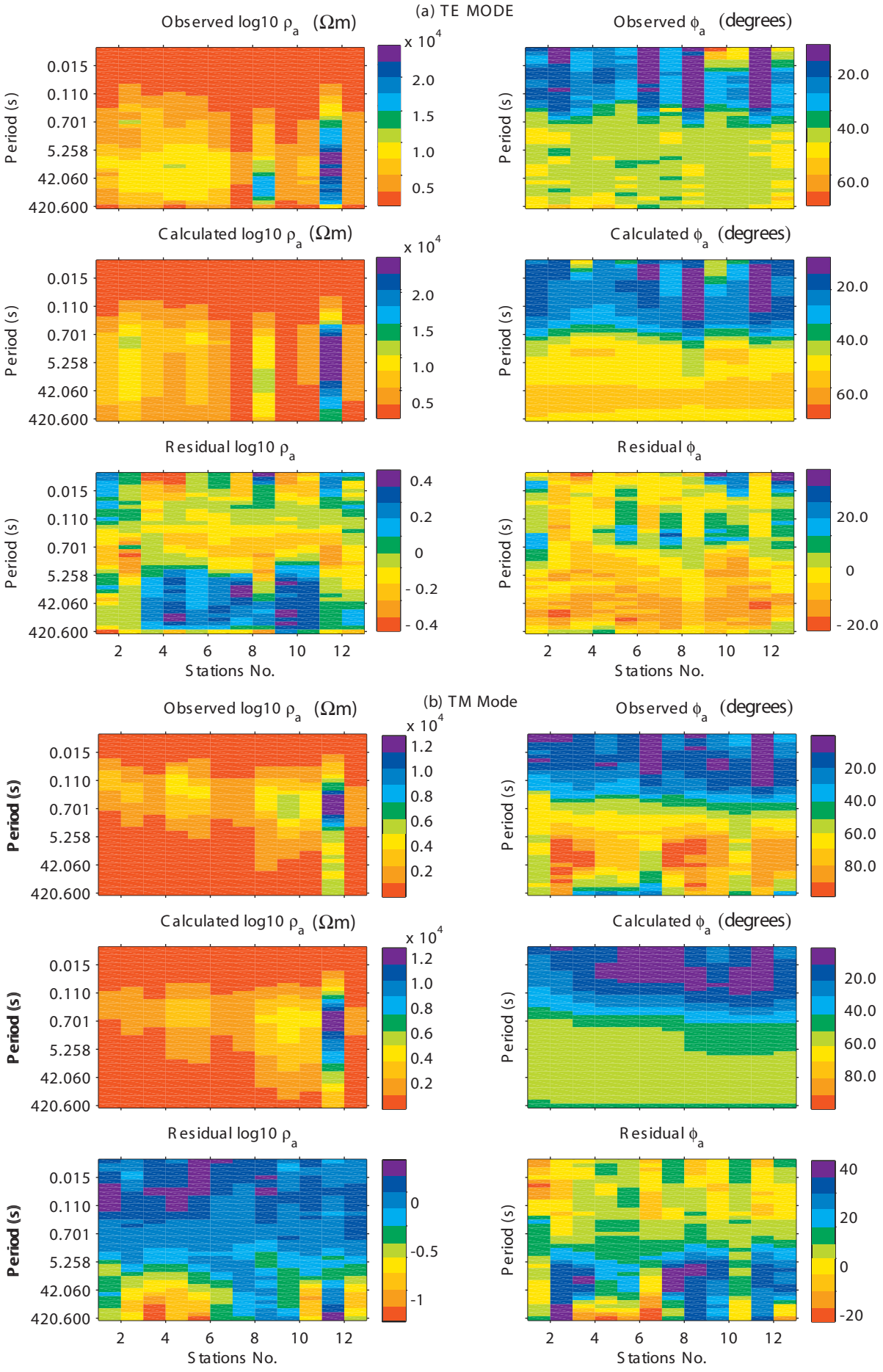

Figure 5.12. Observed and calculated pseudo-sections of MT data along the Remiremont profile.
a. TE mode b. TM mode

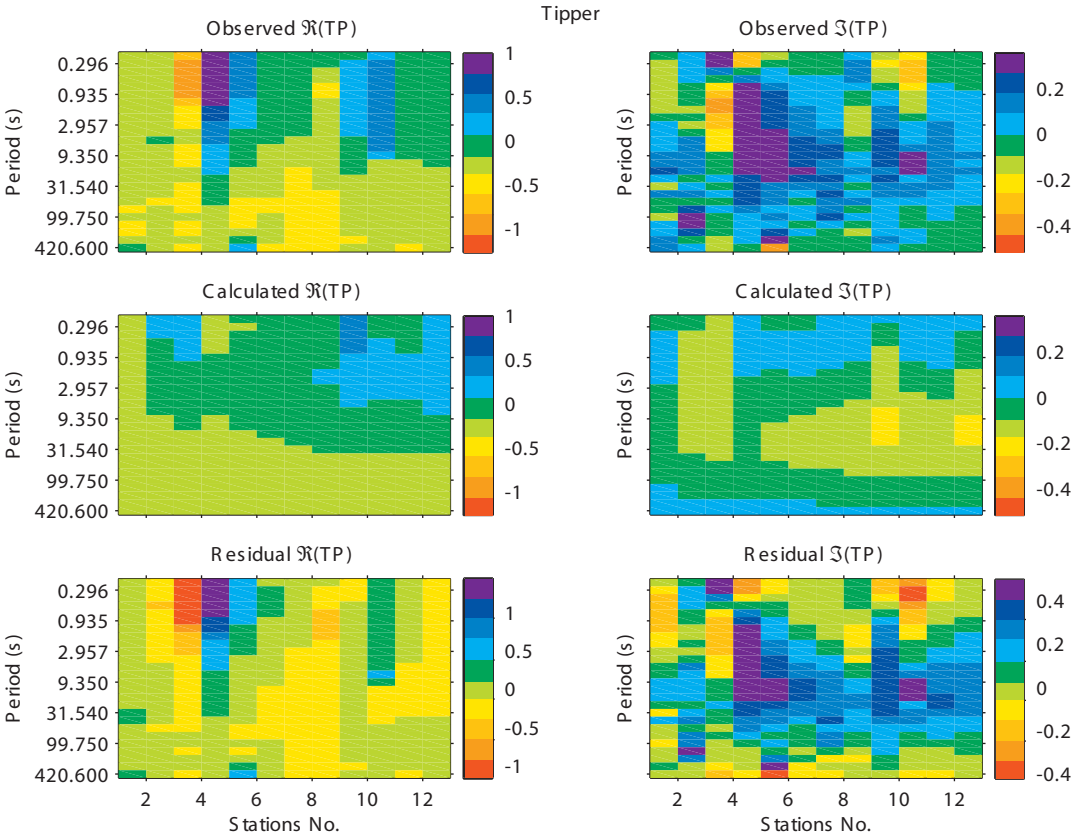

Figure 5.12c. Observed and calculated pseudo-sections of MT data along the Remiremont profile. Tipper.

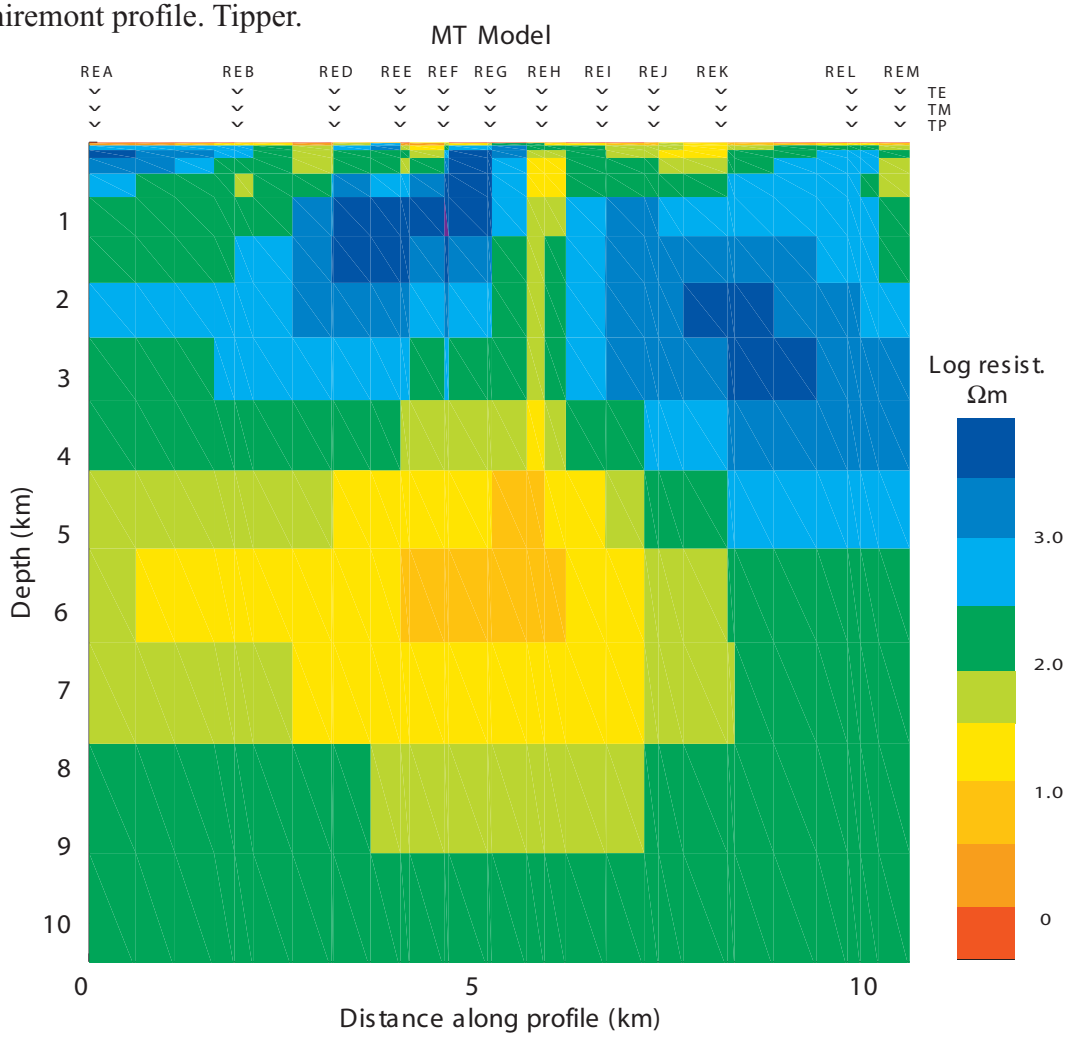

Figure 5.12d. Final result from REBOCC inversion on MT data along the Remiremont profile.

Fig. 5.12c shows a good fit of the real induction arrows except for short periods that are strongly affected by the shallow faults described earlier. This part of the data set was not used in the modelling.

Fig. 5.12d shows the resistivity model. The shallow conductive features can be explained by Quaternary and fractured Mesozoic formations overlying compact Hercynian granite. The deep central conductivity (~5Ωm) is believed to arise from fluids within the fault zone and the high geothermal anomalies of the lower crust/upper mantle (hydrothermal circulation of water at greater depth (10 km).

The 2D model is shown only for the top 10 km. Good-conductive material is located in the depth between 4 and 8 km in an otherwise high resistive medium (Hercynian granite). Comparing this resistivity model with the earthquake distribution of the area (Fig. 5.5), it seems reasonable to interpret it by the presence of some crustal fluids that, in turn, could be involved in the triggering of the seismicity. The resistivity values range between 5-100 Ωm along the anomalous zone. Note that the resistivity values are lower in the middle part (main fault) of the profile, around the seismic area rather than the other faults. It extends to a depth of about 5 km within the Hercynian Vosges basement. The increased resistivity below fractured crystalline basement does not imply the absence of fluids, but probably increasing confining pressure reducing the porosity of the rock and pathways available for electric current flow (Unsworth et al. 2000). The fitting curves of the observed and calculated 2D inversion (REBOCC) are shown in Figs. 5.13a-c. The subsurface model calculated by REBOCC will be used as input to the SPW program developed for modelling the particular behaviour of the short-period tipper.

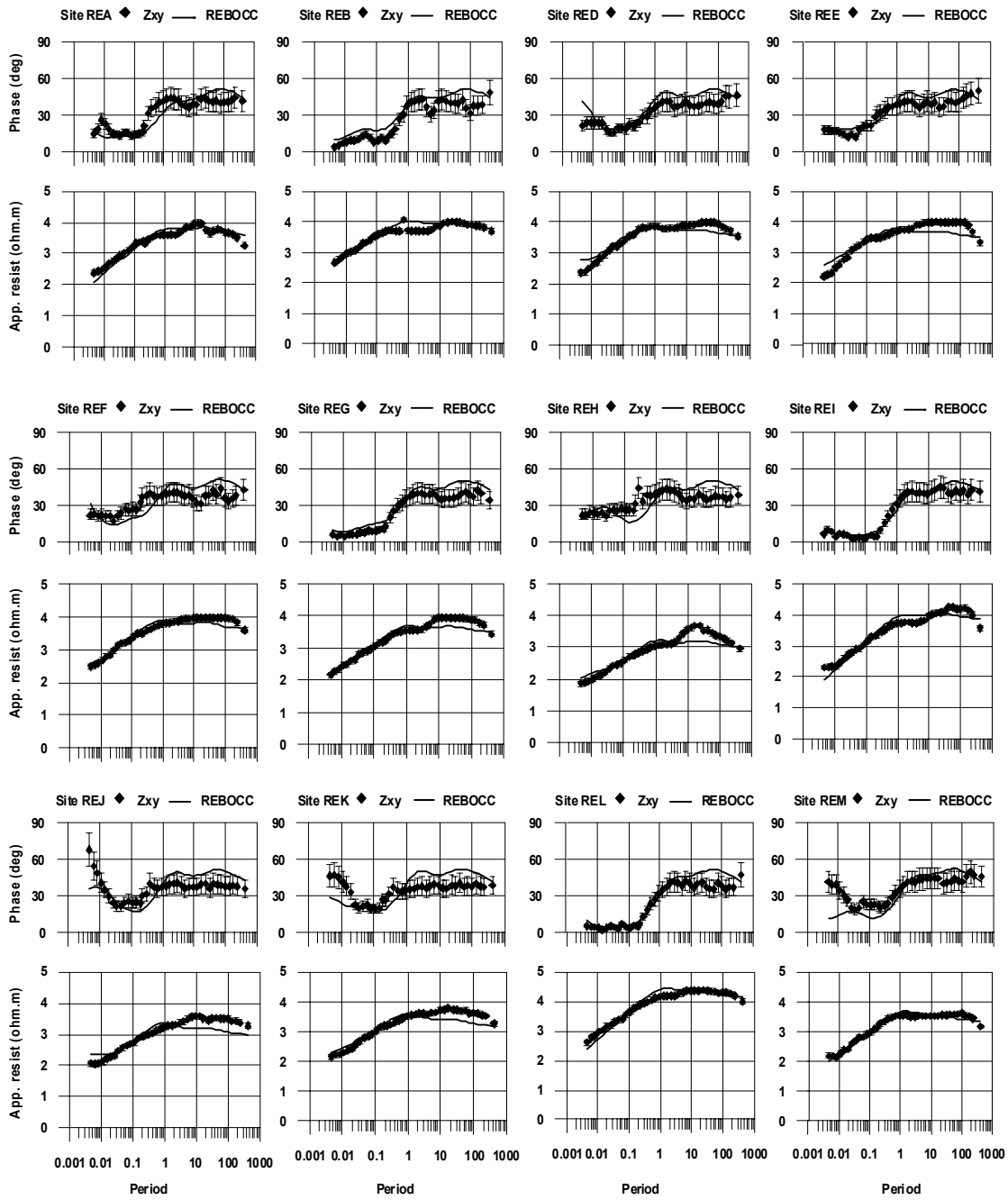

Figure 5.13a. Fit (solid line) of the model to the apparent resistivity and phase (TE mode) of the Remiremont 2D model.

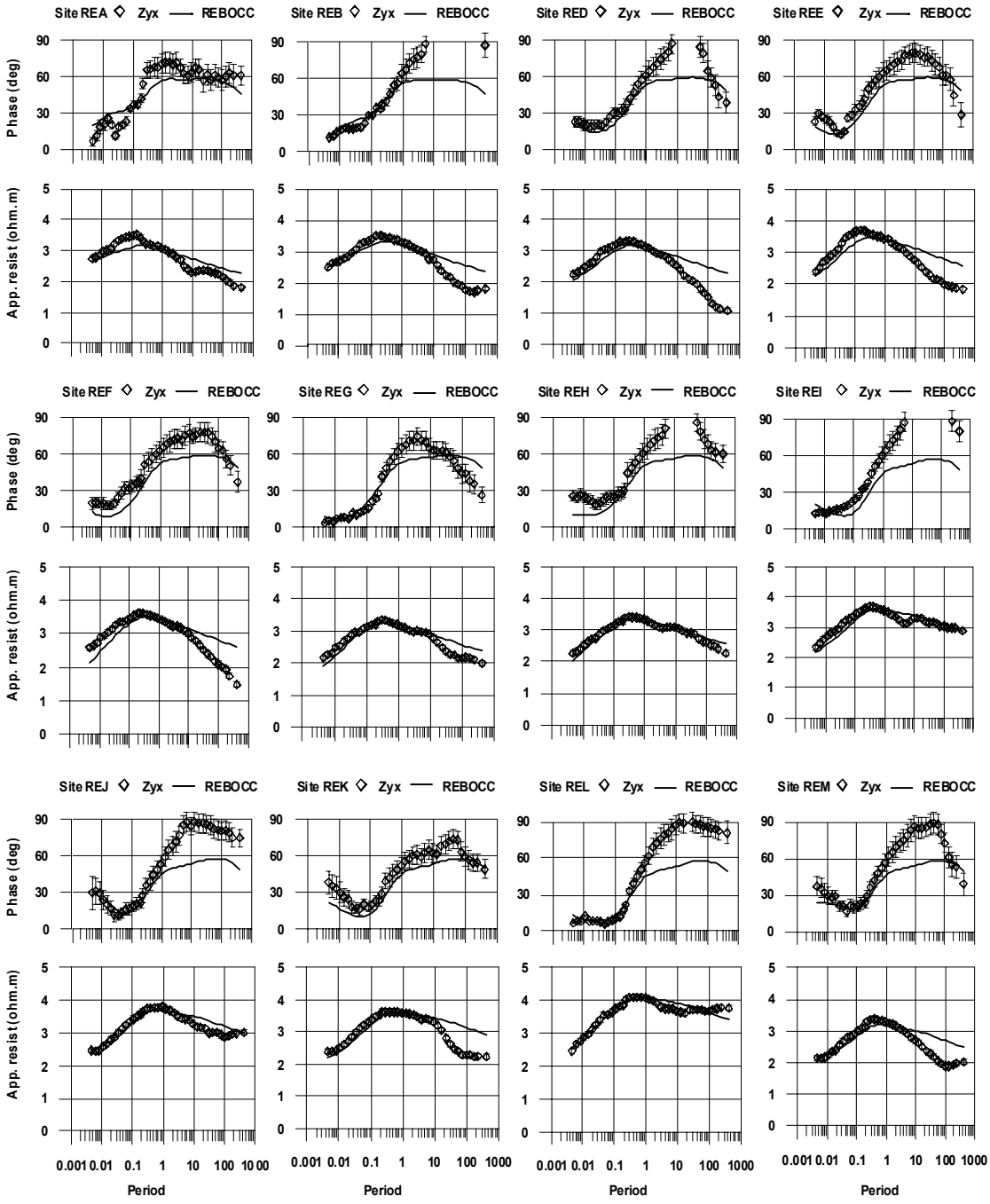

Figure 5.13b. Fit (solid line) of the model to the apparent resistivity and phase (TM mode) of the Remiremont 2D model.

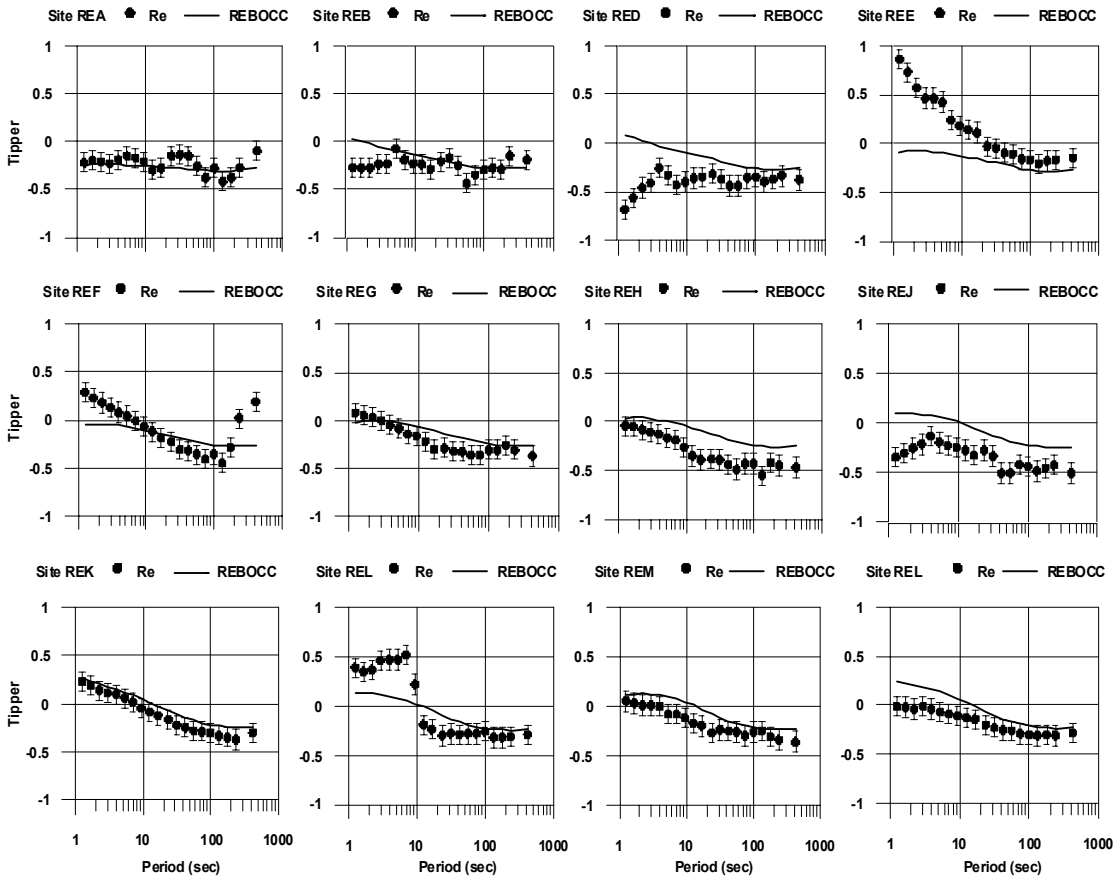

Figure 5.13c. Fit of the model to the real induction arrow of the Remiremont 2D model. Note the high misfit at site REE due to a surficial conductive feature.

Our algorithm SPW is based on a finite element program that computes magnetotelluric responses (it is assumed that TE and TM may be treated independently) of a 2D earth resistivity structure (Wannamaker et al. 1985). To find the best model, it makes use of the MINDEF subroutine (Beiner 1970) for minimisation of the misfit between measured data and model response. The model parameters are automatically fitted by the program. Those parameters are: horizontal fault location, width and resistivity. To keep the model as simple as possible the dip is set vertically. Because it was obvious that the H_z data showed mainly two conducting anomalies, we looked for a model with two separated faults simultaneously.

Figures 5.14a-c show the response of the real tipper at four periods (0.225, 0.525, 1.24 and 2.92 s) from which the subsurface model was calculated. In general the model response of the real component can reproduce the measurement but the sites REK, REL and REM do not fit well at all periods. This is interpreted as the result of the local interplay of crosscutting faults. Two shallow dike-like strong conductors are found (Fig. 5.14c), one of them coinciding with a known fault (Fig. 5.8). Faults located with the short-period tipper seem to extend down to 250-1000 m depth. The resolving power of the method is not able to follow them at greater depth.

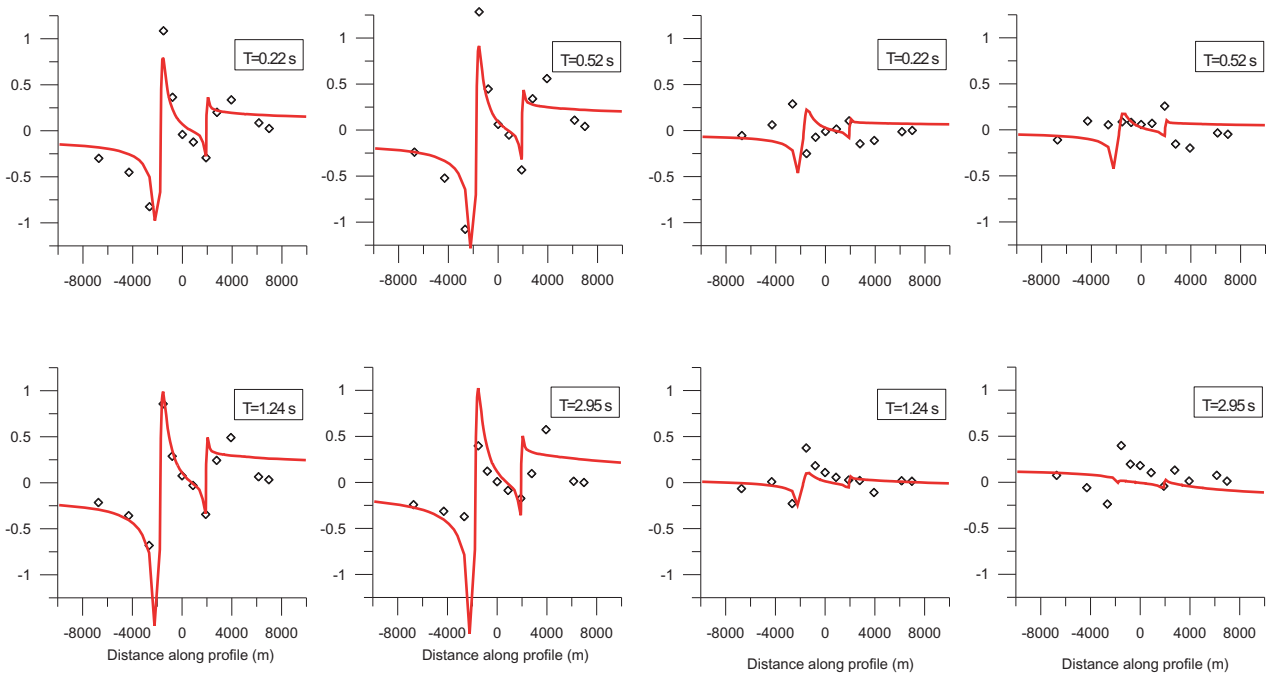

Figure 5.14. Measured arrows versus profile distance and 2D model response at four periods in the short-period end. Model obtained by automatically fitting location, size and resistivity of two vertical rectangular prisms. a) real arrows b) imaginary arrows

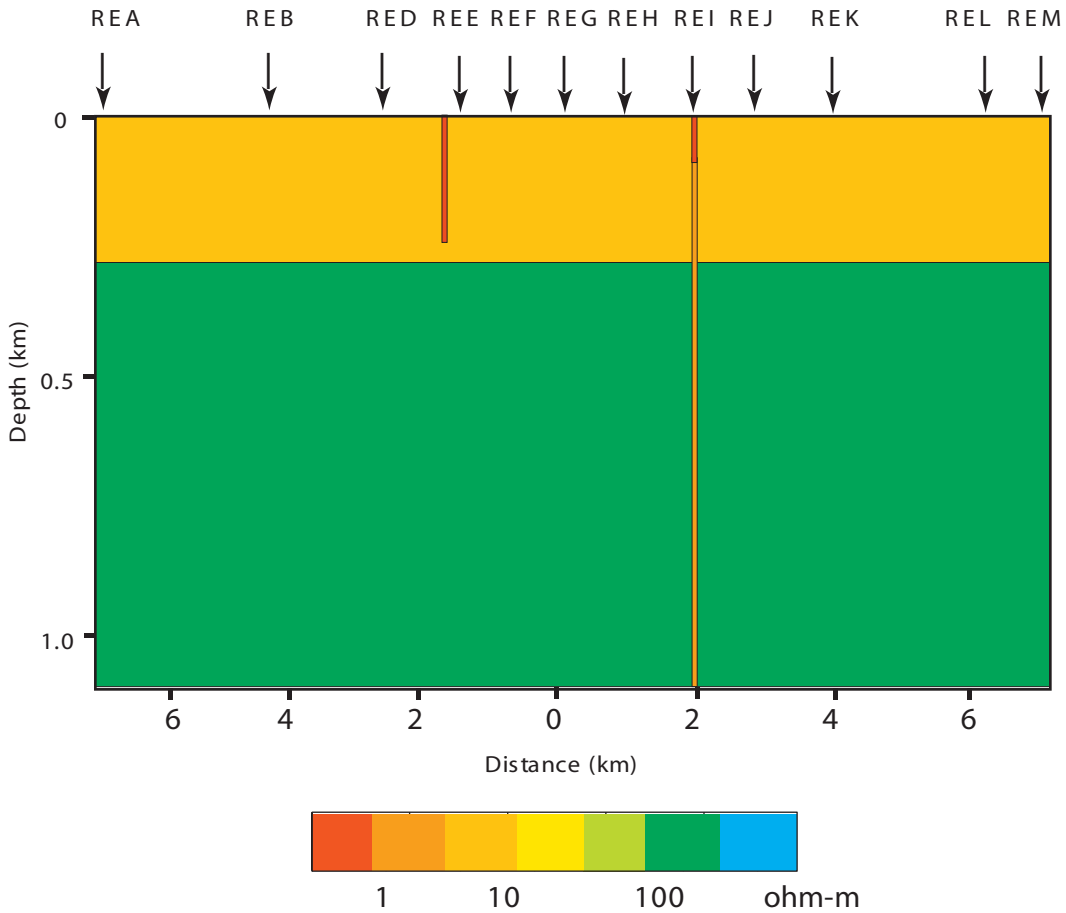

Figure 5.14c. Subsurface model obtained solely with the induction arrows showing two-high conducting features, one of them (at site REI) coinciding with a documented fault. The 1D structure is inherited from the previous 2D modelling.

5.9 Discussion

Seismic activity is found in the Remiremont area between 1984 and 1985. Recent strong event of magnitude M = 5.5 occurred 10 km north of our profile on February 22, 2003. It means that the southern Vosges Massif stays tectonically active. Audin et al. (2002) suggested that the seismic activity reflects rupture of asperities driven by fluid-flow in a high permeability zone, and the fluid circulation could occur in the fractured Hercynian basement.

Figure 5.14c shows the model of the subsurface that was calculated from the real and imaginary induction arrows. The two faults are filled with substances of very low resistivity between 0.5 and 3.2 Ωm, as might be expected for water containing a high concentration of dissolved salt. In Vosges, the upper Triassic layers contain salt deposits, but these layers have been eroded away of the area. Furthermore, salt concentration in the water of the local springs is relatively low, suggesting that its source be located in the crystalline rocks.

Alternative explanation could be clay material in the fault, or deposited minerals. If hot water percolated up through the cracks of the faults, minerals dissolved in the fluid could have crystallised along the walls of the faults. Also metal-sulphide deposits conduct current very well and might lead to the low conductivity values in the fault plane.

In their deeper range, our MT measurements indicate the presence of conducting material in a location coinciding with a seismic cluster that develops along 40 km to the north (1984-1985). The conducting fault can be found between sites REG, REH and REI. It is noted that the resistivity values are lower in the central part of the profile around the seismic strip.

6. Similarities with other faults

To study the connection of the Kalabsha and Remiremont seismicity to the corresponding 2D resistivity structure, MT measurements were carried out across Kalabsha and Remiremont faults. The results support the idea of the influence of fluid-bearing conducting faults in the tectonically active regions to the earthquake mechanism (Johnson and McEvilly 1995; Audin et al. 2002). Supposing that fluids deposited minerals in the conductive fractures decreasing the resistivity, the high seismicity in the region can be explained by the presence of these fluids. They play a role in the release of stress accumulation in the earthquake mechanism (dilatency).

Lake Aswan area:

Fig. 6.1a-b show the final models of the Wadi Kalabsha and Remiremont areas. The two models exhibit several distinctive features, starting with Kalabsha 2D resistivity model as follows:

- The Kalabsha fault (Fig. 6.1a) is characterised by low resistivities (10-100 Ωm) only at shallow depth (5 km), reflecting a thin sedimentary cover and a possible deep-reaching weathering of basement layers.
- The distribution of earthquakes around the Kalabsha fault is found to lie on a single dipping plane, with geometrical parameters automatically determined by our minimising method.
- It is clear that the seismic activity is controlled by the Kalabsha fault. The active and deeper part (cluster K1, see figure 3.4) is seasonally covered by water.
- The very high resistivity on both sides (1,000-3,000 Ωm) below 4 km which are likely granitic basement rocks (associated with granitic outcrops in the eastern part of the lake, see figure 2.4), could be explained by increasing confining pressures and reduced porosity of the granite rock.
- The high electrical conductance (1-10 S) found below 20 km, can be explained with fluids, partial melting, aqueous fluids or a combination of partial melt and aqueous fluids (Li et al. 2003).

Remiremont area:

Fig. 6.1b shows the resistivity model from an inversion of the TE, TM and tipper in the Remiremont area:

- The most prominent structure is the dyke-like vertical conductor below REH site. This high conductor zone (HCZ) goes much deeper than 5 km. It may be explained by the influence of hydraulic routing for deep fluids.
- Additionally, high conductivities (below 20 km) could reflect deeper structures below the area of the hydrothermal anomaly within the lower crust/upper mantle (Werner and Parini 1980).

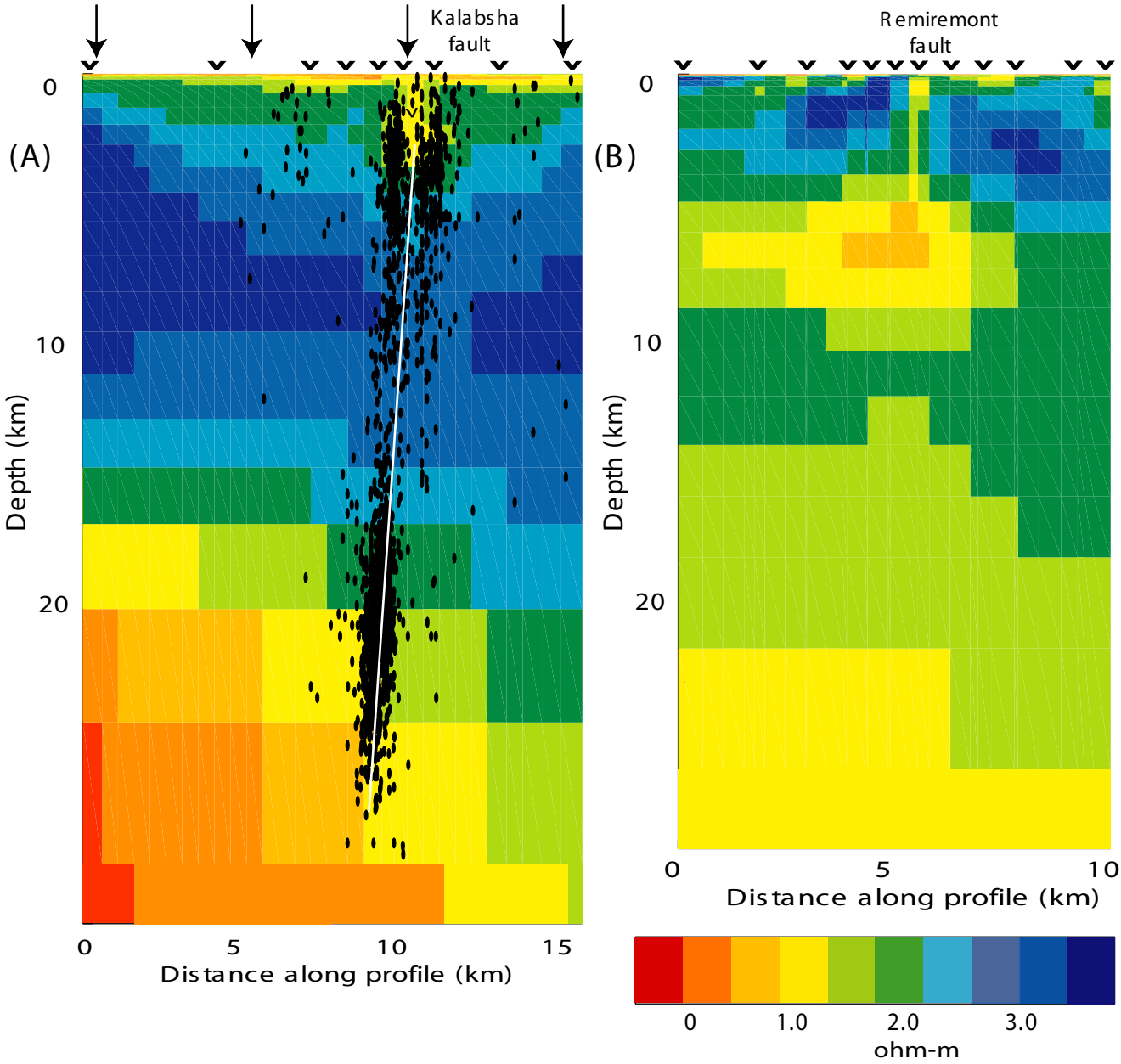

Figure 6.1a-b. 2D model of the electrical resistivity along (a) Kalabsha and (b) Remiremont faults. The vertical arrows indicate pore fluid pressure increase due to water level loading. Location of MT sites marked on the surface. Fig. 6a shows foci of earthquakes and best-fitting plane.

- If we compare this model with the seismic activity of the area (figure 5.7), most of the earthquakes occurring between latitudes (47.9-48.1) and longitudes (6.4-6.6) can be projected in the middle of our MT profile.
- Induction vectors indicate two documented conductive structures at site RED/REE and REI and REJ, but fail to detect other two faults in the geological map (MT site density too low).
- The source of the HCZ (Fig. 5-14c) could be in Hercynian granite rocks with cracks filled with good-conducting substances (brines, graphite, sulphides or salt).

San Andreas fault (SAF):

Imaging the internal structure of the active SAF fault has been done in recent years (Mackie et al. 1997; Unsworth et al. 1999 2000; Bedrosian et al. 2002). MT profiles have crossed the SAF at different locations. High-resolution images of electrical conductivity variations within and near the fault zone to a depth of about 4-6 km are estimated (Fig. 6.2 and 6.3). They suggest a higher porosity and fluid content in the seismically active region of SAF. Obviously, the fault zone properties (the fluid distribution) are controlling the seismicity. Both shallow and deeper events (M ≈ 6) are fluid-driven. At the depth of the characteristic M ≈ 6 events a zone of low P-wave velocity and high seismic attenuation (Vp/Vs) is consistent with the presence of fluid. The source of fluids within fault-zones remains uncertain until now. The fault creep (associated with microseismicity) on the SAF is controlled by the availability of fluids coming from metamorphic reactions within the Franciscan formation (Irwin and Barnes 1975). Geochemical studies of fluids from spring and wells along the SAF suggest a meteoric origin (Kharaka et al. 1999) and maximum circulation depth of 6 km. Another possibility is the presence of clays along the fault zone (Bedrosian et al.2002).

According to Unsworth et al. (1997) Archie's law can be used to relate the fluid conductivity (a function of salinity), porosity of a fluid saturated rock, and the expected bulk resistivity:

$$\rho_r = \rho_f \phi^{-m} \tag{41}$$

where ρ_r is the effective resistivity of the rock, ρ_f is the resistivity of pore fluid, ϕ is the porosity, and m is a constant between 1 and 2. To obtain ρ_r=3 Ωm, typical of the fault zone at 3 km depth, would required a porosity range 8.6-30 %, with m=1 and 2 respectively.

If we compare our results with SAF work as mentioned above, the Kalabsha and Remiremont areas are highly fractured and controlled by active tectonic faults system (El-Shazly 1977 and Ziegler 1992). Low velocities were found at shallow depths in both regions from previous work (Awad and Mizoue 1995b and Sitter 1933). These observations are significant since low velocities may indicate the presence of fluids associated with the mechanics of earthquake rupture (Unsworth et al. 2000).

Ziegler (1992) mentioned that the uplift of the southern Rhine graben Vosges-Black Forest rift dome

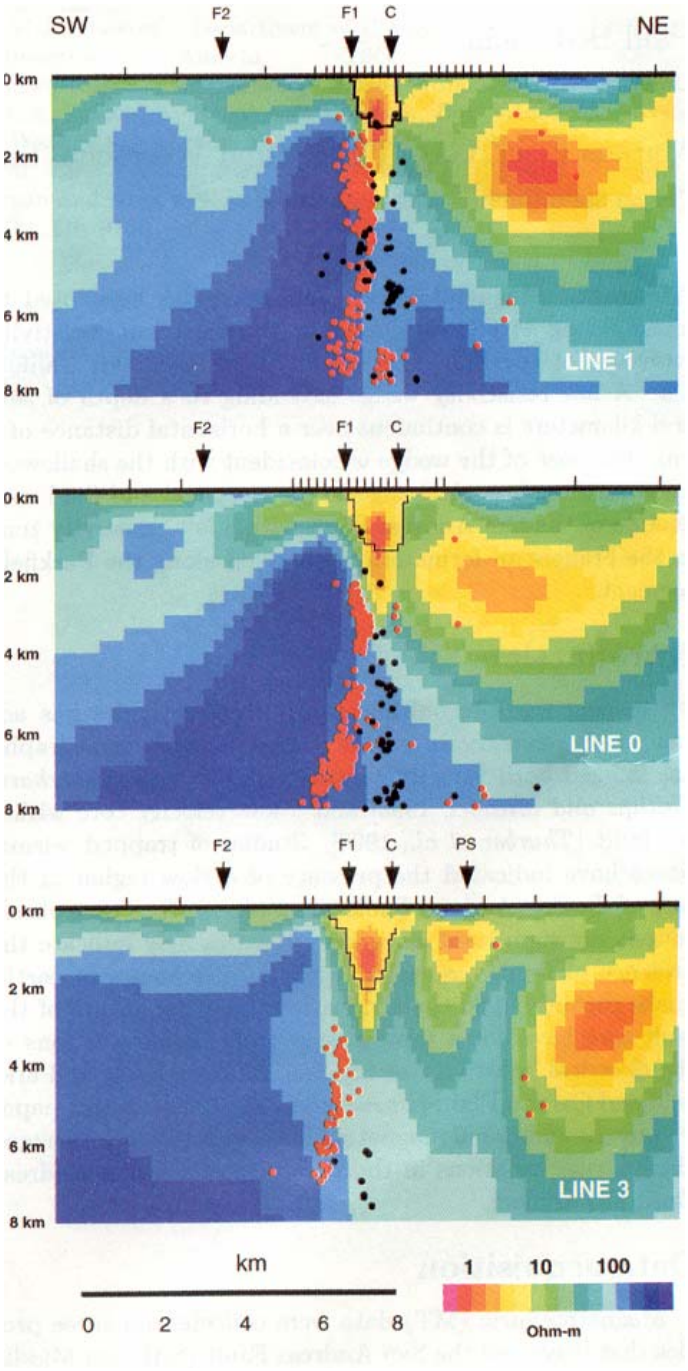

Figure 6.2 Electrical resistivity models for three Middle Mountains profiles within the deep fault zone conductor. Earthquake hypocenters within 2 km of each profile. The black line indicates the 6 Ωm contour for models with a shallow fault zone conductor (Unsworth et al. 2000).

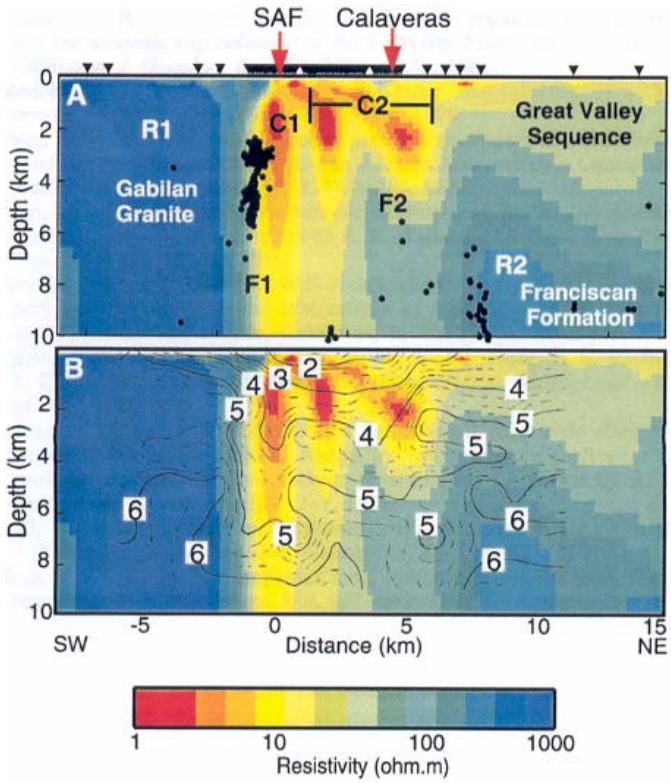

Figure 6.3. (a) Electrical resistivity model along the northern profile to the southern part of Hollister, California. Earthquake hypocenters within 2km of each profile as black circles. (b) same model overlain by P-wave velocity contours (Bedrosian et al. 2002).

started during the late middle Miocene, as evidenced by the deposition of the Nagelfluh in the Jura Mountains; these conglomerates are the erosion of the former Mesozoic cover of the Vosges and Black Forest. The Vosges and Black Forest domes are probably underlain by asthenoliths emplaced at the lower crust/upper mantle boundary.

Adam (2001) suggested that low viscosity graphite and/or fluid spread across the tectonic zones (conducting dikes), influencing the stress accumulation of earthquakes and providing higher attenuation of seismic waves. Earthquake mechanism starts at a lower level of stress accumulation (slipping, creeping), in the low viscosity graphite and/or fluid. Therefore these conditions can set an upper limit to earthquake magnitudes.

As mentioned above, high electrical conductivities are found in active tectonic regions due to water containing high concentration of salt, or high temperature (hydrothermal circulation of water at greater depth), or ore materials (graphite and sulphides). Furthermore, permeability and high porosity (weathered layers and fractured basement) are required.

7. Summary and conclusions

With our work, MT measurements were carried out in Egypt for the second time (Brasse 1990) and first time in Wadi Kalabsha area after the occurrence of the November 14, 1981 earthquake. The magnitude of this earthquake was 5.4, occurring not far from the High Dam (about 60 km). The High Dam provides Egypt with hydroelectric power, water supply and protects the country from high floods. Lake Aswan now extends over 350 km along the river Nile in Egypt and 150 km in Sudan territory. The main target of our field work was to detect electrical resistivity anomalies associated with earthquake activity and water loading as well as particular stress conditions.

A summary of the MT data in active tectonically areas (Wadi Kalabsha and Remiremont) are presented to better understand the connection between low resistivity anomalies and the earthquake occurrence and their role in earthquake mechanism. The conclusions of the study are given in the form of seismicity and MT results.

Seismicity results in Wadi Kalabsha

- We analysed the Aswan seismicity pattern in the 1982-2001 period to understand how water level loading drives the moderate ($M < 5.0$) seismicity in this period.
- From the distribution of earthquakes, it was found that the seismicity (1982-2001) is concentrated at five cluster zones. The K1 cluster (Fig. 3-5) is the active and deeper (>15 km) zone located on Kalabsha fault. The other zones are characterised by shallow seismicity (< 15 km) at the intersection of Kalabsha fault with NS faults.
- The shallow and deep seismic zones behave differently over time.
- We applied statistical techniques to the Aswan catalogue (4514 events) to evaluate the seismicity patterns (average spatial behaviour, fractal spatial clustering and b-value change with time) and compare them with water level in different time windows.
- The deep-earthquake rate decreased with time and remained at a constant or increasing depth and displays a b-value lower than the shallow events.
- The variations in b-value are related to differences in stress, pore pressure and material heterogeneity. We suggest that at shallow depth conditions, more heterogeneous material and lower lithospheric stress prevail. The reverse prevails at greater depth.
- The shallow events migrate toward surface with constant rate
- The correlation between seismicity and water level change is not fully consistent. However, we were able to observe a phase shift (a delay of time) between the two time series. The delays are two and four months for shallow and deep seismicity respectively.
- In the frequency domain, well-resolved peaks of water level and seismicity are shown at 1 $year^{-1}$. This is a quite convincing proof of causality effect.
- Decrease in D-values for shallow and deep events indicates an increase of clustering, i.e. the earthquake occurs in concentrated areas only.

- Another interesting correlation between conductivity and seismic activity: the orientation of the plane that contains the earthquake foci is in good agreement with the MT strike, N60^{o}E.
- Our results suggested that the Aswan seismicity emerges both from water level fluctuations and the interplay between induced earthquake through numerous aftershock sequences.

The seismicity of Remiremont area

- The historical activity within Remiremont area is long (e.g. 1682 to date).
- The area becomes particularly tectonically interesting after the February 22, 2003 earthquake (M = 5.5) occurred 10 km north from our MT profile.
- The seismicity in Remiremont area is characterised by shallow activity (depth<15 km).
- From the distribution of magnitude with time, we saw that the magnitude in the area is low (M < 4.0) except for two events (1984 and 2003).
- Migration patterns of seismicity in the area proposed that intrusions of fluids might be at the origin of the earthquakes (Audin et al. 2002).

MT results in Wadi Kalabsha

On the basis of the MT profile of nine stations, the main electrical features of the area can be summarised as following:

- The high resistivity consists of two main zones. Between them, a conducting fault plane of at least 5 km depth takes place in the tectonically weak zone (fractured fault/strike slip).
- The source of the locally-enhanced conductivity could be fluid (meteoric or infiltrated water and clay) having penetrated along fractured basement rocks and accumulated in the fault zone and forming low resistivity anomaly.
- Comparison of our results with seismic tomography studies shows that this zone is highly fractured and bounded by the Kalabsha fault. This is consistent with a zone of low seismic velocities.

MT results in Remiremont area

MT soundings offer opportunity to detect crustal fluids along Remiremont faults due to their low resistivity. Seismic events having magnitude less than 4.8 are found to align along a 40 km-long fault zone. The aims of the measurements are to determine the precise location of the active faults and to support idea of the influence of the conducting fluids in the Remiremont area to the earthquake mechanism. The results can be described as follows:

- The orientation of the tipper at short periods (induction arrows) suggested that our profile crossed two faults in the subsurface, one of which is also indicated on the geologic map of the area.
- The two faults are filled with substances of very low resistivity (~ 1-3 Ωm).

- At a depth in agreement with the seismicity, the fault zone conductor is clearly observed (> 5 km), although the change of azimuth compared with the subsurface faults indicates that the fault is perpendicular (trending N40°W).

7.1 Recommendations

According to our results during two weeks of measurements in Aswan and southern Vosges, it is recommended:

- To extend the magnetotelluric measurements in Vosges area, especially after the February 22, 2003 M = 5.5 earthquake and using various MT profiles for detailed investigation of the resistivity anomalies associated with earthquakes occurrence.
- The magnetotelluric measurements must be continued in the Aswan region and repeated to estimate 3D resistivity structure of the area and influence of perpendicular faults.
- Establish permanent MT stations around Kalabsha fault to better understand earthquake mechanism and possible prediction parameters, and the seasonal evolution of the conductivity.
- The study by geophysical methods (including seismic refraction and reflection and gravity) could contribute to the better understanding of the earthquake occurrence.

8. References

1. AbdelRahman, E.M., A. Tealeb and H.A. Ahmed, *Gravity Map of Kalabsha area, northwest of Aswan lake, and its structural surface.* J. Geodynamics, 1991. **14**: p. 125-135.
2. Abhorner, L., *Present day stress field and seismotectonic block movements along major fault zones in cental Europe.* Tectonophysics, 1975. **29**: p. 233-249.
3. Adam, A., *Relation of the graphite and fluid bearing conducting dikes to the tectonics and seismicity (Review on the Transdanubian crustal conductivity anomaly).* Earth Plantes Space, 2001. **53**: p. 903-918.
4. Aki, K., *Maximum likelihood estimate of b-value in the formula log N = a-bm, and its confidence limits.* Bull. Earthquake Res. Inst., 1965. **43**: p. 237-239.
5. Ambraseys, N.N., C.P. Melville and R.D. Adam, *The seismicity of Egypt, Arabia and the Red Sea: A historical review.* Cambridge University Press, 1994.
6. Amitrano, D., *The brittle-ductile transition in rock experiment.* J. Geophys. Res. in press, 2003.
7. Amitrano, D., J.R. Grasso and D. Hantz, *From diffuse to localized damage through elastic interaction.* Geophys. Res. Lett, 1999. **26**: p. 2109-2112.
8. Andrieux, P., G. Clerc and P. Tort, *Capteur magnétometrique triaxial pour la prospection magnétotellurique artificielle entre 4Hz et 4 kHz.* Physique Appliquée, 1974. **9**: p. 183-190.
9. Arora, B.R. and A. Adam, *Anomalous directional behaviour of induction arrows above elongated conductive structures and its possible causes.* Phys. Earth Planet. Inter., 1992. **74**: p. 183-190.
10. Audin, L., J. Avouac, M. Flouzat and J. Platet, *Fluid-driven seismicity in a stable tectonic context: The Remiremont fault zone, Vosges, France.* Geophys. Res. Lett, 2002. **29**(6).
11. Awad, H. and M. Mizoue, *Earthquake activity in the Aswan region, Egypt.* PAGEOPH, 1995. **145**: p. 69-86.
12. Awad, H. and M. Mizoue, *Tomography inversion for the three-dimensional seismic velocity structure of the Aswan region, Egypt.* PAGEOPH, 1995. **145**: p. 193-208.
13. Awad, H. and A. Tealeb, *Attenuation of intensity in the northern part of Egypt associated with May 28, 1998 Mediterranean Earthquake.* Acta Geophysica Polonica, 2000. **XLVIII**(No. 1).
14. Bahr, K., *Interpretation of the magnetotelluric impedance tensor: regional and local telluric distortion.* J. Geophys. Int., 1988. **62**: p. 119-127.

15. Bailey, R., R. Edwards, G. Garland, R. Kurtz and D. Pitcher, *Electrical conductivity studies over a tectonically active area in eastern Canada.* J. Geomagn. Geoelect, 1974. **26**: p. 125-146.
16. Beamish, D. and J.M. Travassos, *A study of static shift removal from magnetotelluric data.* J. appl. Geophys, 1992. **29**: p. 1-21.
17. Beavan, J.K., S. Evans, S. Mousa and D. Simpson, *Estimating aquifer parameters from analysis of forced fluctuations in well level: An example from the Nubian formation near Aswan, Egypt. 2. poroelastic properties.* J. Geophys. Res, 1991. **96**(B7): p. 12139-12160.
18. Bedrosian, P.A., M.J. Unsworth and G. Egbert, *Magnetotelluric imaging of the creeping segment of the San Andreas Fault near Hollister.* Geophys. Res. Lett, 2002. **29**(No. 0, 1029).
19. Beiner, J., *Fortran routine MINDEF for function minimization.* Institut de Physique, Université de Neuchâtel, Switzerland., 1970.
20. Bell, M.L. and A. Nur, *Strength changes due to reservoir-induced pore pressure and application to Lake Oroville.* J. Geophys. Res, 1978. **83**: p. 4469-4483.
21. Bendat, J.S. and A.G. Piersol, *Random data: Analysis and measurements procedures*. 1986: Wiley. 266.
22. Ben-Menahem, A. and E. Aboodi, *Tectonic patterns in the northern Red Sea region.* J. Geophys. Res, 1971. **76**(11): p. 2674-2689.
23. Berdichevskiy, M.N. and Kulikov, V.A., 1995. *Sensitivity of deep magnetotelluric sounding in the presence of fluid-saturated fractures.* Phys. Solid Earth. Russian edition, 30(6): 511-521.
24. Berktold, A., H. Dittus and U. Teufel, *Audiomagnetotellurik, Magnetotellurik und Erdmagnetische Tiefensondierung im mittleren und nordlichen Schwartzwald.* 46th Annu. Meet. DGG., Karlsruhe, 1986.
25. Bonjer, K.-P., C. Gelbke, R. Gilg and D. Rouland, *Seismicity and dynamics of the upper Rhinegraben.* J. Geophys., 1984. **55**: p. 1-12.
26. Brasse, H., *Audiomagnetotelluric investigation of hydrogeological and tectonic problems in eastern Sahara.* IAGA BULL., 1990. **53**: p. 165-165.
27. Brewitt-Taylor, C.R. and J.T. Weaver, *On the finite difference solution of two-dimensional induction problems.* Geophys. J. R. astr. Soc., 1976. **47**: p. 375-396.
28. BRGM, *Carte géologique de la France à l'échelle 1: 50 000, Remiremont and Plombières-Les-Bains.* 1979.
29. Brun, J.P., M.A. Gutscher and D.-E. team, *Deep crustal of the Rhine Graben from DEKORP-ECORS seismic reflection data: A summary.* Tectonophysics, 1992. **208**: p. 139-147.

30. Brun, J.P., F. Wenzel and E.-D. team, *Crustal-scale structure of the southern Rhine Graben from DEKORP-ECORS seismic reflection data.* Geology, 1991(19): p. 728-762.
31. Byerlee, J., *Friction, over pressure and fault normal compression.* Geophys. Res. Lett., 1990. **17**: p. 2109-2112.
32. Cagniard, L., *Basic theory of the magnetotelluric method of geophysical prospecting.* Geophysics, 1953. **18**: p. 605-635.
33. Camfield, P.A., *Magnetometer array in the tectonically active region of Quebec, Canada.* Geophys. J. R. astr. Soc, 1981. **65**: p. 553-570.
34. Chave, A.D. and J.T. Smith, *On electric and magnetic distortion tensor decompositions.* J. Geophys. Res, 1994. **99**(B3): p. 4669-4682.
35. Chen, C.C., Chen, C.S. and Shieh, C.-F., 2002. *Crustal electrical conductors, crustal fluids and 1999 Chi-Chi, Taiwan earthquake.* TAO, 13(3): 367-374.
36. Crampin, S., Volti, T., Chastin, S., Gudmundsson, A. and Stefansson, R., 2002. *Indication of high pore-fluid pressure in a seismically-active fault zone.* Geophys. J. Int., 151: F1-F5.
37. deGroot-Hedlin, C. and S. Constable, *OCCAM's inversion to generate smooth, two dimensional models from magnetotelluric data,.* Geophysics, 1990. **55**: p. 1613-1624.
38. Deichmann, N. and M. Baer, *Earthquakes focal depths below the Alps and northern Alps of Switzerland, the European Geotraverse.* European Science Foundation, Strasbourg, France., 1990.
39. Delouis, B., H. Haessler, A. Cisternas and L. River, *Stress tensor determination in France and neighbouring regions.* Tectonophysics, 1993. **221**: p. 413-437.
40. Echternacht, F., S. Tauber, M. Eisel, H. Brasse, G. Schwarz and V. Haak, *Electromagnetic study of the active continental margin in northern Chile.* Phys. Earth Plan. Int., 1997. **102**: p. 69-87.
41. El-Sayed, A., F. Vaccari and G.F. Panza., *Deterministic seismic hazard in Egypt,.* Geophys. J. Int., 2001. **144**: p. 555-567.
42. El-Shazly, E.M., *The geology of the Egyptian region*. The ocean basin and margins. Vol. 145. 1977. 193-207.
43. Evans, K., J. Beavan and D. Simpson, *Estimating aquifer parameters from analysis of forced fluctuations in well level: An example from the Nubian formation near Aswan, Egypt. 1. Hydrogeological background and large-scale permeability estimates.* J. Geophys. Res., 1991. **96**(No. B7): p. 12127-137.
44. Evans, K., J. Beavan and D. Simpson, *Estimating aquifer parameters from analysis of forced fluctuations in well level: An example from the Nubian formation near Aswan,*

Egypt. 3. Diffusivity estimates for saturated and unsaturated zones. J. Geophys. Res., 1991. **96**(No. B7): p. 12161-12191.

45. Farquharson, C.C. and D.W. Oldenburg, *Approximate sensitivities for the electromagnetic inverse problem.* Geophys. J. Int., 1996. **126**: p. 235-252.
46. Filloux, J., *Instrumentation and experimental methods for oceanic studies.* Geomagnetism, 1987. **1**(ed Jacobs, J., Academic Press, London).
47. Fischer, G. and W. Masero, *Rotational properties of the magnetotelluric impedance tensor: the example of the Araguainha impact crater, Brazil.* Geophys. J. Int., 1994. **119**: p. 548-560.
48. Fluck, P., A. Pique, J.-L. Schneider and H. Whitechurch, *Le Socle Vosgien,.* Sci. Géol. BULL., Strassbourg, 1991. **44**(3-4): p. 207-235.
49. Gamble, T.D., W. M.Goubau and J. Clarke, *Magnetotelluric with remote magnetic reference.* Geophysics, 44, 53-68, 1979. **44**: p. 53-68.
50. Gamble, T.D., W. M.Goubau and J. Clarke, *Error analysis for remote reference magnetic reference.* Geophysics, 1979. **44**: p. 959-968.
51. Gavrilenko, P. and Gueguen, Y., 1993. *Fluid overpressures and pressure solution in the crust.* Tectonophysics, 217: 19-110.
52. Gavrilenko, P. and Gueguen, Y., 1998. *Flow in fractured media: a modefied renormalization method.* Water Resources Res., 43: 177-191.
53. Gavrilenko, P., Mlikadze, G., Chelidze, T., Gibert, D. and Kumsiashvili, G., 2000. *Permanent water level drop associated with Spitak earthquake: observation at Lisi borehole (Republic of Georgia) and modelling.* Geophys. J. Int., 143: 83-98.
54. Gerstenberger, M., S. Wiemer and D. Giardini, *A systematic test of the null hypothesis that the b-value varies with depth in California.* Geophys. Res. Lett., 2001. **28**(1): p. 57-61.
55. Gharib, A., *The crust and the upper mantle structure in the lake Nasser area from seismic waves generated by earthquakes and explosions.* Ph.D. Thesis, Faculty of science, Cairo University., 1992.
56. Gharib, A. and D.W. Simpson, *Crustal structure around lake Aswan, Egypt,.* 1st Sc. Gen. Meeting, NRIAG Bull., 1990.
57. Gibowicz, S.J., Droste, Z., Kebeasy, R., and Ibrahim, I. M., *A micro earthquake survey in Abu-Simbel area in Egypt.* Eng. Geol., 1982. **19**: p. 95-109.
58. Grassberger, P. and P.D. Procaccia, *Measuring the strangeness of strange attractors.* Physica, France, 1983. **9**(D): p. 189-208.
59. Grasso, J.-R., F. Guyoton, J. Frechet and J.F. Gammond, *Triggering earthquakes as stress Gauge: Implication for the upper crust behaviour in the Grenoble area, France.* PAGEOPH, 1992. **139**: p. 579-605.

60. Grellet, B., P. Combes, T. Granier and H. Philip, *Sismotectonique de la France métropolitaine dans son cadre géologique et géophysique.* IPSN, 1993. **1**.
61. Groom, R.W. and K. Bahr, *Correction for near surface effects: decomposition of the magnetotelluric impedance tensor and scaling corrections for regional resistivities: a tutorial.* Surv. Geophys., 1992. **13**: p. 341-379.
62. Groom, R.W. and R.C. Bailey, *Decomposition of Magnetotelluric Impedance Tensors in Presence of Local Three-Dimensional Galvanic Distortion.* J. Geophys. Res., 1989. **94**(B2): p. 1913-1925.
63. Groom, R.W. and R.C. Bailey, *Analytical investigation of the effects of near surface three-dimension galvanic scatters on MT tensor impedance.* Geophysics, 1991. **56**: p. 496-518.
64. Gudmudsson, A., Berg, S.S., Lyslo, K.B. and Skurtveit, E., 2001. *Fracture networks and fluid transport in active fault zones.* J. Struct. Geol., 23: 343-353
65. Gupta, H.K., *Reservoir induced seismicity.* Elsevier, Amsterdam, 1992: p. 364.
66. Gupta, H.K. and B.K. Rastogi, *Dams and earthquakes.* Elsevier, New York, 1976: p. 364.
67. Gutenberg, B. and C.F. Richter, *Magnitude and energy of earthquakes.* Ann. Geofis., 1956. **9**: p. 1-15.
68. Harris, R.A. and R.W. Simpson, *Changes in static stress changes on southern California faults after the 1992 Landers earthquake.* Nature, 1992. **360**: p. 251-254.
69. Hassib, G.H., *A study on the earthquake mechanics around the High Dam Lake, Aswan, Egypt.* Ph.D. Thesis, Faculty of Science, South Valley University, Sohag, Egypt., 1997.
70. Helmstetter, A., *Rupture and instabilities: seismic and landslides.* Ph.D. thesis, Grenoble Univ., 2002: p. 387.
71. Helmstetter, A. and D. Sornette, *Subcritical and Supercritical regimes in epidemic models of earthquakes aftershocks.* J. Geophys. Res, 2003. **107**.
72. Helmstetter, A. and D. Sornette, *Diffusion of earthquakes aftershocks and Omori law: exact mapping to generalized continuous time random walks models.* Physical Review E., 2003. **107**(10).
73. Helmstetter, A., D. Sornette and J.-R. Grasso, *Mainshocks are aftershocks of conditioned foreshocks.* ,J. Geophys. Res., in press, 2003.
74. Hickmann, S., Sibson, R.H. and Bruhn, R., 1995. *Introduction to special section: mechanical involvement of fluids in faulting*. J. Geophys. Res., 100: 12831-12840.
75. Hohmann, G.W., *Three dimensional induced polarization and electromagnetic modeling.* Geophysics, 1975. **40**: p. 309-324.

76. Imoto., M., *On migration phenomena of aftershocks following large thrust earthquakes in subduction zones.* Report of the National Center for Disaster prevention, 1981. **25**: p. 29-86.
77. Issawi, B., *The geology of Kurkur-Dungul area.* General Egyptian Organization for Geological Research and Mining, Geological Survey of Egypt, Cairo, Egypt., 1969. **46**: p. 101.
78. Issawi, B., *Geology of Nubia west area, western desert,.* Annals of the Geological Survey of Egypt, 1978.
79. Issawi, B., *Geology of the southwestern desert of Egypt.* Annals of the Geological Survey of Egypt., 1982.
80. Johnson, P.A. and J.V. McEvilly, *Parkfield seismicity : Fluid driven?* J. Geophys. Res, 1995. **100**(b7): p. 12937-12950.
81. Jolly, A.D. and S.R. McNutt, *Seismicity at the volcanoes of Katmai National Park, Alaaska, July 1995-December 1997.* J. Volc. Geoth. Res., 1999. **93**: p. 173-190.
82. Jones, A.G., *Static shift of magnetotelluric data and its removal in a sedimentary basin enviroment.* Geophysics, 1988. **53**: p. 867-978.
83. Jones, R.A. and R.C. Stewart, *A method for determining significant structures in a cloud of earthquakes.* J. Geophys. Res., 1997. **102**: p. 8245-8254.
84. Kagan, I. and L. Knopoff, *Stochastic synthesis of earthquakes catalogue.* J. Geophys. Res., 1981. **86**: p. 2853-2862.
85. Kao, D.W. and D. Rankin, *Enhancement of signal-to-noise ratio in magnetotelluric data,.* Geophysics, 1977. **42**: p. 103-110.
86. Karner, S. and C. Marone, *Frictional restrengthening in simulated fault gauge: effect of shear load perturbations*, J. Geophys. Res., **106,** 19319-19337.
87. Kaufman, A.A. and G.V. Keller, *The magnetotelluric sounding method. Series in methods in Geochemistry and Geophysics.* Elsevier, Amsterdam, 1981. **15**: p. 595.
88. Kebeasy, R.M., *Seismicity, in The Geology of Egypt.* ed Said R. A. Balkema, Rotterdam, 1990: p. 51-59.
89. Kebeasy, R.M., A.I. Bayoumi and A.A. Gharib, *Crustal structure modeling for the north part of the Aswan lake using seismic waves generated by explosions and local earthquakes.* J. Geodynamics, 1991. **14**: p. 159-182.
90. Kebeasy, R.M. and A.A. Gharib, *Active fault and water loading are important factors in triggering earthquake activity around Aswan Lake.* J. Geodynamics, 1991. **14**: p. 73.82.
91. Kebeasy, R.M., M. Maamon and E.M. Ibrahim, *Aswan Lake induced earthquake.* Bull. International Institute of Seismology and Earthquake Engineering, Tsukuba, 1982. **19**.

92. Kebeasy, R.M., M. Maamon, E.M. Ibrahim, A. Megahed, D.W. Simpson and W.S. Leith, *Eerthquake studies at Aswan Reservoir.* J. Geodynamics, 1987. **7**: p. 173-193.
93. Kebeasy, R.M. and A.A. Tealab, *Earthquake activity and subsurface structures of south valley project.* , internal report, NRIAG, 1997. **14**: p. 1-87.
94. Kharaka, Y.K., J.J. Thordsen, W.C. Evans and B.M. Kennedy, *Geochemistry and hydromechanical interactions of fluids associated with San Andreas Fault system, California, in Faults and subsurface fluid flow in the shallow crust, ed. by W. C. Haneberg, P. S. Mosely, J. C. Moore and L. B. Goodwin.* Geophys Monograph, 1999. **113**: p. 129-148.
95. King, G.C., R.S. Stein and J. Lin, *Static stress changes and the triggering of earthquakes.* Seismological Society of America Bulletin, 1994. **84**: p. 935-953.
96. Lahaie, F. and J.-R. Grasso, *Loading rate impact on fracturing pattern: Lessons from Hydrocarbon recovery, Lacq gas field, France.* J. Geophys. Res., 1999. **104**: p. 941-954.
97. Larsen, J.C., *Removal of local surface conductivity effects from low frequency mantle response curves.* Acta Geodaet., Geophys. et Montanist. Acad. Sci. Hung., 1977. **12**(183-186).
98. Lee, W., *Hypo71 PC program.* IAESPI software library, 1990. **1**.
99. Lemonnier, C., G. Marquis, F. Perrier, J.-P. Avouac, G. Chitrakar, B. Kafle, S. Sapkota, U.Gautam, D.Tiwari and M. Bano, *Electrical structure of the Himalaya of central Nepal; high conductivity around the mid-crustal ramp along the MHT.* Geophys. Res. Lett, 1999. **26**(21): p. 3261-3264.
100. Li, S., M.J. Unsworth, J.R. Booker, W. Wei, H. Tan and A.G. Jones, *Partial melt or aqueous fluid in mid-crust of southern Tibet? Constraints from INDEPTH magnetotelluric data.* Geophys. J. Int., 2003. **153**: p. 289-304.
101. Maamoun, M., *Observed intensity-epicenteral distance relation in Egyptian earthquakes.* BULL. NRIAG, Cairo, Egypt, 1979. **184**: p. 1-12.
102. Maamoun, M. and E.M. Ibrahim, *Tectonic activity in Egypt as indicated by earthquakes.* NRIAG, 1978. **170**: p. 1-13.
103. Maamoun, M., A. Megahed. and A. Allam., *Seismicity in Egypt.* NRIAG, 1984. **4**(B).
104. Mackie, R.L., D.W. Livelybrooks, T.R. Madden and J.C. Larsen, *A magnetotelluric investigation of the San Andreas fault at Carrizo Plain California.* Geophys. Res. Lett, 1997. **24**: p. 1874-1850.
105. Madden, R. and R. Mackie, *What electrical measurements can say about changes in fault systems.* Proc. Natl. Acad. Sci, USA, 1996. **93**: p. 3776-3780.

106. Mahmoud, S.M., S.N. Bhattacharya, S. Yunga and H.N. Srivastava, *Seismicity pattern near Aswan reservoir, Egypt.* NRIAG BULL, Geophysics B, 1998. **XII**: p. 173.

107. Malergue, G., J. Aissa, C. Herisson and J. Rainaud, *Recent developments in the magnetotelluric prospecting method.* First Break, 1986. **4**: p. 23-28.

108. Malone, S. and S. Wiemer, *A software package to analyze seismicity: ZMAP.* Seis. Res. Lett., 2001. **72**: p. 374-383.

109. McGarr, A., *On a possible connection between three major earthquakes in California and oil production.* Bull. Seis. Soc. Am., 1991. **81**: p. 948-970.

110. McGarr, A., D. Simpson and L. Seeber, *Case histories of induced and triggered seismicity.* Int. Handbook earthquake and engineering seismology, 2002. **81A**: p. 647-661.

111. McNeice, G.W. and A.G. Jones, *Multisite, multifrequency tensor decomposition of magnetotellric data.* Geophysics, 2001. **66**: p. 158-173.

112. Mekkawi, M., J.-R. Grasso and P.-A. Schnegg, *Seismicity patterns at Lake Aswan, Egypt, 1982-2001.* Bull. Seis. Soc. Am., 2003. **submitted**.

113. Mogi, K., *Sequential Occurrences of recent great earthquakes.* J. Phys. Earth, 1968. **16**: p. 1-30.

114. Mohammed, A., *Seismic microzoning study and its applications in Egypt.* Ph.D thesis, Ain Shams University, Egypt., 1993.

115. Mori, J. and R. Abercrombie, *Depth dependence of the earthquake frequency-magnitude distribution in California: implications for rupture initiation.* J. Geophys. Res, 1997. **102**: p. 15081-15090.

116. Morrison, F., *Lectures on review of Magnetotellurics: Principals and Applications.* Univ of California, Berkeley, (ed. in Sept., 1997,Warsaw), 1997.

117. Mueller, B., B.J. Reinecker and K. Fucks, *The 2000 release of the world stress map, available online.* at http://www.wsm.physik.uni-karlsruhe.de, 2000.

118. Noir, J., Jacques, E., Bekri, S., Adler, P.M., Tapponnier, P. and King, G.C.P., 1997. *Fluid flow triggered migration of events in the 1989 Dobi earthquakes sequence of central Afar.* Geophys. Res. Lett., 24(18): 2335-2338.

119. Noshy., M.G., *Geophysical studies on some localities in southern Egypt.* Ph.D. Thesis, Faculty of Science, Cairo University, 1993.

120. Nur, A. and Walder, J., 1990. *Time-dependent hydraulics of the earth's crust. In: the role of fluids in crustal process.* National Research Council, National Academic press. D C, Washington, 170 pp

121. Ogata, Y., *Statistical model for earthquake occurrence and residual analysis.* J. Am. Stat. Assoc, 1998. **83**: p. 9-27.

122. Omori, F., *Investigation of aftershocks.* Rep. Earthq. Inv. Comm., 1894. **2**: p. 103-139.
123. Osella, A.M. and P. Martinelli, *Magnetotelluric response of anisotropic 2-D structure.* Geophys. J. Int., 1993. **115**: p. 819-829.
124. Osman, A. and A. Ghobarah, *The Aqaba earthquake of November 22, 1995.* EERI special earthq rept, 1996.
125. Park, S.K., *Minotering resistivity changes prior to earthquakes in Parkfield, California, with telluric array.* J. Geophys. Res, 1991. **96**: p. 14211-14237.
126. Park, S.M., T. Johnston, F. Madden and F. Morrison, *Electromagnetic precursors to earthquakes in the ULF band: Aereal view of observations and mechanisms,.* Rev. Geophys., 1993. **31**(No. 2): p. 117-132.
127. Parkinson, W.D., *The influence of continents and oceans on geomagnetic variations.* Geophys. J. astr. Soc, 1962. **42**: p. 3-30.
128. Plenefish, T. and K.-P. Bonjer, *The stress field in the Rhine Graben area inferred from earthquakes focal mechanisms and estimation of frictional parameters.* Tectonophysics, 1997. **275**: p. 71-79.
129. Pous, J., P. Queralt, J. Ledo and E. Roca, *A high electrical conductive zone at lower crustal depth beneath the Betic Chain (Spain).* Earth Plant. Sci. Lett., 1999. **167**(1-2): p. 35-45.
130. Raleigh, B. and J. Evernaden, *Case for low deviatoric stress in the Lithosphere. Mechanical behaviour of crustal rocks, The Handin volume.* Geophysical Monograph, 1981. **24**: p. 173-186.
131. Rice, J.R., 1992. *Fault stress, pore pressure distribution, and weakness of the San Andreas fault. Fault mechanics and transport properties of rocks.* Academic press, San Diego, 475-503 pp.
132. Richards, M.L., U. Schmucker and E. Steveling, *Electrical conductivity in the Urach Geothermal project (Swabian Alb Germany).* Scweizerbart'sche Verlagsbuchhandlung, Stuttgart, 1981: p. 301-311.
133. Rodi, W. and R.L. Mackie, *Nonlinear coniugate gradients algorithm for 2-D magnetotelluric inversion.* Geophysics, 2001. **66**: p. 174-187.
134. Roeloffs, E.A., *Fault stability changes induced beneath a reservoir with cyclic variations in water level.* J. Geophys. Res., 1988. **93**: p. 2107-2124.
135. Rokityansky, I.I., *Geoelectromagnetic investigation of earth's crust and upper mantle.* Springer Verlag, Berlin., 1982: p. 381.
136. Rooney, D. and V. Hutton, *A magnetotelluric and magnetovariational study of the Gregory Rift Valley, Kenya.* Geophys. J. R. astr. Soc, 1977. **51**: p. 91-119.
137. Said, R., *The geology of Egypt.* Elsevier. Amsterdam, New Yourk, 1962: p. 377.

138. Sausse, J., Jacquot, E., Fritz, B., Leroy, J. and Lespinasse, M., 2001. *Evolution of crack permeability during fluid-rock interaction: example of the Brezouard granite (Vosges, France).* Tectonophysics, 336: 199-214

139. Schmucker, U., *Anomalies of geomagnetic variations in the southwestern United States.* Bull. Scripps Inst. Oceanograph. Univ. Calif., 1970. **13**.

140. Schnegg, P.-A., *The magnetotelluric survey of the penninic Alps of Valais.* , Bern, Swiss Geophysical Commission, P76., 1998: p. 76.

141. Schnegg, P.-A., G. Fischer, B.V. LeQuang and J. Weaver, *Investigation of a buried vertical fault with natural and controlled source AMT.* Ann. Geophysicae, 1987. **4B**: p. 139-144.

142. Schnegg., P.-A., *An automatic scheme for 2D magnetotelluric modeling, based on low order polynomials fitting.* J. Geomag. Geoelect., 1993. **45**: p. 1039-1043.

143. Schneider, J.L., *Enregistrement de la dynamique Varisque dans les bassins volcano-sédimentaires Dévono-Dinantiens : example des Vosges du sud (Zone Moldanubienne).* Thèse Univ. Louis Pasteur, Strasbourg, 1990: p. 222 PP., 101 fig., 11 pl.

144. Schwartz, D., W. Joyner, R. Stein, R. Brown, A. McGarr, S. Hickman and W. Bakun, *Review of seismic-hazards issues associated with the Asuburn Dam Project, Sierra Nevada foothills, California.* U. S. Geological Survey open report (96-0011). 1996.

145. Seeber, L., G. Ekstrom, S.K. Jain, C.V.R. Murty, N. Chandak and P. J. G. Armbruster, *The Killari earthquake in central India: A fault in Mesozoic basalt flows.* J. Geophys. Res., 1996. **101**: p. 8543-8560.

146. Sharma, P.V., *Enviromental & Engineering Geophysics.* Cambridge Univ. Press, 1997.

147. Simpson, D.W., *Triggered earthquakes.* Annual Rev. Earth and Planetary Science, 1986. **14**: p. 21-42.

148. Simpson, D.W., A.A. Gharib and R.M. Kebeasy, *Induced seismicity and changes in water level at Aswan reservoir, Egypt.* Gerlans. Beitr. Geophysik Leipzig, 1990. **99**: p. 191-204.

149. Simpson, D.W., R.M. Kebeasy, C. Nicholson, M. Maamoun, R.N.H. Albert, E.M. Ibrahim, A. Gharib and A. Hussein, *Aswan telemetered seismograph network.* J. Geodynamics, 1987. **7**: p. 195-203.

150. Simpson, D.W. and W. Leith, *The 1976 and 1984 Gazli, USSR, earthquakes-were they induced?* Bull. Seis. Soc. Am., 1985. **75**: p. 1465-1468.

151. Simpson, D.W., W. Leith and C.H. Scholz, *Two types of reservoir-induced seismicity.* Bull. Seis. Soc. Am., 1988. **75**: p. 2025-2040.

152. Simpson, D.W. and S.K. Negmatallaev, *Induced seismicity at Nurek reservoir, Tadjikistain, USSR.* Bull. Seis. Soc. Am., 1981. **75**: p. 1465-1468.
153. Sims, W.E. and F.X.J. Bostick, *Methods in magnetotelluric analysis.* Univ. of Texas at Austin, EGRL Technical Report, 1969(No. 58).
154. Siripunvaraporn, W. and G. Egbert., *Software documentation and user manual a Reduced Basis OCCam (REBOCC) Inversion for two-dimensional magnetotelluric data.* Collage of oceanic and Atmospheric Science, Oregon State University., 1999.
155. Siripunvaraporn, W. and G. Egbert., *An efficient data-subspace inversion method for 2-D magnetotelluric data.* Geophysics, 2000. **65**: p. 791-803.
156. Sitter, C., *Illustration de l'histoire géologique du fossé rhénan et de l'Alsace.* Geol. Palaont. Abh., 1992. **186**(3): p. 255-282.
157. Sitter, C. and M. Hoff, *Collines Sous-Vosgiennes: disposition structurale, champs de fractures, Séries sédimentaires, écologie et groupement Végétaux.* Encyclopedie de l'Alsace, Strasbourg, 1983. **3**: p. 1816-1823.
158. Smith, C.M., *Geology of Egypt Rep.* Schlumberger Oil Company, Well Evalution Conf. Cairo, Egypt., 1984.
159. Smith, J.T., *Understanding telluric distortion matrices.* Geophys. J. Int., 1995. **122**: p. 219-226.
160. Smith, J.T. and J.R. Booker, *Rapid inversion of two and three-dimensional magnetotelluric data.* J. Geophys. Res., 1991. **96**: p. 3905-3922.
161. Snow, D.T., *Geodynamics of seismic reservoirs, Proc. Percolation through Fissured rocks.* Ges. Erd. Grundbau, Stuttgart,, 1972. **T2-J**: p. 1-19.
162. Stein, R.S., *The role of stress transfer in earthquakes occurrence.* Nature, 1999. **402**: p. 605-609.
163. Stein, R.S., G. King and J. Lin, *Change in Failure stress on the southern San Andreas Fault system caused by the 1992 magnitude 7.4 Landers earthquake.* Science, 1992. **258**: p. 1328-1332.
164. Sternberg, B.K., J.C. Washburne and L. Pellerin, *Correction for static shift in magnetotellurics using transient electromagnetic soundings.* Geophysics, 1988. **53**: p. 1549-1468.
165. Sue, C., J.-R. Grasso, F. Lahaie and D. Amitrano, *Mechanical behaviour of western Alpine structures inferred from statistical analysis of seismicity.* Geophys. Res. Lett., 2002. **29**(No. 8): p. 1-4.
166. Suzuki, K., S. Toda, K. Kusunoki, Y. Fujimitsu, T. Mogi and A.J. omori, *Case studies of electrical and electromagnetic methods applied to mapping active faults beneath the thick quaternary.* Eng. Geology, 2000. **56**: p. 24.45.

167. Tajima, F. and H. Kanamori, *Global survey of aftershock expansion patterns.* Phys. Earth Plan. Inter., 1985. **40**: p. 77-134.
168. Tajima, F. and H. Kanamori, *Aftershocks area expansion and mechanical heterogeneity of fault zone within subduction zone.* Geophys. Res. Lett., 1985. **12**: p. 345-348.
169. Talwani, P. and S. Acree, *Pore-pressure diffusion and the mechanism of reservoir induced seismicity.* PAGEOPH, 1985. **122**: p. 947-965.
170. Tealeb, A., *Programs for monitoring crustal deformation seismoactive areas in and around Egypt using geodetic techniques.* Preceeding of the 1st. Turkish Inter. Symp. On deformation, Istanbul, 1994. **94**: p. 872-898.
171. Tealeb, A., *Programs for monitoring crustal deformation and seismic hazard assessment in Egypt using geodetic techniques.* NRIAG , Internal Rep. (unpublished). 1998.
172. Tealeb, A. and A.S.N. Team, *Report on seismicity, deformation and seismic hazard in and around Wadi Kalabsha area, Aswan.* NRIAG, Cairo, Egypt, 1999.
173. Thenhaus, P.C., R.V. Sharp, M. Celebi, A.K. Ibrahim and H. Van, *Reconnaissance report on the 12 October 1992 Dahshour, Egypt.* Earthquake U. S. Geological Survey, open report, Golden Co., 1993: p. 93-181.
174. Toppozada, T., F. Boulos, S. Henin, A. El-Sherif, A. El-Sayed, N. Basta, F. Shatiya, Y. MeliK, C. Cramer and D. Parke, *Seismicity near Aswan High Dam, Egypt, following the November 1981 earthquake.* Annals of the geological survey of Egypt, 1984. **XIV**: p. 107-126.
175. Uchida, T., *Smoothed 2-D inversion for magnetotelluric data based on statistical criterion.* J. Geomag. Geoelect., 1993. **45**: p. 841-858.
176. Unsworth, M.J., P. Bedrosian, M. Eisel, G.D. Egbert and W. Siripunvaraporn, *Along strike variations in the electrical structure of the San Andreas Fault at Parkfield, California*, in *Geophys. Res. Lett.* 2000. p. 3021-3024.
177. Unsworth, M.J., G.D. Egbert and J. Booker, *High resolution electromagnetic imaging of the San Andreas Fault in central California.*, in *J. Geophys. Res.* 1999. p. 1131-1150.
178. Unsworth, M.J., P.E. Malin, G.D. Egbert and J.R. Booker, *Internal Structure of the San Andreas fault at Parkfield, California.*, in *Geology*. 1997. p. 359-362.
179. Utsu, T., Y. Ogata and S. Matsu'ura, *The centenary of the Omori formula for a decay law of aftershock activity.* J. Phys. Earth, 1995. **43**: p. 1-33.
180. Vogel, S., 1995. *Naked earth : the new geophysics*. Penguin, London, 217 pp.
181. Volti, T.K., *Magnetotelluric measurements on the Methana Peninsula (Greece): modelling and interpretation.* Tectonophysics, 1999. **301**: p. 111-132.

182. Vozoff, K., *The magnetotelluric method in the exploration of sedimentary basin.* Geophysics, 1972. **37**: p. 98-141.
183. Vozoff, K., *Magnetotelluric Methods*. Geophysics reprint series, ed. F.K. Levin. 1986: SEG.
184. Vozoff, K., *Magnetotelluric Methods, in Electromagnetic Methods in Applied Geophysics, Vol. 2.* . Geophysics reprint series, ed. M.N. Nabighian. Vol. 2. 1991: SEG. 641-711.
185. Vyskocil, P., *Present stage of geodynamical properties of Kalabsha area, Northwest of Aswan Lake, Egypt.* J. Geodynamics, 1991. **14**: p. 221-247.
186. Wannamaker, P., J. Stodt and L. Rijo, *Two dimensional topographic responses in magnetotelluric modeled using finite elements.* Geophysics, 1986. **51**: p. 2131-2144.
187. Wannamaker, P., J. Stodt and L. Rijo, *A stable finite element solution for two-dimensional magnetotelluric modelling.* Geophys. J. Res. Astro. Soc., 1987. **88**: p. 277-296.
188. Wannamaker, P.A., J.A. Stodt and L.Rijo, *PW2D-finite element program for solution of magnetotelluric responses of two-dimensional earth resistivity structure*. 1985, Earth Science Laboratory, University of Utah: Salt Lake City.
189. Ward, S.H., 1990. *Geotechnical and environmental geophysics: review and tutorial, 1*. SEG, Tusla, Oklahoma, 389 pp.
190. Weidelt, P., *EM induction in 3-D structures.* J. Geophys.. 1975. **41**: p. 85-109.
191. Werner, D. and M. Parini, *The geothermal anomaly of Landau/Pfalz-an attempt of interpretation.* J. Geophys., 1980. **48**: p. 28-33.
192. Wiemer, S. and J. Benoit, *Mapping the b-value anomaly at 100 km depth in the Alaska and New Zealand subduction zones.* Geophys. Res. Lett., 1996. **23**: p. 1557-1560.
193. Wiemer, S., S. McNutt and M. Wyss, *Temporal and three dimensional spatial analysis of the frequency-magnitude distribution near Long Valley Caldera, California.* J. Geophys. Int., 1998. **134**: p. 409-421.
194. Wyss, M., K. Nagamine, E. Klein and S. Wiemer, *Evidence for magma at intermediate crustal and depth below Kilaueas east rift, Hawii, based on anomalously high b-values.* J. Volc. Geoth. Res. (in press), 2000.
195. Youssef, N., S. Adham, M. Celeibi and J. Malilay, *Cairo, Egypt, Earthquake of October 12.* EERI Newsletter, 1992. **26**(12).
196. Yungul, E.H., *Geoelectricity in McGraw-Hill Encyclopida of Science and Technology*. 1982: Geol. Palaeont. Abh. 171-175.
197. Yungul, E.H., *Electrical methods in geophysical exploration of deep sedimentary basins.* printed in Great Britain by St. Edmundsbury Press., 1996.

198. Zhang, P., L.B. Pedersen, M. Mareschal and M. Chouteau, *Channelling contribution to tipper vectors: a magnetic equivalent to electric distortion.* Geophys. J. Int., 1993. **113**: p. 693-700.

199. Ziegler, P.A., *European Cenozoic rift system, present-day deformation of the French northwestern Alps/southern Jura mountains : Comparison between historical triangulations.* Tectonophysics, 1992. **208**: p. 91-111.

200. Zoback, M.D. and S. Hickmann, *In situ study of the physical mechanisms controlling induced seismicity at Monticello reservoir, South Carolina.* J. Geophys. Res, 1982. **87**: p. 6959-6974.